

INVESTIGATION OF HYDROGEN BONDING
IN STRONG NITROGEN BASES

By

PIERRE HENRI CHABRIER

A DISSERTATION PRESENTED TO THE GRADUATE SCHOOL
OF THE UNIVERSITY OF FLORIDA IN PARTIAL FULFILLMENT
OF THE REQUIREMENTS FOR THE DEGREE OF
DOCTOR OF PHILOSOPHY

UNIVERSITY OF FLORIDA

1998

ACKNOWLEDGMENTS

I want to sincerely thank Dr. Willis B. Person for welcoming me in his laboratory. This acknowledgment is not just a formality. Dr. Person, through his guidance and patience, was able to comprehend my ideas (no matter how awkwardly stated) and to sharpened my understanding of the subject. The numerous discussions we have had unequivocally helped me put together this dissertation.

I would also like to express my deepest gratitude to Dr. Krystina Szczepaniak for teaching me the use of the FTIR spectrometer and of the matrix isolation technique. I have greatly appreciated our long conversations about science and maybe more importantly about life itself. Her attachment to Polish traditions and her culinary abilities made me discover the unforgettable piroghi.

I wish to extend my thanks to Dr. Barbara Galuska-Muga for the preparation of the different salts studied in this work and to Dr. Janet E. Del Bene for providing the ab initio calculations as well as for very helpful discussions. Without their contributions, this work would not have been possible.

Other people have played a significant role in my stay at the University of Florida. I would like to acknowledge, in particular, Dr. Martin T. Vala who was my first contact from France and who provided me the opportunity to complete a Ph.D. in a totally new cultural environment. His support during difficult times was sincerely appreciated.

Thanks are extended to Dr. Lisa A. McElwee-White, Dr. William Weltner and Dr. Neil S. Sullivan for their participation on the supervisory committee. Friends with whom I will be able to share happy memories also deserve my thanks: Scott Ekern, Piotr and Ewa Roziczko, Igor and Lena Gornushkin, Mike Pearson, Alfredo and Daisy Matteus, and many others.

I am also grateful to the support from NSF through grant No. CHE-950588 made jointly to Drs. Del Bene and Person for collaborative studies on strong H-bonds.

Last but not least, I want to thank my loving wife, Christina, who gave me her support throughout this work and helped me edit the present dissertation.

TABLE OF CONTENTS

	<u>page</u>
ACKNOWLEDGMENTS.....	ii
ABSTRACT	vii
 CHAPTERS	
I. INTRODUCTION.....	1
II. EXPERIMENTAL CONSIDERATIONS	7
A. Experimental Techniques.....	7
1. Brief Review of Fourier Transform Infrared Spectroscopy	7
2. Matrix Isolation.....	8
3. Formation of the Complex.....	10
B. Experimental Setup	12
C. Infrared Band Intensities and Concentrations.....	16
1. Determination of the Pathlength ℓ	18
2. Determination of Integrated Relative Intensities	20
3. Determination of the Concentration.....	20
III. TOOLS FOR VIBRATIONAL ANALYSIS	23
A. Coordinate Systems.....	24
B. Force Field in Internal and Symmetry Coordinates.....	27
C. Solutions of the Secular Equation	29
D. Potential Energy Distributions	31
E. Intensity Distributions	32
F. Atomic Cartesian Displacements.....	34
IV. INVESTIGATION OF SUBSTITUTED PYRIDINE COMPLEXES WITH HYDROGEN BROMIDE	36
A. The HBr:pyridine Complex.....	36
1. Infrared Spectra of Pyridine	36
2. Vibrational Analysis of Pyridine.....	40
3. Infrared Spectra of the HBr:pyridine Complex.....	44
4. Theoretical Ab initio Prediction	52

5. Discrepancies between Computed and Experimental Spectra.....	56
B. The HBr:3,5-dichloropyridine Complex	63
1. Introduction.....	63
2. Infrared Spectra of the 3,5-DCP	64
3. Vibrational Analysis of the 3,5-DCP	67
4. Infrared Spectra of the HBr:3,5-DCP Complex.....	71
5. Theoretical Prediction and Comparison.....	74
6. Force Field Treatment.....	81
C. The HBr:4-chloropyridine Complex	87
1. Infrared Spectra and Analysis of 4-chloropyridine	87
2. Infrared Spectra of the HBr:4-CP Complex.....	94
3. Theoretical Prediction and Force Field Treatment	96
D. The HBr:4-methylpyridine Complex	102
1. Infrared Spectra and Analysis of 4-methylpyridine	102
2. Infrared Spectra of the HBr:4-MP Complex.....	109
3. Theoretical Prediction and Force Field Treatment	111
E. The HBr:3,5-dimethylpyridine Complex.....	118
1. Infrared Spectra and Analysis of 3,5-dimethylpyridine	118
2. Infrared Spectra of the HBr:3,5-DMP Complex.....	124
V. COMPARISONS AND TRENDS	128
A. Matrix Effect on the Complex.....	128
B. The Proton Stretch Local Oscillator	134
C. Force Constants	142
1. Effect of the Scale Factors on the Spectrum	142
2. Force Constants of the Proton Stretch Local Oscillator.....	149
3. Harmonic Coincidental Match.....	152
VI. CONCLUSION	155
APPENDICES	
A. FORTRAN FLOW-CHART DIAGRAM	159
B. CONSTRUCTING THE INPUT FILES FOR XTRAPACK	168
Input Files Generated by Xtrapack.....	168
Coordinate Input File	168
Internal Coordinates	170
Symmetry Coordinates.....	171
C. SYMMETRY COORDINATE DEFINITIONS	178

REFERENCES.....	183
BIOGRAPHICAL SKETCH.....	191

Abstract of Dissertation Presented to the Graduate School
of the University of Florida in Partial Fulfillment of the
Requirements for the Degree of Doctor of Philosophy

INVESTIGATION OF HYDROGEN BONDING
IN STRONG NITROGEN BASES

By

Pierre Henri Chabrier

August 1998

Chairman: Willis B. Person
Major Department: Chemistry

A study of hydrogen-bonded complexes of HBr with pyridine derivatives has been carried out by systematically changing the substituent(s) of the pyridine, thus varying the proton affinity of the nitrogen base. Infrared absorption spectra have been obtained for matrix isolated complexes of HBr with pyridine, 4-chloropyridine, 3,5-dichloropyridine, 4-methylpyridine, 3,5-dimethylpyridine and 2,4,6-trimethylpyridine.

Vibrational analyses of the experimental spectra were performed using results from ab initio calculations in conjunction with Xtrapack, a normal coordinate program specifically written for this study, in order to decompose each normal mode into individual contributions from the symmetry coordinates to the potential energy (PEDs) and to the intensity (IDs).

All six hydrogen-bonded complexes were found to be "proton shared" type, based on the large frequency shift of the proton stretch from the isolated HBr (or NH^+ stretching

vibration in the protonated base). Except for the HBr:3,5-dichloropyridine complex, the frequency of the proton stretch was found to increase with the proton affinity of the base, indicating that the proton is transferred towards the nitrogen. These results were confirmed by the computed structures.

The proton stretch local oscillator, predicted to be very intense (up to 6000 km/mol for the complexes studied here), was shown to couple with some of the local modes of the substituted pyridine, dramatically increasing the intensity of these modes via intensity borrowing from the proton stretch. Comparisons of experimental and computed harmonic spectra showed that discrepancies as large as 50% exist in the frequency of the strongest band, and also revealed very different intensity patterns. The treatment of the force field we proposed, adjusting only the effective force constant of the proton stretch, produced results in remarkable agreement with the experiment.

CHAPTER I INTRODUCTION

The importance of hydrogen bonding in biological systems and the chemistry of life in general cannot be overemphasized. Early x-ray crystal diffraction studies, although not able to observe the electron density describing the hydrogen atom, led to at least two major discoveries pointing to the significance of hydrogen bonding: the spatial folding of polypeptides from the analysis of crystal structures of the amino acids¹ and the Watson-Crick base-pairing in the DNA double helix.² All known double helical structures of naturally occurring nucleic acids feature the Watson-Crick base-pair hydrogen bonding and are the basis for genetic coding in all living organisms. In the same way, the secondary structures of proteins, the α -helix and the β -pleated sheet, are also stabilized by hydrogen bonds. It was subsequently recognized that although hydrogen bonds are weaker than covalent bonds, they are the most important intra- and intermolecular cohesive forces, determining the three-dimensional folding and the modes of recognition and association of biological macromolecules.

Hydrogen bonding also plays a central role in a wide range of other chemical and physical phenomena, including the formation of the condensed phases.³ In 1920, Latimer and Rodebush⁴ recognized the existence of hydrogen bonds, stating that hydrogen could sometimes have a valence of two. Their qualitative description of liquid water gave one of the first examples of associated chains, i.e., intermolecular hydrogen bonds: "water...

may be made up of large aggregates of molecules continually breaking up and reforming under the influence of thermal agitation.”^(5, p1)

Many of today’s definitions of the hydrogen bond are based on the principle of the relative atomic electronegativities and originate from Pauling’s “Nature of the Chemical Bond.”⁶ A hydrogen bond is an attractive interaction between two closed-shell species that arises between a proton donor covalent pair A-H and a close-by acceptor B, where A and B are (highly) electronegative elements and B possesses a lone pair of electrons.⁷ In the direction of an A-H bond, the proton is increasingly descreened as A proceeds from left to right of the Periodic Table and its electric potential is increasingly positive. This gives rise to a dipole with a positive charge at the hydrogen end of the A-H bond. The hydrogen bond may then be described as the Coulombic interaction of the dipole with the excess electron density at the acceptor atom. It is, however, difficult to generalize this description to all types of hydrogen bonds. The hydrogen bond resembles a covalent bond with the electron pair shared equally between A and B when both A and B are very electronegative, while with weakly electronegative atoms, the interaction is primarily electrostatic.⁸ A broader definition, proposed by Pimentel and McClellan,⁵ ignores the nature of the donor and acceptor atoms: “a hydrogen bond is said to exist when 1) there is evidence of a bond, and 2) there is evidence that this bond specifically involves a hydrogen atom already bonded to another atom.”^(5, p6)

There are common criteria associated with the formation of hydrogen bonds. In particular, as the A-H...B interaction gets stronger, the A-H bond weakens while the H...B bond strengthens. This phenomenon translates into specific changes occurring in the vibrational spectra upon formation of hydrogen bonds:⁵

- 1) the frequency of the A-H stretching mode decreases;
- 2) the intensity of the A-H stretching mode increases.
- 3) the band width of the A-H stretching mode increases.
- 4) There are new low frequency modes associated with the A...B stretch and the A-H...B bend motions.

It is generally accepted that hydrogen bonds may be classified in three separate types. One type blends into the other as the interaction between A-H and B increases.

The first type is the normal or weak bond, also referred to as a traditional hydrogen bond. The vast majority of studies of hydrogen bonds reported in literature refer to this type of bond. The geometries of the two sub-units, the donor A-H and the acceptor B, are only slightly perturbed from their isolated monomeric forms and the complex can be symbolized by A-H...B. The bond energy is normally less than 20 kJ/mol and the H...B distance is much longer than the A-H distance.

The second type of hydrogen bond may be called "proton shared" or "quasi-symmetric" and is symbolized by A...H...B. In this type of bond, the A...H and H...B distances are comparable although the distance criterion alone is not sufficient for heterodimer complexes. Proton shared hydrogen bonds are strong with dissociation energies greater than 40 kJ/mol. The vibrational frequency of the hydrogen-bonded proton stretching mode is shifted very strongly from that of the A-H monomer or of the (H-B)⁺ cation. While the strongest proton shared hydrogen bonds, like F...H...F or O...H...O⁺, are transient species, proton shared hydrogen bonds also exist in larger neutral molecular complexes. They will be the focus of this dissertation.

Finally, the third type of hydrogen bond is the ionic hydrogen bond, with the hydrogen-bonded proton fully transferred to the acceptor. This often happens in the solid phase of some neutral complexes where the crystal field forces are relatively strong. These bonds be depicted by $A^-\cdots H-B^+$. The $H-B^+$ distance is now much shorter than the $A^-\cdots H$ distance. This type of bond has been widely studied in crystals by x-ray diffraction, neutron diffraction and nuclear magnetic resonance.⁵

The goal of this work is to present results, both theoretical and experimental, for complexes of hydrogen halides with strong nitrogen bases (substituted pyridines in this study). By systematically varying the substituent, it is expected that the base strength of the pyridine can be changed gradually over a wide range, thus spanning the entire range of proton transfer along the halide-nitrogen axis from the traditional $A-H\cdots N$ bonds, to the proton-shared $A\cdots H\cdots N$ bond, and finally to the ion pair $A^-\cdots H-N$. Figure 1-1 illustrates schematically the complexes studied here and the types of hydrogen bond that may be covered. Because the spectra for several complexes of HCl with substituted pyridines have already been acquired in our laboratory by Dr. Krystina Szczepaniak (most still unpublished) the focus of the present study will be on the series of complexes with HBr. Complexes of HF with the same bases have not yet been studied, but are expected to be examples of traditional hydrogen bonds. Until now, there have been very few combined theoretical and experimental studies of proton-shared hydrogen bonds; this work helps partially fill the gap.

The choice of substituted pyridines as nitrogen bases was motivated by several factors. These molecules are stable and expected to present a wide basicity range. Their C_{2v} symmetry, conserved upon formation of the complex, simplifies the ab initio

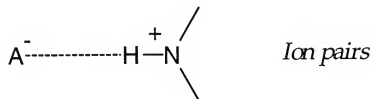
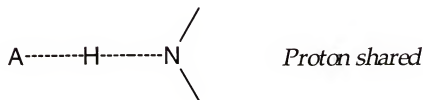
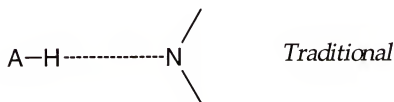
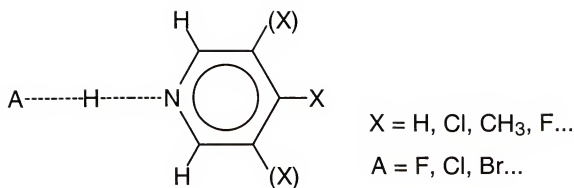


Figure 1-1. Schematic representation of complexes of hydrogen halides with substituted pyridines and the three types of hydrogen bond expected by changing the substituent(s).

computations. The complexes are stable and complications from different tautomers are not expected to be important.

The *ab initio* calculations were carried out by Dr. Janet E. Del Bene at Youngstown State University while the experimental spectra were obtained in our laboratory using low temperature matrix isolation infrared spectroscopy. In Chapter 2, a description of the experiment is given, discussing some of the difficulties and specific details associated with the study of isolated hydrogen-bonded complexes.

Chapter 3 presents the theoretical tools that were developed in Dr. Person's laboratory to allow multicomponent analysis of the vibrational spectra. Several aspects of the program, such as the transformation and the decomposition of the *ab initio* results and the possibility of re-computing the vibrational frequencies and intensities after modification of the force field, are presented.

Chapter 4 shows the results obtained for complexes of hydrogen bromide with different substituted pyridines. The experimental spectra are compared with, and interpreted in terms of the computed spectra. Both frequencies and intensities are considered for the interpretation of the fundamental modes of vibration. Force field treatments to explore reasons for discrepancies between theory and experiment are explained.

Chapter 5 examines the trends in the structural and spectroscopic properties of complexes as a function of proton donor and proton acceptor strengths. Experimental results showing the effects on the complex of different matrix environments are also presented.

CHAPTER II EXPERIMENTAL CONSIDERATIONS

A. Experimental Techniques

1. Brief Review of Fourier Transform Infrared Spectroscopy

Infrared spectroscopy has enjoyed a renewed popularity since the technology of solid-state devices and integrated circuits has advanced enough to develop small computers, and it is now used as a routine analytical tool as well as for “state of the art” research. In the late 60’s, the fast Fourier transform algorithm introduced by Cooley and Tukey⁹ was first applied to interferometry.¹⁰ The result was a dramatic reduction in the measurement time for a spectrum acquired interferometrically compared to a spectrum measured by a typical diffraction spectrometer.

The infrared electromagnetic spectrum is divided into three main regions. The near infrared region is the closest to the visible region and ranges from 12800 to 4000 cm^{-1} . The middle infrared region, where most of the vibrational transitions of molecular bonds occur, extends from 4000 to 200 cm^{-1} . The vibrational absorptions of the molecules and complexes presented in this work fall in this region. Finally, the far-infrared region covers the 200 - 10 cm^{-1} range.

A Fourier transform infrared (FTIR) spectrometer is basically a Michelson interferometer with a source and a detector. The broad band IR source is typically a Nernst glower heated by the passage of an electric current. The detector can be either a

thermocouple or a photodetector. The principle of this instrument can be found in many books and review.¹¹⁻¹⁴

2. Matrix Isolation

Matrix isolation was initially proposed for the investigation of unstable or short-lived species, by trapping them as isolated entities in an inert solid, or matrix. Its value in studying hydrogen bonding interactions was demonstrated in two classic papers from van Thiel, Becker and Pimentel.^{15,16} The matrix isolation technique, simultaneously introduced by Pimentel *et al*¹⁷ and by Norman and Porter,¹⁸ is conceptually quite simple. A gas mixture, containing the absorbing species and a high concentration of inert diluent gas, is condensed on a cold surface at a cryogenic temperature that must be low enough to solidify the isolant gas. The inert gas and the vapor of the species of interest can be either pre-mixed before depositing or co-deposited from separate inlets. The latter method was employed for most of the molecules and complexes studied in the present work.

The nature of the cold surface mentioned above depends on the type of spectroscopic measurement to be made. For mid-IR spectroscopy, the substrate must be transparent in this spectral region. A transmitting alkali halide window is usually employed. A reflecting metal mirror can also be used.

The choice of matrix material is also dictated by its transparency in the mid-IR and by its interaction with the solute. Noble gases are ideally suited as matrices since they have a low polarizability (i.e., they are weakly interacting hosts) and are totally transparent in the region of interest. Argon was the preferred matrix material for the complexes studied here because it is one of the least interacting hosts. Neon is less reactive but does not solidify at the temperatures reached by most closed-cycle helium

compressors (10 K). Other inert gases, like krypton or nitrogen were also used as matrix material for some studies of our hydrogen-bonded complexes.

One of the objectives of trapping species in inert matrices is to produce an environment that is comparable to the gas phase. Although the perturbation of the molecular energy levels by the matrix environment is small, small frequency shifts from the gas phase values are observed. These shifts, however, are much smaller than the analogous solvent shifts observed at room temperature in solution spectra.¹⁹ Since there is very little gas phase vibrational information available for strong hydrogen-bonded complexes it is not possible to evaluate quantitatively their matrix shift, as has been done for many transient molecules by Jacox.²⁰⁻²²

Another problem linked to matrix isolation may arise when the same species occupies different trapping sites in the matrix. Spectral lines can be inhomogeneously broadened or exhibit splittings that can complicate the interpretation of the spectrum. One way of distinguishing band splitting due to nearly degenerate transitions or to the interaction with different trapping sites is to repeat the experiment with different deposition conditions; for example, different matrix materials. The chances that similar alternative trapping sites will produce similar splittings in matrices made of different materials are very small.

In most matrix-isolation experiments, the Boltzmann population distribution at cryogenic temperatures (~ 10 K) implies that the species under investigation are in their ground electronic and vibrational states. The transitions observed in the mid-infrared region then correspond to the absorptions of radiation between the vibrational levels $v = 0$ and $v = 1$ of the electronic ground state. As a direct consequence, absorptions appear

sharper due to the absence of “hot” bands (transitions from higher vibrational levels). Also, because the matrix is rigid, molecules are usually not free to rotate. Hence, the spectrum is further simplified by the absence of rotational transitions. There are exceptions for small molecules like HCl, HBr, H₂O etc., but their rotational structures exhibit reversible temperature dependence since the population of the rotational energy levels changes as the temperature is increased.²³ These lines have been well studied and are easily recognized.

Transient species trapped in a rigid matrix are prevented from reacting or undergoing decomposition as would normally occur in the gas phase. Similarly, the matrix isolation of hydrogen-bonded complexes prevents self-association and other intermolecular interactions that would change the characteristics of the hydrogen bonds themselves. For instance, it is well known that mixing gaseous ammonia and hydrogen chloride rapidly forms the ionic salt NH_4^+Cl^- , where the hydrogen-bonded proton is transferred to the nitrogen. However, it is known^{24,25} that the proton is not transferred for the isolated $\text{NH}_3\text{:HCl}$ complex. The same behavior is expected for other strong hydrogen-bonded complexes. It is therefore necessary to study those complexes either in the gas phase or isolated in a matrix, since the intermolecular interactions between the complexes may be strong enough to form a crystal lattice. At this time, matrix isolation is by far the most practical technique for our study.

3. Formation of the Complex

The method used for the formation of the hydrogen-bonded complex is to generate it *in situ*. The association of two reactive species is often achieved by annealing (warming) the initial deposit of the matrix mixture on the cold window. Initially, the

molecules of acid and base are, for the most part, isolated in their monomeric form after depositing. When the deposition rate of the two monomers is slow enough compared to the growth of the matrix, the spectrum after depositing typically shows bands arising from absorptions of both the acid and the base with little or no trace of complex. The complex is subsequently formed by controlled diffusion of the monomers through the matrix.

The diffusion mechanism starts when the matrix is warmed to a temperature about 30% to 50% of the melting point,²⁶ but depends also on other factors. The matrix structure undergoes a rearrangement at the atomic level towards the most stable crystal structure. This annealing process, during which the matrix softens, particularly favors the formation of hydrogen-bonded complexes. Of course, unwanted associations also occur since the diffusion is mostly governed by random motions. Oligomers and weak hydrogen complexes with water impurities always form (there are always traces of water) but they are usually well known or are readily identifiable.

A more serious problem in the interpretation of the spectrum may arise from absorption bands by the two-to-one AH:AH:B complex, where AH is the acid and B the base. The concentration of this complex depends dramatically on the initial degree of isolation of the monomers. If the concentration of AH dimer is relatively high before annealing, then the probability of forming the 2:1 complex after annealing may be high. Successive annealing of the matrix to increasing temperatures can also produce excessive diffusion and possible formation of the 2:1 complex.

The temperature dependence of the diffusion rate can be expressed by:²⁶

$$R \propto \exp(-\Delta E / RT), \quad (2-1)$$

where ΔE is the activation energy for diffusion per mole of diffusing species. The energy ΔE is a function of the size, the shape and the mass of the diffusing species. It is also related to the relative energy of different sites in the lattice and thus depends on the matrix material chosen. It is not possible to evaluate precisely the activation energy but some simple qualitative remarks can be drawn from expression (2-1). Small diatomic molecules may show significant mobility when the matrix starts to lose its rigidity, but the diffusion of larger molecules, like pyridine or substituted pyridine, is expected to be significantly slower. The formation of higher aggregates of pyridine or higher order associations of the one-to-one complex is therefore less likely. This is very important because the strong intermolecular interactions of the complexes can lead to very large frequency shifts upon aggregation (see chapter 4).

Good isolation of the monomeric species can be attained with matrix to solute ratios, M/S, of 1000 or greater.²⁷ In theory, a molecule occupying a single substitutional site of a perfect crystal at a M/S ratio of 100 should be 99% isolated. In practice, the matrix is far from a perfect crystal and the number of matrix atoms displaced to accommodate the solute increases as the solute molecules become larger and the M/S ratio needed to keep the same probability of isolation increases dramatically.

Nitrogen impurities can also complicate the spectrum. It was shown for a variety of solutes trapped in Ar matrices that the interaction with nitrogen impurities can lead to the appearance of new absorption bands.²⁸⁻³³

B. Experimental Setup

The vacuum chamber, the deposit window and the locations of both the matrix gas inlet and sample inlet are shown in the schematic diagram, Figure 2-1. The chamber

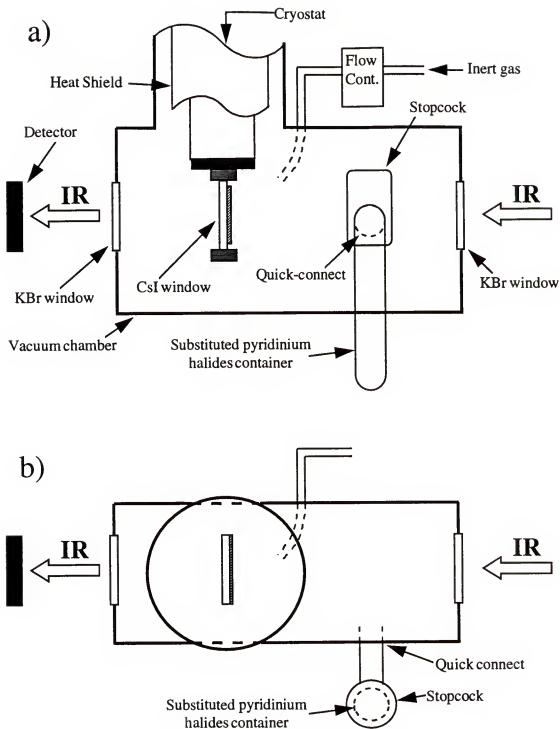


Figure 2-1. Details of the cryostat chamber for matrix isolation spectroscopic studies of infrared spectra of hydrogen-bonded complexes. The ionic salt, source of gaseous monomers, is kept in a closed container outside the vacuum chamber. a) Front view. b) Top view.

is evacuated by a combination of rotary and oil diffusion pumps. Typically, the cryostat chamber reaches pressures of about 10^{-6} torr without filling the liquid nitrogen trap, and about 5×10^{-7} cm⁻¹ when the trap is filled.

The cryogenic temperature of the deposit window was attained with a closed cycle helium refrigeration system (Displex Model DE-202 from APD Cryogenic, Inc.). With the compressor on, the cold finger attached to the end of the cryostat's second stage is cooled to 10 K. The temperature is monitored by a Pt/Au thermocouple attached to the copper holder of the cold window and connected to a temperature controller (model 9600-5, Scientific Instruments, Inc.). The pressure in the cryostat chamber during a normal experiment with both the helium compressor on and the liquid nitrogen trap filled is about 10^{-7} torr.

The infrared beam coming out from the spectrometer passes successively through an external KBr window, the matrix isolated sample deposited on a cold CsI window and another external KBr window. The beam is then focused on a Nicolet triglycine sulfate (TGS) detector.

The experimental infrared spectra were recorded with a Nicolet FT-IR spectrometer (model 740). The resolution of the instrument was set to 1 cm⁻¹ to considerably reduce the acquisition time without significant loss of spectral information (compared with the highest resolution, 0.3 cm⁻¹). Between 250 and 500 scans were made to record each spectrum.

One difficulty associated with matrix studies of hydrogen-bonded complexes is the need to deposit comparable molar concentrations of acid and base in the matrix. Published studies of matrix isolated complexes with nitrogen bases have been carried out

using the dual jet deposition method.^{25,34-46} Unfortunately, it is very difficult to control accurately the flow of both inlets. The relative concentrations of the two monomeric species are often different from what is expected. The deposition in excess of one of the two species can favor the formation of complexes with acid to base ratios of 2:1 or 1:2 instead of 1:1.

In order to partially avoid this problem, the source of gaseous monomers for all the complexes studied in this work was provided by the sublimation at room temperature of the corresponding ionic salt (for instance, pyridinium bromide provides vapors of pyridine and HBr). These salts were usually not available commercially and were synthesized in our laboratory by Dr. Barbara Galuska-Muga. The main advantage of this method is that the sublimation of the salt produces a vapor with a one-to-one ratio of acid and base. This procedure has also been used by Johnson and Andrews⁴⁷ for the study of FH:NH₃, a weakly bound complex.

As shown in Figure 2-1, the solid was kept in a container closed with a Teflon stopcock and located outside the cryostat chamber. This precaution was necessary to avoid continuous sublimation prior to and during the experiments. Indeed, some of these salts have a relatively high vapor pressure at room temperature and can sublime completely under high vacuum after a few minutes or hours. When the sublimation rate was too high, it was necessary to insert a Teflon needle valve (quick connect) between the container and the cryostat chamber. On the contrary, other salts had relatively low vapor pressures at room temperature and required heating.

With the exception of some monomer studies, the gaseous vapors were codeposited with the inert gas without prior mixing. The pressure of HBr and substituted

pyridine entering the cryostat chamber was controlled by the stopcock or the Teflon needle valve, depending on the salt. The flow of argon was regulated by a needle valve allowing a better control of the M/S ratio.

Although the vapor sublimed from the solid has a 1:1 ratio of acid to base, the ratio deposited into the matrix may be different. The different species may condense on the cold window (or on the metallic walls of the vacuum shroud) at different rates. It is expected however, that the M/S ratio is much closer to 1:1 than could be obtained from dual jet deposition.

The spectrum subsequent to matrix deposition was recorded at 10 K. The matrix was then annealed to about 30 K by turning off the helium compressor until the matrix warmed to the desired temperature. The sample was cooled back to 10 K and the spectrum was recorded again. The cycle of annealing to gradually increasing temperatures, cooling, and re-recording the spectrum was repeated several times.

C. Infrared Band Intensities and Concentrations

Accurate measurement of absolute vibrational intensities, even in the gas phase, is an extremely difficult problem. In addition, measurements in the matrix present some unique difficulties that are absent in the gas phase. However, the measurement of intensities is important to obtain molecular properties such as transition dipole moments and the polar characteristics of the molecule in general.

In some cases, intensities may turn out to be the most sensitive probe to assess some molecular properties. For instance, Huggins and Pimentel⁴⁵ have reported intensities for the stretching vibration $\nu(\text{CD})$ of deuterated chloroform, in a variety of solvents. Their findings showed that even though the frequency $\nu(\text{CD})$ exhibits little or

no solvent shift, there is a very large variation in intensity from one solvent to another. This variation can be attributed in part to intrinsic structural changes of the absorbing molecule due to different environments,⁴⁶ and in part to specific interactions solute/solvent of a charge transfer nature.^{48,49} In any case, the fact that the frequencies are almost unchanged “indicates that the band intensities are much more sensitive probes for structural and interaction studies than other parameters such as vibrational frequencies, bond lengths or nuclear quadrupole coupling constants.”^{27,p170}

The general expression for vibrational band intensity (the absolute integrated molar absorption coefficient) is given by:⁵⁰

$$A = \frac{1}{100 C \ell} \cdot \int_{\text{band}} \ln \left(\frac{I_0}{I} \right) dv, \quad (2-2)$$

where C is the concentration of the species from which the band originates, in mole liter⁻¹, ℓ is the pathlength, in cm, $\ln(I_0/I)$ is the absorbance. With these units, the band intensity is expressed in km mole⁻¹, a unit proposed by Person and Steele⁵¹ for its appropriate order of magnitude.

The intensity of the s^{th} fundamental vibration, is related to the transition dipole moment, μ_{01s} by:^{50,52}

$$A_s = \frac{8\pi^3}{3hc(4\pi\epsilon_0)} N_A v_s |\mu_{01s}|^2, \quad (2-3)$$

where h is Planck's constant, c the velocity of light, $4\pi\epsilon_0$ converts to SI units, N_A is Avogadro's number, v_s the wavenumber at the band center and μ_{01s} is the transition dipole moment for the s^{th} mode with:

$$|\mu_{01s}|^2 = \sum_{\alpha} |\mu_{01s}^{\alpha}|^2 \quad \text{and}, \quad (2-4)$$

$$\mu_{01\alpha}^{\alpha} = \int \Psi_{1\alpha} \hat{\mu}_{\alpha} \Psi_0 \, dv = \langle 1_{\alpha} | \hat{\mu}_{\alpha} | 0 \rangle. \quad (2-5)$$

Here, $\mu_{01\alpha}^{\alpha}$ is the α^{th} component of the transition dipole moment.

1. Determination of the Pathlength ℓ

The pathlength is probably the easiest parameter to evaluate. It can be readily obtained by monitoring the interference fringes as the matrix grows. Figure 2-2a illustrates the path difference (retardation) between two monochromatic rays. As the matrix grows in time, the retardation increases and the two rays will recombine constructively and destructively at the detector. With a broadband source there is an infinity of interference patterns, functions of the thickness ℓ of the matrix. At the end of the matrix deposition, the thickness ℓ is fixed and for each individual wavelength λ , the corresponding interference pattern yield a single amplitude value. In the frequency domain, these interferences appear like the spectra presented in Figure 2-2b.

The pathlength ℓ is obtained directly from:

$$2n\ell = \Delta\bar{\nu} / N, \quad (2-6)$$

where $\Delta\bar{\nu}$ is the frequency difference (in cm^{-1}) between two maxima, N is the number of fringes between these two maxima, and n is the refractive index of the pure matrix (for argon, $n_{\text{Ar}} = 1.41$).⁵³ Observation of Figure 2-2b reveals that as the matrix grows in time, there is a visible superposition of two different interference fringes. The narrow fringes correspond to the thicker deposit on the front side of the CsI window towards which the inert gas inlet is oriented. The larger fringes correspond to the thinner deposit on the back side of the window. The pathlength ℓ is of course the sum of both thicknesses.

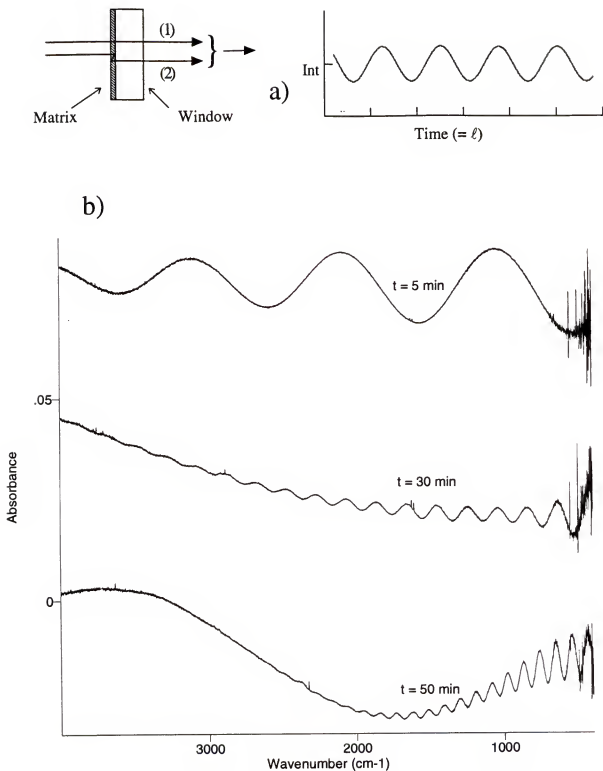


Figure 2-2. Interference fringes from the passage of light through the matrix sample. a) From a monochromatic source. Interferences are shown as a function of the thickness of the matrix. b) From a broadband IR source. Actual spectra recorded at different times (i.e. different thicknesses) during the matrix deposition.

2. Determination of Integrated Relative Intensities

Computers dramatically facilitate the determination of integrated absorbances. The baseline of the spectrum is corrected in order to remove the interference fringes and the scattering. Particular care must be taken for bands that are broad enough to cover one fringe because errors in the baseline correction can lead to quite different values of integrated intensities. Figure 2-3 illustrates the extrapolation that must be done when choosing points for the new baseline. By determining the average frequency difference between two maxima, it is possible to set the position of the maximum of the fringe that lies under the band or group of bands. Errors made at the base of a band are critical, especially if several bands overlap.

Direct integration over each band of the spectrum can then be carried out, although it is often necessary to deconvolute overlapping bands with a curve fitting procedure. For each band, the relative integrated intensity provides the term

$$\int_{\text{band}} \ln\left(\frac{I_0}{I}\right) d\nu \text{ in Eq. (2-2) for a given concentration and thickness of the matrix. This}$$

analysis of the spectrum was accomplished with the Grams/32 program.⁵⁴

3. Determination of the Concentration

The concentration was evaluated using Eq. (2-2) after determining the pathlength and the integrated intensities as explained in the previous sections. The molar absorption coefficients A_s were provided by the ab initio calculation since experimental values for these coefficients are not available, except for very limited number of molecules. In principle, using any mode of vibration of the same species should yield the same

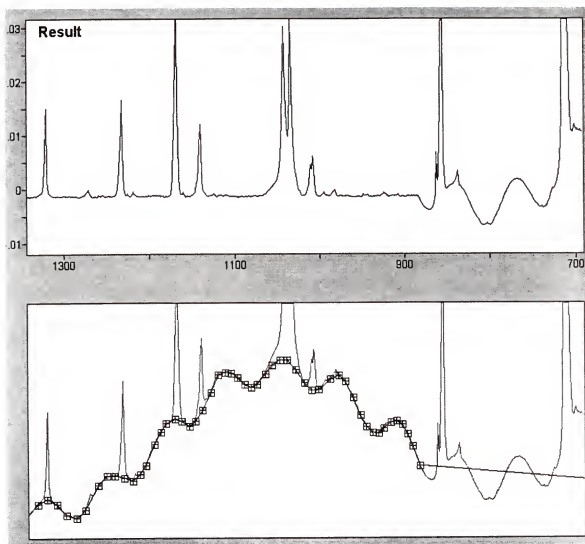


Figure 2-3. Example of baseline correction applied to remove the interference fringes. The top spectrum shows the result for the baseline corrected region. The bottom trace shows the original spectrum and correction points. Notice the extrapolation needed when the width at the base of a peak becomes as large as a fringe.

concentration. In reality, errors of measurements in integrated intensities and inaccurate computed intensities can produce quite different results. There has been much debate about the accuracy of calculated intensities and whether they can be used reliably. Comparison of computed and experimental (when available) absolute intensities reveals that computed intensities have the right order of magnitude. These values are dependable enough to provide an estimation of the concentration.

Because of the errors mentioned above, each band of the same species can produce a different concentration. Thus, the determination of the concentration of the hydrogen-bonded complex is accomplished slightly differently by taking the sum of the molar absorption coefficients of all the intense modes and the sum of the experimental integrated intensities attributed to the one-to-one complex:

$$C = \frac{\sum \int_{\text{band}} \ln\left(\frac{I_0}{I}\right) dv}{100\ell \sum A_s} . \quad (2-7)$$

This procedure will be justified later, in Chapter 4.

CHAPTER III TOOLS FOR VIBRATIONAL ANALYSIS

One purpose of this work is to show the importance of a combined theoretical and experimental approach to the understanding of strong hydrogen bonding. The computational tools employed here for the prediction and interpretation of the observed infrared spectra consist of two separate programs.

The first is the commercially available Gaussian 92 and 94 series of computer programs.⁵⁵ The Gaussian output logfiles provide numerous data that are useful for this study: for example, equilibrium geometry, energy, Cartesian force constants, frequencies, infrared intensities, Cartesian displacements and dipole derivatives contained in the archive. The ab initio calculations were carried out at the Ohio Supercomputer Center on a Cray Y-MP8/864 by Dr. Janet E. Del Bene, and they will not be discussed in this dissertation. Here, we may simply note that these calculations included electron correlation effects and were performed at the second order Møller-Plesset perturbation theory (MBPT(2) = MP2) using the split-valence plus polarization 6-31+G(d,p) basis set augmented by diffuse functions on non-hydrogen atoms. This level of theory is believed^{56,57} to be the minimum required to give “reasonable” results for vibrational properties of hydrogen-bonded complexes, and is the maximum level that is practical for complexes as large as those studied here.

The second tool is the Xtrapack program written for this study and specifically designed for our needs. Xtrapack is a multilanguage program based on the Pack program⁵⁸ and allows the “dissection” of the vibrational spectrum into separate contributions to the observed frequencies and intensities. The flowchart diagram of the Fortran code is given in Appendix A. Some of Xtrapack’s features will be explained in more detail in the following sections.

A. Coordinate Systems

Transformation between different coordinate systems is one of the most crucial functions of Xtrapack. Displacement coordinates that describe the vibrational motions are given by Gaussian as a set of $3N$ mass-weighted Cartesian coordinates, where N is the number of atoms. These coordinates q_i are related to the $3N \times 1$ column vector of the ordinary Cartesian displacement coordinates X_i by:

$$\mathbf{q} = \mathbf{M}^{1/2} \mathbf{X}, \quad (3-1)$$

where \mathbf{M} is the $3N \times 3N$ diagonal matrix of the masses. Throughout this chapter, bold letters will designate matrices and vectors.

The $(3N - 6)$ normal coordinates \mathbf{Q} (for non-linear molecules) describing the actual molecular motions are linear combinations of these displacement coordinates that are unknown until the secular equation has been solved. Once found, they can be correlated with the mass-weighted Cartesian coordinates by the inverse of the transformation matrix \mathbf{I} :

$$\mathbf{Q} = \mathbf{I}^{-1} \mathbf{q}, \text{ or } \mathbf{q} = \mathbf{I} \mathbf{Q}. \quad (3-2)$$

Given the dimension of the vectors \mathbf{Q} and \mathbf{q} , \mathbf{I} is a $3N \times (3N - 6)$ matrix. It can be shown⁵⁹ that the transformation matrix \mathbf{I} is orthogonal since:

$$\mathbf{I}^t = \mathbf{I}^{-1} \text{ and } \mathbf{I}^t \mathbf{I} = \mathbf{E}. \quad (3-3)$$

Each row of \mathbf{I}^t (transpose of \mathbf{I}) is of particular interest because it provides the coefficients of the mass-weighted Cartesian coordinates that define the corresponding normal coordinates Q_s . These coefficients are given in the output logfile of Gaussian and allow us to visualize the motion of each atom for every normal vibration. Such illustrations were drawn throughout this work using the Animol program.⁶⁰

Although the displacements and force constants in Cartesian coordinates are very useful, the properties do not relate directly to the structure of the molecule. In order to compare the force constants for bonds in a molecule with those for the perturbed molecule in a complex, it is more useful to express the force constants in valence coordinates such as internal and symmetry coordinates.

Five basic internal coordinates are usually sufficient to describe all internal motions of the molecule.^{59,61}

- (1) Bond stretching.
- (2) In-plane angle bending.
- (3) Out-of-plane angle bending.
- (4) Torsion (change in the dihedral angle between the two planes determined by three consecutive bonds).
- (5) Linear bending (change in the angle between two bonds connecting three atoms with a linear geometry at equilibrium).

The definitions of these coordinates for the molecule being studied are required by Xtrapack. It is important for the internal coordinates to be independent of the atomic masses in order to insure that the force constants are unchanged for different isotopic species. The transformation between Cartesian and internal coordinates can be approximated for small amplitudes of vibration by a set of linear transformations expressed in matrix notation by:

$$\mathbf{R} = \mathbf{B}_R \mathbf{X}. \quad (3-4)$$

Here \mathbf{B}_R is a $? \times 3N$ matrix since for non-trivial molecules, there are generally more than $(3N - 6)$ internal coordinate definitions. The “?” used here for the dimension of \mathbf{R} is an integer greater than $(3N - 6)$ and gives the number of internal coordinates. The \mathbf{R} vector is user-defined and must be provided to Xtrapack in one of the required input files (see Appendix B). As long as \mathbf{R} defines completely all internal motions (requiring $? \geq (3N - 6)$), these coordinates constitute a valid set. The \mathbf{B}_R matrix is constructed by Xtrapack based on the “s-vector method”.^{62,63}

Pulay⁸ has emphasized the importance of using a non-redundant set of coordinates in setting up the vibrational problem and calculating the vibrational frequencies. This set must also be complete, i.e., the number of coordinates should be equal to the number of vibrational degrees of freedom. Thus, $(3N - 6)$ symmetrized internal coordinates S_i , or “symmetry” coordinates, can be expressed as linear combinations of the internal coordinates:

$$\mathbf{S} = \mathbf{U} \mathbf{R}, \quad (3-5)$$

where \mathbf{U} is a $(3N - 6) \times ?$ matrix that is constructed using the symmetry of the molecule studied. An example showing how such a matrix may be set up is given in Appendix B

for HBr:NH_3 (C_{3v}), a complex not discussed further in this dissertation but whose reduced number of vibrations (12 compared with 33 for HBr:Pyridine) greatly simplifies the illustration.

The relation between symmetry and Cartesian coordinates is obtained directly by inserting equation (3-4) into (3-5):

$$\mathbf{S} = \mathbf{U} \mathbf{B}_R \mathbf{X} = \mathbf{B} \mathbf{X}. \quad (3-6)$$

The product $\mathbf{U} \mathbf{B}_R$ defines the $(3N - 6) \times 3N$ Wilson \mathbf{B} matrix. Its relevance will emerge in the following sections.

Finally, the $(3N - 6) \times (3N - 6)$ normal coordinate transformation matrix \mathbf{L} defines the transformation from the vector \mathbf{S} of the symmetry coordinates to the vector \mathbf{Q} of the normal coordinates:

$$\mathbf{S} = \mathbf{L} \mathbf{Q}. \quad (3-7)$$

The determination of the \mathbf{L} matrix and its use in the conversion from observable parameters to meaningful molecular parameters is given in the next section.

B. Force Field in Internal and Symmetry Coordinates

As previously mentioned, the ab initio force field generated by the Gaussian program is expressed in Cartesian coordinates. When using this coordinate system, the theoretical results, for example the frequencies, can be compared with the experiment only in the final stage. In internal or symmetry coordinates, the potential energy is partitioned into dominant diagonal terms and less significant cross-terms. This concept is lost in Cartesian coordinates since the diagonal force constants are not necessarily dominant. The force constants in Cartesian coordinates do not provide information (at the molecular level) as valuable as that from the symmetry or internal force constants.

The transformation from the $3N \times 3N$ Cartesian force constant matrix \mathbf{F}_X into the $(3N - 6) \times (3N - 6)$ symmetry force constant matrix \mathbf{F}_S is expressed by:

$$\mathbf{F}_S = (\mathbf{B}^t)^{-1} \mathbf{F}_X \mathbf{B}^{-1}. \quad (3-8)$$

A serious complication arises from the fact that the \mathbf{B} matrix, in Equation (3-6), is not square and thus cannot be inverted. One solution to this problem is to modify \mathbf{B} to make it square and non-singular by adding the coordinates describing the three translations and the three rotations to the definition of \mathbf{S} .⁵⁹ However, this process can be avoided by introducing the “pseudo-inverse” \mathbf{A} matrix of the non-square \mathbf{B} matrix, defined by:

$$\mathbf{X} = \mathbf{A} \mathbf{S} \text{ and } \mathbf{A} \mathbf{B} = \mathbf{E}_{3N}, \quad (3-9)$$

where \mathbf{E}_{3N} is the $3N \times 3N$ identity matrix.

The preliminary step in finding the \mathbf{A} -matrix is to calculate the inverse kinetic energy matrix, also known as the Wilson “ \mathbf{G} ” matrix:⁵⁹

$$\mathbf{G} = \mathbf{B} \mathbf{M}^{-1} \mathbf{B}^t, \quad (3-10)$$

where \mathbf{M}^{-1} is the matrix of the reciprocal masses. Here, \mathbf{G} is a $(3N - 6) \times (3N - 6)$ matrix in terms of the symmetry coordinate. Multiplying equation (3-10) on the right by the inverse of \mathbf{G} gives:

$$\mathbf{G} \mathbf{G}^{-1} = \mathbf{E}_{3N-6} = \mathbf{B} \mathbf{M}^{-1} \mathbf{B}^t \mathbf{G}^{-1}, \quad (3-11)$$

Note that this last expression requires that the \mathbf{G} matrix is not singular, which in turn requires the symmetry coordinates to be linearly independent. By identification of expression (3-11) with the product $\mathbf{B} \mathbf{A} = \mathbf{E}_{3N-6}$, the $3N \times (3N - 6)$ “inverse” \mathbf{A} matrix is:

$$\mathbf{A} = \mathbf{M}^{-1} \mathbf{B}^t \mathbf{G}^{-1}, \quad (3-12)$$

and is so computed by the Xtrapack program.

After evaluating the transpose \mathbf{A}^t , the symmetry force constant matrix \mathbf{F}_S can be directly obtained:

$$\mathbf{F}_S = \mathbf{A}^t \mathbf{F}_X \mathbf{A}. \quad (3-13)$$

The force field is presented to the user in this form and, if desired, adjustments can be made to obtain new values of the elements of \mathbf{F}_S . Note that \mathbf{F}_S is block-diagonal with each block corresponding to coordinates belonging to one symmetry species. Of course, the force constants \mathbf{F}_R expressed in internal coordinates can also be calculated. The \mathbf{F}_R matrix is obtained from the symmetry force constants evaluated in (3-13) and the transformation matrix \mathbf{U} from equation (3-5):

$$\mathbf{F}_R = \mathbf{U}^t \mathbf{F}_S \mathbf{U}. \quad (3-14)$$

Here \mathbf{F}_R is a $? \times ?$ matrix, where $?$ is the number of internal coordinates.

C. Solutions of the Secular Equation

This section presents a brief description of how the vibrational problem is set up in Xtrapack and how its solutions can lead to the vibrational frequencies and the transformation matrix \mathbf{L} . To do so, Xtrapack employs the method of Miyazawa.⁶⁴ In the symmetry coordinate system, the inverse kinetic energy and the potential energy become respectively:

$$(2T)^{-1} = \dot{\mathbf{S}}^t \mathbf{G} \dot{\mathbf{S}}, \quad (3-15)$$

$$2V = \mathbf{S}^t \mathbf{F}_S \mathbf{S}, \quad (3-16)$$

where $\dot{\mathbf{S}}$ is the symmetry coordinate velocity vector. The first step in solving this problem is to diagonalize the \mathbf{G} matrix. Since \mathbf{G} is real symmetric, it is possible to apply

an iterative procedure such as the Jacobi method^{65,66} which is often used for computer programs:

$$\mathbf{D}^t \mathbf{G} \mathbf{D} = \mathbf{T}, \quad (3-17)$$

where \mathbf{D} is the orthogonal matrix of eigenvectors and \mathbf{T} is the matrix of eigenvalues.

Expression (3-17) can be rewritten:

$$\mathbf{G} = \mathbf{D} \mathbf{T} \mathbf{D}^t = \mathbf{D} \mathbf{T}^{1/2} \mathbf{T}^{1/2} \mathbf{D}^t = \mathbf{W} \mathbf{W}^t, \quad (3-18)$$

where $\mathbf{W} = \mathbf{D} \mathbf{T}^{1/2}$ is a matrix that transforms the symmetry coordinates \mathbf{S} into an intermediate set of coordinates \mathbf{Y} in which \mathbf{G} is the identity matrix:

$$(2\mathbf{T})^{-1} = \dot{\mathbf{Y}}^t \mathbf{W}^t \mathbf{G} \mathbf{W} \dot{\mathbf{Y}} = \dot{\mathbf{Y}}^t \mathbf{E} \dot{\mathbf{Y}} \text{ and} \quad (3-19)$$

$$\mathbf{S} = \mathbf{W} \mathbf{Y}. \quad (3-20)$$

By inserting Eq. (3-20) into Eq. (3-16), the potential energy is expressed by:

$$2V = \mathbf{Y}^t \mathbf{W}^t \mathbf{F}_S \mathbf{W} \mathbf{Y} = \mathbf{Y}^t \mathbf{H} \mathbf{Y}. \quad (3-21)$$

The second step is then to find an orthogonal matrix \mathbf{C} which diagonalizes \mathbf{H} into the matrix of frequency parameters Λ :

$$\mathbf{C}^t \mathbf{H} \mathbf{C} = \mathbf{C}^t \mathbf{W}^t \mathbf{F}_S \mathbf{W} \mathbf{C} = \Lambda. \quad (3-22)$$

The eigenvalues Λ can also be called “normal force constants” since in the normal coordinate system \mathbf{Q} , the potential energy is:

$$2V = \mathbf{Q}^t \Lambda \mathbf{Q}. \quad (3-23)$$

Therefore, the diagonalization procedure performed by Xtrapack on \mathbf{H} provides both the eigenvalues Λ and the eigenvectors \mathbf{C} which then can produce the transformation matrix \mathbf{L} introduced in Eq. (3-7) by comparison of Eq. (3-16) and Eq. (3-23) :

$$\mathbf{L} = \mathbf{W} \mathbf{C}. \quad (3-24)$$

The vibrational frequencies ν_s (cm^{-1}) are related to the the frequency parameters λ_s ($\text{u}^{-1} \text{mdyn } \text{\AA}^{-1}$), elements of the diagonal matrix Λ , by:

$$\nu_s = \frac{\sqrt{N_{\text{Av}} \times 10^5 \lambda_s}}{2\pi c} = 1302.791 \times \sqrt{\lambda_s} . \quad (3-25)$$

D. Potential Energy Distributions

The eigenvalues of the secular equation are already provided by the Gaussian logfile in the form of vibrational frequencies. However, the logfile does not provide any information on the actual contributions from each symmetry coordinate to different normal coordinates of the molecule. In particular, it is usual^{67,68} to evaluate the percentage contribution from these coordinates to the potential energy of a normal mode Q_s . The construction of the potential energy distributions (PEDs) in Xtrapack is explained below.

As shown in the previous section, the potential energy can be expressed in terms of the normal coordinates Q_s as:

$$2V = \mathbf{Q}^t \Lambda \mathbf{Q} = \sum_s \lambda_s Q_s^2 . \quad (3-26)$$

By replacing Eq. (3-07) into Eq. (3-26) it can be seen that:

$$\Lambda = \mathbf{L}^t \mathbf{F}_S \mathbf{L} , \quad (3-27)$$

or expanding Eq. (3-27), each eigenvalue, or frequency parameter, is given by:

$$\lambda_s = \sum_i \sum_j L_{js} L_{is} F_{Sij} . \quad (3-28)$$

In this last equation, the upper case subscript “s” in F_S should not be confused with the lower case subscript “s” which designates a particular mode Q_s . The F_{Sij} are the elements of the symmetry force constants matrix F_S presented earlier. The contribution from the j^{th}

symmetry coordinate to the potential energy of the normal mode Q_s is then found by removing the summation over j :

$$P_{sj} = L_{js} \sum_i L_{is} F_{sij} . \quad (3-29)$$

This contribution is usually expressed as a percentage. Thus, a single PED value computed by Xtrapack corresponds to an individual contribution P_{sj} from the j^{th} symmetry coordinate divided by the s^{th} eigenvalue λ_s :

$$\text{PED}_{sj} = 100 \times \frac{P_{sj}}{\lambda_s} . \quad (3-30)$$

The PEDs are usually positive and add up to 100% for each mode. However, when the symmetry coordinates are not defined to be exactly orthogonal (which is often the case for non-trivial molecules such as pyridine) a single contribution (PED_{sj}) may be negative or greater than 100%. In order to avoid these extreme values, it would be necessary to use higher order redundancy conditions for the construction of the symmetry coordinates.

E. Intensity Distributions

A decomposition similar to that of the potential energy presented above can be carried out for the intensity of each fundamental vibration. The intensity distributions (IDs) are found by examining the dipole moment derivatives with respect to the internal (symmetry) coordinate displacements. This dissection method allows one to see how much of the observed infrared intensity for a particular mode comes from each symmetry coordinate.

The dipole derivatives are provided in the archive of the Gaussian logfile and are rearranged by the Xtrapack program into a tensor form known as the atomic polar tensor (ATP):⁶⁹⁻⁷¹

$$\mathbf{P}_\alpha = \begin{pmatrix} \frac{\partial p_x}{\partial x_\alpha} & \frac{\partial p_y}{\partial x_\alpha} & \frac{\partial p_z}{\partial x_\alpha} \\ \frac{\partial p_x}{\partial y_\alpha} & \frac{\partial p_y}{\partial y_\alpha} & \frac{\partial p_z}{\partial y_\alpha} \\ \frac{\partial p_x}{\partial z_\alpha} & \frac{\partial p_y}{\partial z_\alpha} & \frac{\partial p_z}{\partial z_\alpha} \end{pmatrix} \quad (3-31)$$

where $(x_\alpha, y_\alpha$ and $z_\alpha)$ are the Cartesian coordinates of the α^{th} atom, and $(p_x, p_y$ and $p_z)$ are the Cartesian components of the total dipole moment.

The 3×3 ATPs for the atoms are juxtaposed to form the $3 \times 3N$ Cartesian polar tensor \mathbf{P}_X for the molecule. This polar tensor \mathbf{P}_X is then transformed into the $3 \times (3N - 6)$ polar tensor \mathbf{P}_Q expressed in terms of the normal coordinates, using Eq. (3-7) and Eq. (3-9):

$$\mathbf{P}_Q = \mathbf{P}_X \mathbf{A} \mathbf{L}. \quad (3-32)$$

The intensity (in km/mol) for each mode is then directly evaluated from:⁷²

$$A_s = \frac{N_A \pi}{(4\pi\epsilon_0)3000c} \sum_\alpha \left| \frac{\partial p_\alpha}{\partial Q_s} \right|^2 = K \times (\mathbf{P}_Q^\dagger \mathbf{P}_Q)_{ss}. \quad (3-33)$$

where ϵ_0 is the vacuum permittivity, $(\partial p_\alpha / \partial Q_s)$ is expressed in $e/\text{\AA}$, $K = 974.9$ and α designates the Cartesian components (x, y , and z). It is clear from equation (3-32) that any modification to the force field will change the eigenvectors \mathbf{L} of the secular equation and thus the polar tensor \mathbf{P}_Q . However, the total molecular intensity (ΣA_s) will remain unchanged. It will be shown in Chapter 5 that changing two constants (and their couplings) in the ab initio force field affects the frequencies of the fundamental

vibrations, but that the intensities of individual modes often reflect an even greater change.

In order to evaluate the contribution of each symmetry coordinate participating in one mode of vibration to the intensity A_s , it is necessary to express Equation (3-31) in terms of a polar tensor in symmetry coordinates \mathbf{P}_s . Given the relation $\mathbf{P}_Q = \mathbf{P}_s \mathbf{L}$, the intensity of the s^{th} mode can be written:

$$A_s = K \sum_{\alpha} \left[\sum_k \left(\frac{\partial p_{\alpha}}{\partial S_k} \right) L_{ks} \right]^2, \quad (3-34)$$

or in matrix notation,^{69,70}

$$A_s = K \times \left(\mathbf{L}^t \mathbf{P}_s^t \mathbf{P}_s \mathbf{L} \right)_{ss} = K \times \sum_{\alpha} \left(\sum_k \left(L_{sk}^t P_{s\alpha}^t \right) \sum_l \left(P_{s\alpha} L_{ls} \right) \right), \quad (3-35)$$

By collecting the terms arising from the k^{th} symmetry coordinate, and by using the definition of the transpose $L_{sk}^t = L_{ks}$, the ID of the s^{th} mode can be expressed as:

$$ID_{ks} = K \times L_{ks} \sum_{\alpha} \left(P_{s\alpha} \sum_l \left(P_{s\alpha} L_{ls} \right) \right). \quad (3-36)$$

This is the contribution from the k^{th} symmetry coordinate to the intensity A_s of the s^{th} normal mode, i.e. $\sum_k ID_{ks} = A_s$.

Xtrapack does not present the IDs as percentages since the intensity A_s of some normal modes is exactly zero. IDs are given in km/mol.

F. Atomic Cartesian Displacements

Another useful way of visualizing the normal modes of vibration is to calculate the corresponding Cartesian displacement for each atom of the molecule. As mentioned

earlier, these displacements are available through the Gaussian output logfile and can be visualized by the Animol program. However, if changes are made to the force constant matrix, the eigenvectors will be altered from their original values and as a consequence, the atomic displacements of each mode will also be different. The representation of such displacements before and after modification of the force field will be illustrated in Chapter 4.

From replacing Eq. (3-7) into Eq. (3-9), the relation between Cartesian and normal coordinates can be written:

$$\mathbf{X} = \mathbf{A} \mathbf{L} \mathbf{Q}. \quad (3-37)$$

The i^{th} row of the $(\mathbf{A} \mathbf{L})$ matrix contains the coefficients of the normal coordinates contributing to i^{th} Cartesian coordinate. Hence, the s^{th} column of $(\mathbf{A} \mathbf{L})$ contains the contribution of each Cartesian coordinate to the s^{th} mode. The $(3N - 6) \times 3N$ matrix of the normalized displacements is then given by:

$$\Delta = \mathbf{N}^t (\mathbf{A} \mathbf{L})^t = (\mathbf{N} \mathbf{A} \mathbf{L})^t, \quad (3-38)$$

where \mathbf{N} is the $(3N - 6) \times 1$ column vector of the normalization factors:

$$N_s = \frac{1}{\sqrt{\sum_j^{3N} (\mathbf{A} \mathbf{L})_{sj}^2}}. \quad (3-39)$$

The new displacements are saved normalized and in the exact same order as in the Gaussian logfile.

CHAPTER IV INVESTIGATION OF SUBSTITUTED PYRIDINE COMPLEXES WITH HYDROGEN BROMIDE

A. The HBr:pyridine Complex

1. Infrared Spectra of Pyridine

The experimental infrared spectra were measured for pyridine isolated in an argon matrix at 10K, in the gas phase at 300K and in the solid phase at 10K. They are presented in Figures 4-1 and 4-2 along with the computed spectrum at the MP2/6-31+G(d,p) level of theory. The experimental procedure required for the acquisition of the vapor spectrum was different from that explained in Chapter 2. The container with liquid pyridine was evacuated for a very short time (< 10 s) with a rotary pump in order to remove as much water as possible. After recording the background at room temperature and closing the diffusion pump, the container was opened and the cryostat chamber was filled with pyridine vapor at a pressure greater than 1 torr (limit of the primary gauge); the vapor pressure of pyridine at room temperature is about 20 torr. The spectrum was subsequently recorded using the cryostat as a cell of about 10 cm pathlength.

The solid phase spectrum was obtained by depositing the vapor from the same container on a CsI window cooled to 10K. The sample was then warmed to 220K so that the amorphous pyridine changed into a crystalline phase. Indeed, the difference in bandwidths between the glass and the crystal phase can be dramatic. The sample was cooled back to 10K and the spectrum recorded.

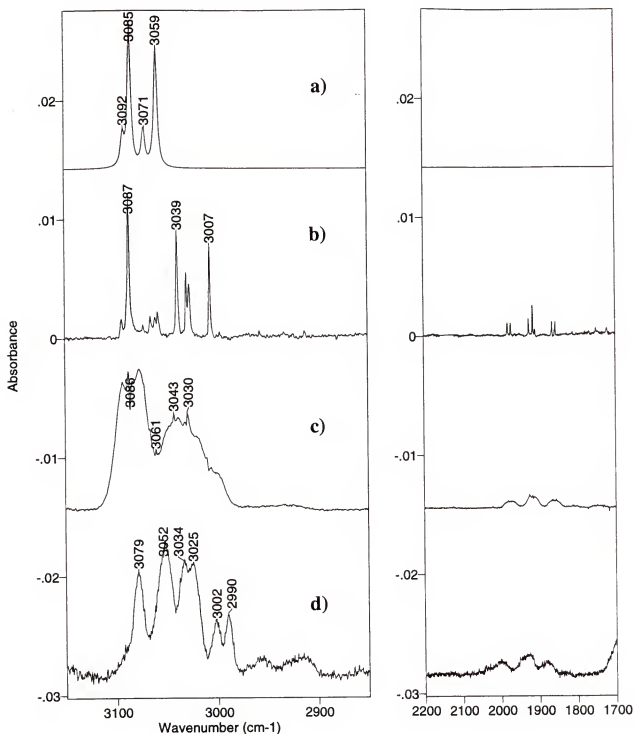


Figure 4-1. Infrared spectra of pyridine in the region from 3150 to 2850 cm^{-1} . The region from 2200 to 1700 cm^{-1} shows some strong overtones and combinations. a) Computed MP2/6-31+G(d,p). b) Isolated in an argon matrix at 10 K (baseline corrected). c) Gas phase at 300 K. d) Solid phase at 10 K.

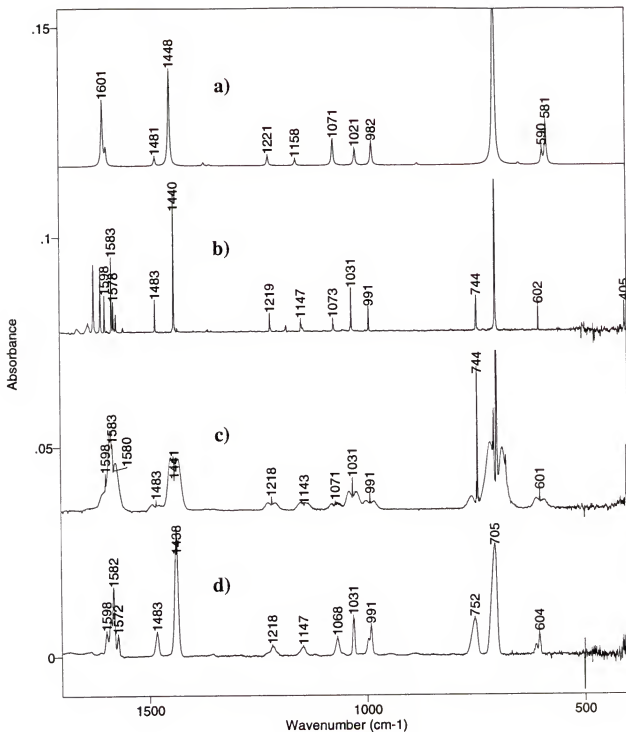


Figure 4-2. Infrared spectra of pyridine in the region from 1700 to 400 cm^{-1} . The strongest band around 700 cm^{-1} is off-scaled in order to better view the weaker ones. a) Computed MP2/6-31+G(d,p). b) Isolated in an argon matrix at 10 K (baseline corrected). c) Gas phase at 300 K. d) Solid phase at 10 K.

In the matrix studies argon was premixed with pyridine vapor and the mixture was condensed on the cold CsI window. The ratio of pyridine to argon in the resulting matrix was usually less than 1:1000. The condensed matrix was annealed several times in order to form matrix isolated pyridine complexes with impurities, mostly water, and self-associated. It is necessary to recognize the absorption by these species when studying the HBr:pyridine complex.

The calculated infrared spectrum was converted by the Animol program⁶⁰ from the ab initio output logfile. The frequencies above 2000 cm^{-1} were scaled by 0.942 and the rest by 0.970 in order to bring the calculated values into reasonable agreement with the experimental spectra. These values were found⁷³ to be the most appropriate at this level of theory when compared with experimental results for pyridine. Although the frequency of each individual mode of vibration could be scaled by a different factor, all calculated frequencies of the monomers will be scaled, throughout this work, by these two constants.

Observation of Figures 4-1c and 4-2c shows that the vapor-phase band envelopes seriously overlap in some congested regions. In addition to the 24 infrared active fundamentals there are more than 200 IR-active binary combination-tones,⁷⁴ and some can enter in Fermi resonance, especially in the C-H stretching region ($3000 - 3100\text{ cm}^{-1}$). In contrast, the fundamentals and most of the Fermi resonances are sharply defined in the matrix spectrum (Figure 4-1b). Fermi resonances and combination bands will not be discussed for pyridine. It is clear that the frequencies marked for the peak of the Q branch (or at the minimum band center) are almost identical with those for the peak absorption in the matrix spectrum. The average frequency difference between bands in

the gas phase and matrix spectrum is less than 1 cm^{-1} . There is therefore no significant environmental (“matrix”) effect on the frequencies and intensities of pyridine isolated in an argon matrix. Comparison of the solid and the gas phase spectra (Figure 4-2c and 4-2d) yields an average frequency difference of about 4 cm^{-1} . While this effect is still small, the bandwidths are much larger than those of the matrix spectrum. Fermi resonance effects as well as some fundamentals are now not clearly visible as separate peaks because of band overlaps.

2. Vibrational Analysis of Pyridine

The vibrations of pyridine have been studied both theoretically and experimentally by many workers.⁷⁴⁻⁹³ The spectral assignment is well known and relatively non-controversial. It is not our intent to re-assign pyridine but rather to verify that our observed spectra and calculations produce a consistent assignment agreeing with those already published, thus establishing a reliable procedure for other compounds studied in this work. Here, the emphasis will be put on the comparison of the experimental spectrum with the theoretical prediction at the MP2/6-31+G(d,p) level of theory.

Pyridine has C_{2v} symmetry, with 27 fundamental vibrations: 19 in-plane ($10a_1 + 9b_2$) and 8 out-of-plane ($3a_2 + 5b_1$). Modes with a_2 symmetry are inactive in infrared. Table 4-1 summarized the assignment of the observed frequencies in matrix, gas and solid phases, compared with the ab initio results. The experimental absolute intensities were obtained by multiplying the relative integrated intensities of each band by:

$$R = \frac{\sum_{\text{All Bands}} A_s}{\sum_{\text{All Bands}} \int_{\text{band}} \ln\left(\frac{I_0}{I}\right) dv} \quad (4-1)$$

Table 4-1. The 27 vibrational modes of pyridine from ab initio calculation, argon matrix at 10K, gas phase at 300K and solid crystal at 10K. Frequencies (ν , cm^{-1}), intensities (A, km mol^{-1}), PEDs (%), and IDs (km mol^{-1}).

MP2/6-31+G(d,p)							Ar Matrix		Gas	Cryst.
Q	ν	$\nu_{\text{calc}}^{(1)}$	A	S_i	(PED)	[ID]	ν	A	ν	ν
1	3283	3092	5.2	5a1 C3H 6a1 C4H	(64+) (30+)	[3] [3]	3094	1.1		
2	3275	3085	24.1	23b2 C3H	(92-)	[16]	3087	14.9	3086B	3079
3	3261	3072	6.5	6a1 C4H 4a1 C2H 5a1 C3H	(62+) (21-) (17-)	[5] [2] [-2]	3073 3066 3061 3058 sum =	0.8 1.4 1.3 1.7 5.2	shld ^{bl} 3067 ^{bl} 3061 ^{bl}	3053
4	3248	3059	2.1	4a1 C2H 5a1 C3H	(73-) (19+)	[2] [1]	3027	4.9		
5	3247	3059	18.4	22b2 C2H	(92+)	[19]	3039 3030 3007 sum =	7.5 2.2 5.2 14.9	3043 ^{bl} 3030 ^{bl} 3010 ^{bl}	3034 3025 3002 2990
6	1651	1601	14.1	2a1 C2C3 3a1 C3C4 8a1 C3Hb	(46-) (16+) (15+)	[2] [-2] [6]	1598 1583 sum =	7.1 13.8 20.9	1598A 1583	1598 1582
7	1642	1593	3.5	21b2 C3C4 19b2 CN 26b2 C4Hb	(52+) (20-) (13-)	[2] [2] [-2]	1578	6.0	1581B	1572
8	1527	1481	1.8	7a1 C2Hb 8a1 C3Hb 1a1 NC 3a1 C3C4	(47+) (25+) (14-) (13+)	[3] [2] [-2] [0]	1483	5.2	1483A	1483
9	1493	1448	21.2	20b2 C2C3 25b2 C3Hb 26b2 C4Hb 24b2 C2Hb	(36+) (24-) (18-) (16+)	[8] [3] [5] [3]	1440	28.7	1441B	1438
10	1412	1369	.7	19b2 CN 24b2 C2Hb 21b2 C3C4 26b2 C4Hb 20b2 C2C3	(39-) (16+) (15-) (14+) (11+)	[2] [-1] [0] [1] [-1]	1285	0.4		
11	1398	1356	.2	24b2 C2Hb 19b2 CN 25b2 C3Hb	(50+) (27+) (14+)	[0] [1] [0]	1361	0.7		1356
12	1259	1221	2.1	7a1 C2Hb 8a1 C3Hb 1a1 NC 2a1 C2C3	(40-) (24+) (22-) (13+)	[2] [-2] [2] [0]	1219	3.7	1218A	1218
13	1194	1158	1.3	25b2 C3Hb 26b2 C4Hb 21b2 C3C4	(42+) (41-) (15-)	[-1] [1] [0]	1147	5.2	1144B	1147
14	1105	1071	5.9	8a1 C3Hb 3a1 C3C4 1a1 NC 10a1 R1	(33+) (31-) (20+) (13+)	[3] [1] [3] [-1]	1073	3.0	1071A	1068

Table 4-1 -- continued

MP2/6-31+G(d,p)							Ar Matrix		Gas		Cryst.	
Q	v	$\nu_{\text{calc}}^{\text{a)}$	A	S _i	(PED)	[ID]	v	A	v		v	
15	1092	1060	.1	20b2 C2C3 25b2 C3Hb 21b2 C3C4 24b2 C2Hb 26b2 C4Hb	(47+) (13+) (12+) (11-) (10+)	[0] [0] [0] [0] [0]	1052	.1			1057	
16	1052	1021	3.7	10a1 R1 3a1 C3C4 2a1 C2C3	(50+) (29+) (16+)	[2] [1] [0]	1031	9.7	1031A		1031	
17	1013	982	5.3	10a1 R1 1a1 NC 2a1 C2C3	(35+) (35-) (19-)	[2] [4] [0]	991	5.2	991A		991	
18	939	911	.0	11a2 C2Hw 12a2 C3Hw 13a2 R3o	(100+) (12-) (-11+)	[0] [0] [0]						
19	923	896	.0	16b1 C4Hw 14b1 C2Hw 15b1 C3Hw 18b1 R2o	(75+) (23-) (10-) (-11-)	[0] [0] [0] [0]	1000	.1			997	
20	904	877	.5	14b1 C2Hw 15b1 C3Hw	(60+) (45-)	[3] [-3]						
21	873	846	.0	12a2 C3Hw	(96+)	[0]						
22	722	700	78.2	15b1 C3Hw 16b1 C4Hw 14b1 C2Hw	(41+) (29+) (29+)	[34] [21] [30]	701	61.2	700C		705	
23	664	645	.5	27b2 R3	(91+)	[1]						
24	608	590	3.3	9a1 R2	(92-)	[3]	602	4.5	601A		604	
25	599	581	9.6	17b1 R1o 15b1 C3Hw 14b1 C2Hw	(96+) (9-) (-11-)	[8] [13] [-9]	744	10.4	744C		752	
26	377	365	2.7	18b1 R2o	(105+)	[6]	405	3.7				
27	360	349	.0	13a2 R3o	(115+)	[0]						

a) Frequencies below 2000 cm^{-1} are scaled by 0.970, and by 0.942 above 2000 cm^{-1} (see text).

b) Gas phase band center uncertain due to multiple band overlaps.

Here, A_s is the calculated molar absorption and the integral is the experimental integrated intensity as defined in Chapter 2.

The potential energy distribution and the intensity distribution in terms of symmetry coordinates are given for each mode of vibration. The definition of the symmetry coordinates is given in Appendix C. From the band contours in the vapor phase spectrum, it is possible to verify the symmetry of some fundamental transitions. For asymmetric top molecules like pyridine, the dipole transitions along the A, B and C axes can be identified by the distinctive rotational envelop of a vibrational transition.⁹⁴⁻⁹⁶ In general, both type A and type C bands have pronounced central Q branches, that of type C being much stronger relative to the P and R branches. The type B band has no central Q branch, but rather a doublet Q branch that often overlaps with the P and R branches. Wong and Colson⁹⁷ have determined that transitions to levels of a_1 , b_2 and b_1 symmetry in pyridine should possess type A, B and C contours respectively. These are clearly visible in Figure 4-2 for the non-overlapped fundamentals of the gas phase spectrum. Contour types are reported in Table 4-1 when their identification is unambiguous.

The general agreement between theory and experiment is quite good although a few discrepancies are worth noticing. The calculated intensities in the C-H stretching region are overestimated with respect to the rest of the spectrum. The relative intensity pattern predicted in the 1000 cm^{-1} region for the bands at 1073 , 1032 and 991 cm^{-1} , is also incorrect. The frequencies of some of the out-of-plane motions with b_1 symmetry are not predicted correctly, especially when large contributions of the out-of-plane ring distortions (symmetry coordinates $17b_1$ R1o and $18b_1$ R2o) are involved. The worst

disagreement is seen for the mode observed at 744 cm^{-1} which is predicted by the MP2/6-31+G(d,p) calculation at 581 cm^{-1} and for the mode at 405 cm^{-1} predicted at 365 cm^{-1} (see Table 4-1). This error appears to be characteristic of calculation with this basis set made for ring molecules like pyridine. A density functional theory (DFT) calculation carried out⁷³ with a similar basis set (B3LYP/6-31G(d,p)) predicts these two modes, after scaling, at 742 cm^{-1} and 410 cm^{-1} respectively.

3. Infrared Spectra of the HBr:pyridine Complex

The experimental set-up is described in Chapter 2. Solid pyridinium bromide (from Aldrich, 98% purity) was used as a convenient source of gaseous HBr and pyridine. The salt was further purified by vacuum sublimation, primarily to remove water. At room temperature, the vapor pressure above the salt was high enough to provide sufficient concentrations of HBr and pyridine in the matrix without heating. The concentrations of HBr and pyridine were kept as low as possible to minimize absorption by higher aggregates, and the thickness of the matrix was deliberately minimized to insure uniformity of the matrix.

A typical experimental spectrum of a matrix containing Ar, HBr, and pyridine after annealing to 30K is shown in Figure 4-3. This spectrum shows absorption bands from the isolated monomers and bands from the HBr:pyridine complex. The strongest bands attributed to the complex are marked by asterisks. Interference fringes are also visible in this figure. Those with about 815 cm^{-1} spacing between maxima result from deposition on the back side (far from the inlet sample tube) of the cold window. Interference fringes from the thicker deposit on the front side (near the sample inlet) with spacing between maxima of about 23 cm^{-1} are seen in this figure only in the frequency

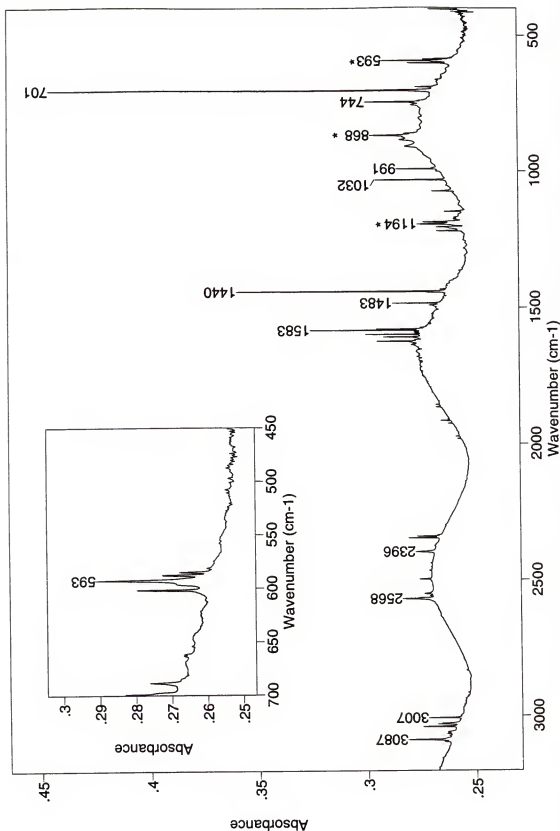


Figure 4-3. The experimental infrared spectrum of a mixture of HBr, pyridine, and Ar at 10 K after annealing at 30 K. The new bands which are marked by asterisks are attributed to the HBr:pyridine complex. The top left window shows the lower frequency region where the front window fringes are still visible.

region below 1000 cm^{-1} . The interference fringes yield a matrix thickness of $\ell = \ell_1 + \ell_2 = 4 + 154 = 158\text{ }\mu\text{m}$ (see Chapter 2), which is used to determine the absolute concentrations for HBr, pyridine and the complex. The measured integrated absorbances of the H-Br stretching bands in HBr monomer and the HBr:pyridine complex are used with the corresponding computed MP2/6-31+G(d,p) integrated molar absorption coefficients [$A(\text{HBr}) = 11\text{ km mol}^{-1}$; $A(\text{HBr:pyridine}) = 6749\text{ km mol}^{-1}$ (see Table 4-2)] to estimate the relative concentrations of these species. Under the experimental conditions, the relative concentration of [Ar:HBr:Py:complex] is about [2500:1:1:0.05]. The absolute concentrations of the species are $C(\text{HBr}) \approx C(\text{Py}) \approx 1 \times 10^{-2}\text{ mol L}^{-1}$ and $C(\text{HBr:pyridine}) \approx 2 \times 10^{-4}\text{ mol L}^{-1}$. The concentration of the H_2O impurity estimated using the experimental integrated absorbance of ν_3 and its computed MP2/6-31+G(d,p) intensity [$A(\nu_3, \text{H}_2\text{O}) = 67\text{ km mol}^{-1}$] is about two orders of magnitude lower than that of the HBr monomer. In the initial matrix, before annealing, trace bands were found in the spectrum which correspond to $(\text{HBr})_2$ and $\text{HBr:H}_2\text{O}$. The concentrations of these pairs were estimated from the integrated experimental absorbances and the computed MP2/6-31+G(d,p) intensities [$A((\text{HBr})_2) = 182\text{ km mol}^{-1}$; $A(\text{HBr:H}_2\text{O}) = 435\text{ km mol}^{-1}$] to be about three orders of magnitude lower than the concentrations of monomeric HBr and pyridine. Because the concentrations of $(\text{HBr})_2$ and $\text{HBr:H}_2\text{O}$ are so low, it is unlikely that complexes of pyridine with either of these hydrogen-bonded species form in any significant amount during the first annealing. The dominant hydrogen-bonded complex containing pyridine in the matrix before and after the first annealing is the 1:1 HBr:pyridine complex.

Figures 4-4 and 4-5 show, on an expanded scale, the baseline corrected experimental spectra of matrix-isolated pyridine, and of matrices containing both HBr and pyridine before and after annealing at about 30 K. The higher-frequency spectral region between 1700 and 3200 cm^{-1} is shown in Figure 4-4. The strong absorption bands between 3000 and 3100 cm^{-1} arise from the C-H stretching vibrations of pyridine. The middle and bottom spectra show, in addition, bands in the region from 2540 - 2580 cm^{-1} due to the H-Br stretch in the monomer. The spectrum of HBr before annealing exhibits relatively strong absorptions at 2568 and 2549 cm^{-1} due to the $J = 0 \rightarrow 1$ [R(0)] and $J = 1 \rightarrow 0$ [P(1)] vibration-rotation transitions, respectively, for the rotating HBr monomers, together with very weak bands due to trace amounts of $(\text{HBr})_2$ (2496 cm^{-1}) and of $\text{HBr}:\text{H}_2\text{O}$ (2396 cm^{-1}). The spectra of HBr monomer, its hydrogen-bonded clusters such as dimer and trimer, and its complex with H_2O in the argon matrix are well known^{98,99} and are not discussed here. It should be reemphasized that the concentrations of $(\text{HBr})_2$ and $\text{HBr}:\text{H}_2\text{O}$ in the initial matrix deposit are about three orders of magnitude lower than that of HBr itself. It is thus unlikely that higher order clusters with three hydrogen-bonded molecules form during annealing. After the first annealing the intensities of bands attributed to $(\text{HBr})_2$ and $\text{HBr}:\text{H}_2\text{O}$ increase, but the bands due to monomeric HBr still dominate the spectrum in the region from 1700 to 3200 cm^{-1} . The relative increase in the absorbance of the bands due to $(\text{HBr})_2$ and $\text{HBr}:\text{H}_2\text{O}$ after annealing results less from the higher concentrations of these species than from the relatively high molar absorption coefficients for the hydrogen-bonded Br-H stretch compared to the HBr monomer. There are no bands in this part of the spectrum, either before or after the first annealing, that can be assigned to the $\text{HBr}:\text{pyridine}$ complex.

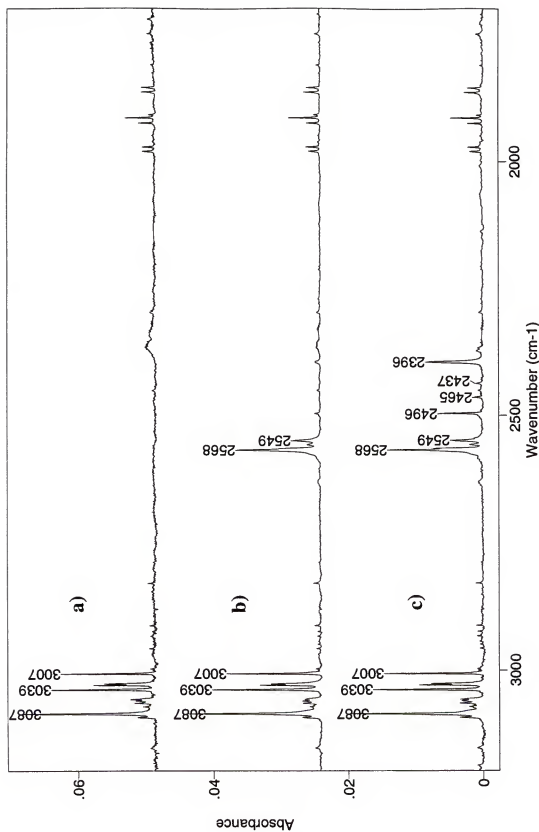


Figure 4-4. Experimental infrared matrix spectra, after correction to a horizontal baseline, in the region from 3200 to 1700 cm^{-1} for pyridine + Ar (a), and for HBr + pyridine + Ar before (b) and after (c) annealing.

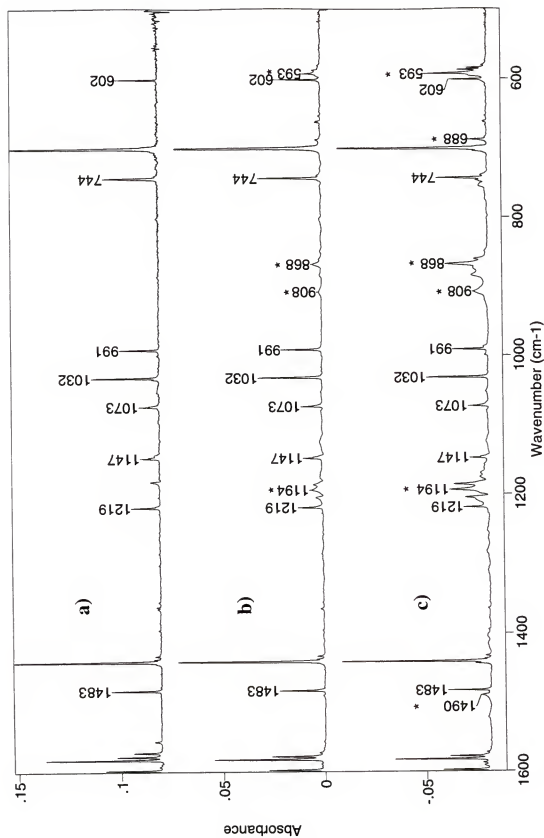


Figure 4-5. Experimental infrared spectra in the low frequency region 1600 - 500 cm^{-1} , corresponding to the spectra shown in Figure 4-4.

The lower-frequency region, from 500 to 1600 cm^{-1} , is shown in Figure 4-5 and is dominated by absorption due to the pyridine monomer. However, the spectrum of the three-component mixture (Ar, HBr, pyridine) before and after annealing does show new bands, which are identified by asterisks. After the first annealing the integrated absorbances of these bands increase by a factor of about five, and these bands are attributed to the 1:1 HBr:pyridine complex.

The spectrum of the 1:1 HBr:pyridine complex extracted from Figure 4-5 is shown on an expanded scale in Figure 4-6. There are three regions of strong absorption (around 1194, 868, and 593 cm^{-1}), each showing multiple bands, and two weaker bands (at 1490 and 688 cm^{-1}). It is interesting to notice that the majority of the 33 modes of the complex are not observed, both because they are too weak and because of the very low concentration of complex in the matrix. The existence of multiple bands in the regions of strong absorption around 1194, 868, and 593 cm^{-1} may be due to several factors. These include interaction of the complex with slightly different trapping sites in the matrix, Fermi resonance, and coupling of the proton stretching mode with low-frequency intermolecular modes of the complex to produce relatively strong combination bands.

The three regions showing the strong absorptions are all at significantly lower frequencies than the Br-H stretching of the monomer at 2568 cm^{-1} . They are also dramatically lower than the frequency of the strong band associated with the N-H stretching mode observed near 3000 cm^{-1} in the spectrum of pyridinium bromide in the crystal (or in solution¹⁰⁰⁻¹⁰²) as shown in Figure 4-7. This figure illustrates the difference between the spectra of the hydrogen bond of the 1:1 HBr:pyridine complex in the Ar matrix and its equivalent in the solid pyridinium bromide.

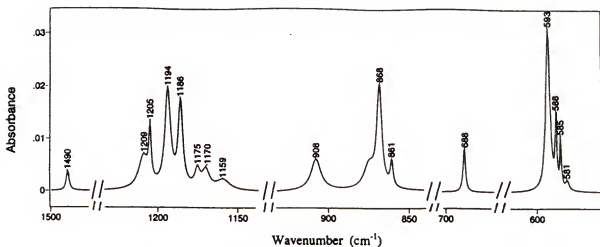


Figure 4-6. Experimental spectrum of the 1:1 HBr:pyridine complex extracted from Figure 4-5. The scale has been expanded to show the splitting of the bands in the regions near 1200, 900, and 600 cm^{-1} .

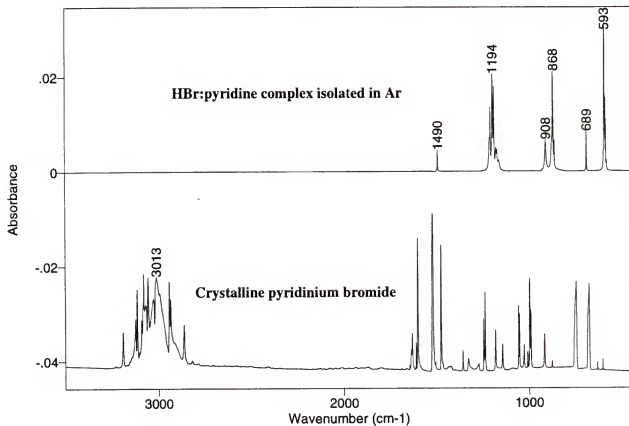


Figure 4-7. Experimental spectrum of the 1:1 HBr:pyridine complex in Ar matrix at 10 K and the experimental spectrum of crystalline pyridinium bromide at 10 K after annealing to 294 K.

4. Theoretical Ab initio Prediction

The computed structure¹⁰³ of the HBr:pyridine complex (C_{2v} symmetry) has an intermolecular Br-N distance of 2.958 Å, a Br-H distance of 1.802 Å which is significantly longer than the monomeric H-Br distance of 1.407 Å, and an N-H distance of 1.156 Å, which is also longer than the N-H distance of 1.007 Å in the pyridinium ion. These structural features are indicative of a proton-shared Br...H...N hydrogen bond in the HBr:pyridine complex.

Table 4-2 presents MP2/6-31+G(d,p) frequencies, intensities, PEDs, and IDs for the normal modes of pyridine and HBr:pyridine. The symmetry coordinates used in Table 4-2 are defined in Appendix C. The normal modes are arranged in order of decreasing frequency for pyridine. The data for pyridine and HBr:pyridine are aligned so that corresponding modes are presented in the same row in order to facilitate comparison among these three systems. Examination of Table 4-2 reveals that the frequencies of most normal modes of pyridine experience relatively minor changes upon complexation with HBr.

Examination of the PEDs and IDs shows that, except for the two a_1 modes at 1259 and 1105 cm^{-1} , all pyridine local modes below 1800 cm^{-1} with a_1 symmetry mix strongly with the local hydrogen-bonded proton stretching mode in HBr:pyridine to produce the intense bands that are so characteristic of its IR spectrum. The mixing of the local proton stretching mode with the two a_1 local modes of pyridine at 1052 and 1013 cm^{-1} is particularly complex, and gives rise to the strong band at 977 cm^{-1} in the spectrum of the complex. It is apparent that the motion of the hydrogen-bonded proton in these modes is coupled to motion of the Br and N atoms, and to motions of atoms of the pyridine moiety.

Table 4-2. Computed MP2/6-31+G(d,p) vibrational frequencies (ν , cm^{-1}), intensities (A, km mol^{-1}), PEDs (%), and IDs (km mol^{-1}) for pyridine and HBr:pyridine.

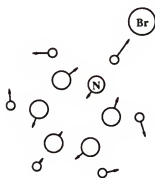
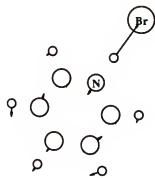
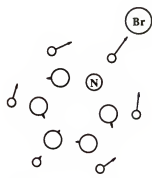
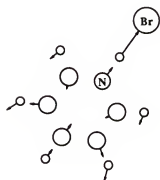
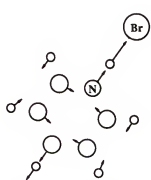
Pyridine						HBr:pyridine					
Q	ν	A	S_i	(PED)	[ID]	Q	ν	A	S_i	(PED)	[ID]
1	3283	5	5a1 C3H 6a1 C4H	(64+) (30+)	[3] [3]	1	3302	3	5a1 C3H 4a1 C2H 6a1 C4H	(67+) (21+) (12+)	[1] [3] [1]
2	3275	24	23b2 C3H	(92-)	[16]	2	3299	0	27b2 C3H 26b2 C2H	(73-) (26-)	[0] [0]
3	3261	7	6a1 C4H 4a1 C2H 5a1 C3H	(62+) (21-) (17-)	[5] [2] [-2]	3	3288	2	4a1 C2H 6a1 C4H	(72-) (19+)	[4] [-1]
4	3248	2	4a1 C2H 5a1 C3H	(73-) (19+)	[2] [1]	5	3275	2	6a1 C4H 5a1 C3H	(69-) (24+)	[1] [0]
5	3247	18	22b2 C2H	(92+)	[19]	4	3285	2	26b2 C2H 27b2 C3H	(73+) (26-)	[2] [0]
6	1651	14	2a1 C2C3 3a1 C3C4 8a1 C3Hb	(46-) (16+) (15+)	[2] [-2] [6]	6	1708	758	2a1 C2C3 1a1 NC 7a1 C2Hb 9a1 R2 12a1 NHs 11a1 HBrS	(38+) (15-) (12+) (10+) (10+) (-1+)	[-9] [100] [-54] [57] [330] [308]
7	1642	4	21b2 C3C4 19b2 CN 26b2 C4Hb	(52+) (20-) (13-)	[2] [2] [-2]	7	1671	1	25b2 C3C4 23b2 CN 32b2 NHBrb	(36+) (32-) (11-)	[0] [2] [1]
						8	1566	24	32b2 NHBrb 30b2 C4Hb 24b2 C2C3 28b2 C2Hb 25b2 C3C4	(27-) (18+) (17-) (17-) (10-)	[4] [6] [10] [8] [-1]
						9	1561	3898	12a1 NHs 3a1 C3C4 8a1 C3Hb 2a1 C2C3 11a1 HBrS	(67+) (11+) (10+) (10-) (-8+)	[1826] [15] [-71] [8] [2046]
8	1527	2	7a1 C2Hb 8a1 C3Hb 1a1 NC 3a1 C3C4	(47+) (25+) (14-) (13+)	[3] [2] [-2] [0]	10	1533	1454	7a1 C2Hb 8a1 C3Hb 12a1 NHs 11a1 HBrS	(35-) (24-) (19+) (0-)	[106] [59] [594] [780]
9	1493	21	20b2 C2C3 25b2 C3Hb 26b2 C4Hb 24b2 C2Hb	(36+) (24-) (18-) (16+)	[8] [3] [5] [3]	11	1478	10	24b2 C2C3 25b2 C3C4 23b2 CN 32b2 NHBrb 29b2 C3Hb	(37+) (22-) (20-) (10-) (10-)	[10] [1] [-4] [-2] [1]
10	1412	1	19b2 CN 24b2 C2Hb 21b2 C3C4 26b2 C4Hb 20b2 C2C3	(39-) (16+) (15-) (14+) (11+)	[2] [-1] [0] [1] [-1]	12	1414	0	29b2 C3Hb 30b2 C4Hb 28b2 C2Hb 32b2 NHBrb 23b2 CN	(27-) (26-) (22-) (12-) (11+)	[0] [0] [0] [0] [0]
11	1398	0	24b2 C2Hb 19b2 CN 25b2 C3Hb	(50+) (27+) (14+)	[0] [1] [0]	13	1339	1	28b2 C2Hb 32b2 NHBrb 23b2 CN	(42+) (34-) (26+)	[2] [-1] [1]
12	1259	2	7a1 C2Hb	(40-)	[2]	14	1241	6	7a1 C2Hb	(43+)	[5]

Table 4-2 -- continued

Pyridine						HBr:pyridine					
Q	v	A	S ₁	(PED)	[ID]	Q	v	A	S ₁	(PED)	[ID]
			8a1 C3Hb	(24+)	[-2]				8a1 C3Hb	(28-)	[-3]
			1a1 NC	(22-)	[2]				1a1 NC	(13+)	[5]
			2a1 C2C3	(13+)	[0]				2a1 C2C3	(13-)	[0]
13	1194	1	25b2 C3Hb	(42+)	[-1]	15	1205	1	29b2 C3Hb	(44+)	[-1]
			26b2 C4Hb	(41-)	[1]				30b2 C4Hb	(39-)	[1]
			21b2 C3C4	(15-)	[0]				25b2 C3C4	(14-)	[0]
14	1105	6	8a1 C3Hb	(33+)	[3]	16	1101	4	8a1 C3Hb	(28-)	[-2]
			3a1 C3C4	(31-)	[1]				1a1 NC	(26-)	[-6]
			1a1 NC	(20+)	[3]				3a1 C3C4	(20+)	[0]
			10a1 R1	(13+)	[-1]				10a1 R1	(20-)	[1]
15	1092	0	20b2 C2C3	(47+)	[0]	17	1096	1	24b2 C2C3	(44-)	[-2]
			25b2 C3Hb	(13+)	[0]				28b2 C2Hb	(13+)	[1]
			21b2 C3C4	(12+)	[0]				25b2 C3C4	(13-)	[0]
			24b2 C2Hb	(11-)	[0]				30b2 C4Hb	(10-)	[1]
			26b2 C4Hb	(10+)	[0]				29b2 C3Hb	(10-)	[0]
16	1052	4	10a1 R1	(50+)	[2]	18	1096	7	22b1 NHBrb	(94-)	[10]
			3a1 C3C4	(29+)	[1]	19	1046	6	3a1 C3C4	(48+)	[1]
			2a1 C2C3	(16+)	[0]				2a1 C2C3	(30+)	[0]
17	1013	5	10a1 R1	(35+)	[2]				1a1 NC	(12+)	[-4]
			1a1 NC	(35-)	[4]	20	977	639	10a1 R1	(66+)	[-27]
			2a1 C2C3	(19-)	[0]				1a1 NC	(16-)	[-42]
18	939	0	11a2 C2Hw	(106+)	[0]				12a1 NHs	(7-)	[249]
			12a2 C3Hw	(19-)	[0]				11a1 HBrbs	(6+)	[470]
			13a2 R3o	(-25+)	[0]	22	939	0	13a2 C2Hw	(73+)	[0]
19	923	0	16b1 C4Hw	(99+)	[0]				14a2 C3Hw	(42+)	[0]
			15b1 C3Hw	(19-)	[0]				15a2 R3o	(-15+)	[0]
			14b1 C2Hw	(16-)	[0]	21	940	1	18b1 C4Hw	(79+)	[-3]
			17b1 R1o	(-12-)	[0]				17b1 C3Hw	(16-)	[2]
			18b1 R2o	(-22-)	[0]				16b1 C2Hw	(13+)	[2]
20	904	0	15b1 C3Hw	(71+)	[-3]				20b1 R2o	(-10-)	[-1]
			14b1 C2Hw	(61-)	[2]	23	902	1	16b1 C2Hw	(60-)	[5]
			17b1 R1o	(-38+)	[-1]				17b1 C3Hw	(46-)	[-4]
21	873	0	12a2 C3Hw	(108+)	[0]	24	884	0	14a2 C3Hw	(66+)	[0]
			13a2 R3o	(-15-)	[0]				13a2 C2Hw	(34-)	[0]
22	722	78	15b1 C3Hw	(46-)	[37]	25	736	101	17b1 C3Hw	(38+)	[37]
			14b1 C2Hw	(26-)	[22]				16b1 C2Hw	(33-)	[40]
			16b1 C4Hw	(25-)	[13]				18b1 C4Hw	(28+)	[23]
23	664	0	27b2 R3	(91+)	[1]	26	653	0	31b2 R3	(92-)	[0]
24	608	3	9a1 R2	(92-)	[3]	27	614	210	9a1 R2	(80+)	[-32]
25	599	10	17b1 R1o	(132+)	[10]				11a1 HBrbs	(18+)	[183]
			15b1 C3Hw	(-9+)	[14]				12a1 NHs	(-4+)	[60]
			18b1 R2o	(-15-)	[-6]	28	539	4	19b1 R1o	(98+)	[8]
26	377	3	18b1 R2o	(136+)	[7]				16b1 C2Hw	(-10-)	[-7]
			17b1 R1o	(18+)	[-2]	29	393	0	20b1 R2o	(93+)	[2]
			15b1 C3Hw	(-27+)	[-4]				19b1 R1o	(14-)	[-1]
			16b1 C4Hw	(-28-)	[1]						

Table 4-2 -- continued

Pyridine						HBr:pyridine					
Q	v	A	S _i	(PED)	[ID]	Q	v	A	S _i	(PED)	[ID]
27	360	0	13a2 R3o 11a2 C2Hw 12a2 C3Hw	(140-) (-13-) (-27+)	[0] [0] [0]	30	379	0	15a2 R3o	(115+)	[0]
						31	212	44	11a1 HBrs 9a1 R2	(84+) (10-)	[41] [2]
						32	88	1	21b1 BrHw 20b1 R2o	(91+) (12+)	[1] [0]
						33	49	2	33b2 BrHb	(98+)	[2]

1707 cm⁻¹; 758 km/mol1561 cm⁻¹; 3898 km/mol1533 cm⁻¹; 1454 km/mol977 cm⁻¹; 639 km/mol614 cm⁻¹; 210 km/molFigure 4-8. Calculated MP2/6-31+G(d,p) atom displacements for the HBr:pyridine a₁ normal modes associated with the most intense bands in the spectrum.

It is also notable that none of the strong bands in the HBr:pyridine spectrum arise from bending vibrations of the hydrogen-bonded proton. Figure 4-8 depicts the computed displacements of atoms for the strongest bands in the spectrum and illustrates the coupling between the local modes of the pyridine moiety and the motion of the hydrogen-bonded Br, H, and N atoms.

5. Discrepancies between Computed and Experimental Spectra

The computed unscaled harmonic spectrum of HBr:pyridine is shown with the experimental spectrum in Figure 4-9. This figure illustrates graphically how the several very intense bands associated with the proton-stretching motion in the complex dominate the spectrum. The most striking feature in both spectra is the appearance of several strong bands below 1800 cm^{-1} . These bands are typical for complexes that have proton-shared hydrogen bonds.^{103,104} The strongest band at 1561 cm^{-1} in the computed HBr:pyridine spectrum is shifted to lower frequency by 43% relative to the HBr stretch for monomeric HBr, in reasonable agreement with the 54% shift observed for the strongest band (1194 cm^{-1}) in the experimental spectrum. However, the computed intensity pattern for the strong bands is quite different from that measured experimentally, as can be seen in Figure 4-9. Clearly the frequencies and the intensity distribution among the various strong bands in the computed spectrum do not match those observed in the experimental spectrum.

Two factors may be responsible for the discrepancy between the experimental and the computed spectra of HBr:pyridine. The first is that the experimental spectrum is for the complex isolated in an argon matrix, whereas the computed refers to the isolated complex in the gas phase. It has been suggested previously¹⁰⁵ that a few Ar or Ne atoms

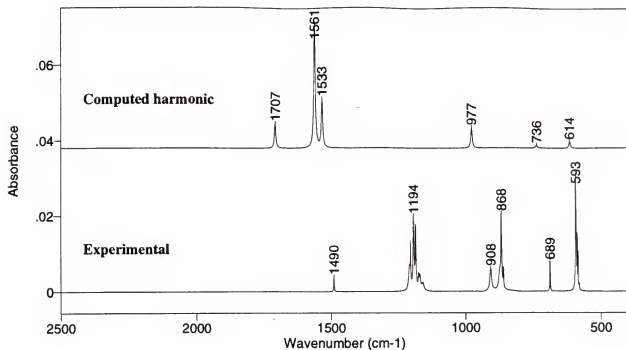


Figure 4-9. The computed MP2/6-31+G(d,p) harmonic spectrum of the HB:pyridine complex, and its experimental spectrum obtained in the Ar matrix.

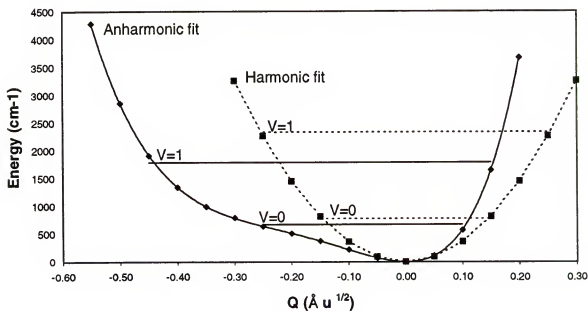


Figure 4-10. The potential energy curve for motion along the normal coordinate for the band computed at 1561 cm^{-1} . The Br-H and Br-N stretches are coupled in this mode. The solid curve is a fit to the computed points using a quartic polynomial. The dashed curve is the potential which fits the computed $v=0$ and $v=1$ harmonic vibrational levels. The corresponding anharmonic energies are also shown.

in the vicinity of the complex can change the computed structure and spectra of specific hydrogen-bonded complexes. However, the computed Br-N and Br-H distances in HBr:pyridine:2Ne differ from their values in the HBr:pyridine by only 0.003 and 0.002 Å, respectively. Since the correlation between computed structures and spectra is well established for complexes of HA:4-X-pyridine,¹⁰³ no significant spectral changes are anticipated for such small structural changes. It seems very unlikely that interaction with the Ar matrix is responsible for the discrepancy between the computed and experimental spectra.

The second factor which may be responsible for the discrepancy is related to the harmonic approximation used to calculate the vibrational spectrum. In order to evaluate the magnitude of the anharmonicity of the hydrogen-bonded proton stretching normal mode, single point MP2/6-31G(d,p) energies were computed along the vector describing the normal coordinate, Q , for the mode at 1561 cm^{-1} . A quartic polynomial [$V = aQ^4 + bQ^3 + cQ^2 + dQ + e$] was then fitted to these energies to give the curve shown in Figure 4-10, which is very anharmonic. This figure also shows the corresponding harmonic potential curve.

Following a procedure similar to that suggested by Somorjai and Hornig,¹⁰⁶ we used the fitted anharmonic potential to estimate the energy levels for the two lowest states ($v = 0$ and $v = 1$) for the proton-stretching mode Q . The anharmonic energy levels are shown in Figure 4-10, where they are contrasted with the harmonic levels. The frequency for the $v = 0 \rightarrow v = 1$ vibrational excitation obtained from the anharmonic potential is 1122 cm^{-1} , compared with 1561 cm^{-1} for the harmonic potential. The ratio of $\nu_{\text{anh}}/\nu_{\text{har}}$ is

0.72. Accordingly, the ratio of the effective force constant for the anharmonic proton stretching mode to that for the harmonic, $k_{\text{anh}}/k_{\text{har}}$, is $(0.72)^2 = 0.52$.

For the symmetry coordinates used, the effective force constant for the hydrogen-bonded proton stretching normal mode is a linear combination of three internal force constants; namely, the two diagonal HBr and NHs constants and the interaction constant between them. These three constants were multiplied by 0.52, without changing any other force constants of the complex. The entire spectrum along with the new Cartesian atomic displacements were re-computed using the Xtrapack program. This re-computed (or “anharmonic”) spectrum is compared with the original computed harmonic spectrum and the experimental spectrum in Figure 4-11. The new atomic displacements corresponding to the strongest absorptions are presented in Figure 4-12, and compared with the computed MP2/6-31+G(d,p) atomic displacements.

Since the re-computed spectrum shows one strong band in each of the three spectral regions of strong absorption, we assumed that the intensities of the multiple components observed in the vicinity of each strong band in the original experimental spectrum are derived from that single strong normal mode. Therefore, the total integrated intensity for all components in each region has been represented as a single strong band for each region, which is shown in the experimental integrated intensity sum spectrum in Figure 4-11. The computed anharmonic spectrum and the experimental spectra, particularly the integrated intensity sum spectrum, are in excellent agreement.

Table 4-3 presents the calculated frequencies, intensities, PEDS, and IDs for the nine strongest modes computed for the HBr:pyridine spectrum after the adjustment for anharmonicity described above. The experimental frequencies and intensities from the

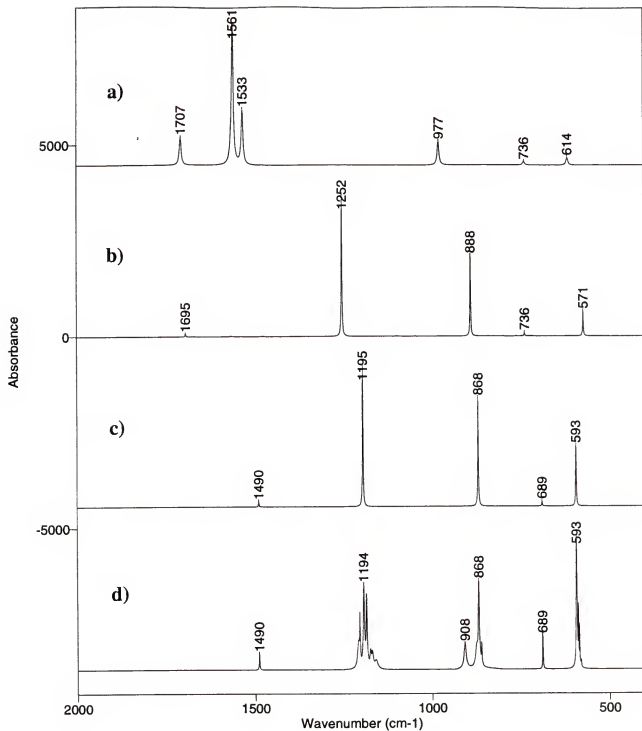
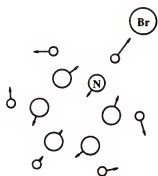
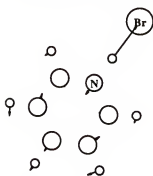


Figure 4-11. Infrared spectra for the HBr:pyridine complex: a) computed harmonic; b) computed anharmonic; c) experimental integrated intensity sum; and d) experimental extracted.

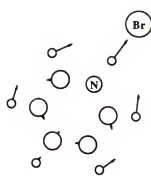
Computed harmonic



1707 cm^{-1} ; 758 km/mol

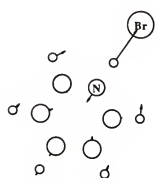


1561 cm^{-1} ; 3898 km/mol

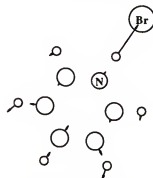


1533 cm^{-1} ; 1454 km/mol

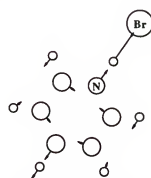
Re-computed anharmonic



1252 cm^{-1} ; 4045 km/mol



888 cm^{-1} ; 2470 km/mol



571 cm^{-1} ; 1144 km/mol

Figure 4-12. Re-computed atom displacements for HBr:pyridine a_1 normal modes associated with the most intense bands in the anharmonic spectrum. They are compared with the displacements of the three most intense bands in the harmonic spectrum.

Table 4-3. Frequencies (cm^{-1}), intensities (km mol^{-1}) PEDs (%) and IDs (km mol^{-1}) for the strongest bands in the anharmonic spectrum^a of HBr:pyridine compared with the original harmonic spectrum, and with experimental values^b.

Original calculation						Anharmonic re-computed					
Q	v	A	S _j	(PED)	[ID]	Q	v	A	S _j	(PED)	[ID]
6	1708	758	2a1 C2C3	(38+)	[-9]	6	1695	89	2a1 C2C3	(45-)	[-3]
			1a1 NC	(15-)	[100]				7a1 C2Hb	(13-)	[-19]
			7a1 C2Hb	(12+)	[-54]				1a1 NC	(12+)	[32]
			9a1 R2	(10+)	[57]				3a1 C3C4	(10+)	[-3]
			12a1 NHs	(10+)	[330]				9a1 R2	(9-)	[19]
9	1561	3898	11a1 HBrs	(-1+)	[308]				8a1 C3Hb	(9+)	[11]
									12a1 NHs	(1-)	[36]
									11a1 HBrs	(0-)	[16]
			12a1 NHs	(67+)	[1826]	8	1566 (1490)	24 104)	32b2 NHBrb	(27-)	[4]
			3a1 C3C4	(11+)	[15]				30b2 C4Hb	(18+)	[6]
10	1533	1454	8a1 C3Hb	(10+)	[-71]				24b2 C2C3	(17-)	[10]
			2a1 C2C3	(10-)	[8]				28b2 C2Hb	(17-)	[8]
			11a1 HBrs	(-8+)	[2046]				25b2 C3C4	(10-)	[-1]
			7a1 C2Hb	(35-)	[106]	13	1252 (1194)	4045 3230)	12a1 NHs	(61+)	[1854]
			8a1 C3Hb	(24-)	[59]				10a1 R1	(20+)	[39]
16	1101	4	12a1 NHs	(19+)	[594]				1a1 NC	(13-)	[123]
			11a1 HBrs	(0-)	[780]				11a1 HBrs	(-6+)	[1941]
						16	1099	15	10a1 R1	(28-)	[3]
			8a1 C3Hb	(28-)	[-2]				8a1 C3Hb	(26-)	[-4]
20	977	639	1a1 NC	(26-)	[-6]				1a1 NC	(21-)	[-10]
			3a1 C3C4	(20+)	[0]				3a1 C3C4	(20+)	[-1]
			10a1 R1	(20-)	[1]				11a1 HBrs	(0+)	[17]
									12a1 NHs	(0-)	[10]
						23	888 (868)	2141 2470)	10a1 R1	(42+)	[-37]
25	736	101	10a1 R1	(66+)	[-27]				12a1 NHs	(35-)	[920]
			1a1 NC	(16-)	[-42]				1a1 NC	(14-)	[-65]
			12a1 NHs	(7-)	[249]				11a1 HBrs	(-1-)	[1315]
			11a1 HBrs	(6+)	[470]	25	736 (688)	101 138)	17b1 C3Hw	(38+)	[37]
									16b1 C2Hw	(33-)	[40]
27	614	210	17b1 C3Hw	(38+)	[37]				18b1 C4Hw	(28+)	[23]
			16b1 C2Hw	(33-)	[40]	27	571 (593)	661 1144)	9a1 R2	(78+)	[-53]
			18b1 C4Hw	(28+)	[23]				11a1 HBrs	(10+)	[488]
			9a1 R2	(80+)	[-32]				12a1 NHs	(4-)	[238]
			11a1 HBrs	(18+)	[183]						
			12a1 NHs	(-4+)	[60]						

- a) Re-computed with the anharmonic force constant for the proton stretching coordinate, with no other changes in the computed harmonic force constants.
- b) Experimental data are given in brackets. The assignment of the experimental spectrum is based on the anharmonic computed spectrum.

integrated intensity sum spectrum are included for comparison. It is apparent from this table that the adjustment for the anharmonicity of the proton stretching mode shifts the strong bands to lower frequencies, changes the mixing of the proton stretching coordinate with a_1 local modes of pyridine, and alters the intensity pattern. Assuming that the sum of the experimental absolute intensities for the strongest bands in the spectrum is the same as the calculated sum, values of experimental absolute intensities may be obtained from the measured relative integrated intensities. These values are reported in Table 4-3 as the experimental intensities. The final agreement between the computed anharmonic and experimental integrated intensity sum spectrum shown in Figure 4-11 and in Table 4-3 is remarkable.

B. The HBr:3,5-dichloropyridine Complex

1. Introduction

In previous publications,^{103,104} the results of theoretical calculations were presented showing that by changing the substituents of the pyridine, it was possible to systematically vary the proton affinity of the nitrogen. The correlation between the proton affinity and the relative changes in the hydrogen halide force constant and distance, $\delta k/k_0$ and $\delta r/r_0$, was of particular importance. When the hydrogen bond approaches the proton-shared region, a small change in the proton affinity has a dramatic effect on the position of the proton and on $\delta k/k_0$. These results suggest that, in this critical region, the difference of environment between the complex in gas phase and the complex "isolated" in matrix for instance, might produce significant changes. In a recent communication¹⁰⁵ we have reported ab initio calculations at the MP2/6-31+G(d,p) level

of theory of the hydrogen bonded complexes HBr:3,5-dichloropyridine (HBr:3,5-DCP) and HBr:3,5-DCP:2Ne in an attempt to account for the effect of the environment. The results were spectacular and exhibited dramatic structural and vibrational changes. The inclusion of two rare gas atoms in the calculation shifted to lower frequency the most intense band of the complex, associated with the proton stretch local oscillator, by 1134 cm^{-1} . However, it was also clear that the computed frequencies and intensities for the complex including the Ne atoms were not in very good agreement with our preliminary experimental results for the complex in an Ar matrix.

2. Infrared Spectra of the 3,5-DCP

The experimental spectra of 3,5-DCP obtained in an argon matrix, in the gas phase and in the crystal phase are presented in Figures 4-13 and 4-14 together with the scaled ab initio MP2/6-31+G(d,p) infrared spectrum. Details of the experiments were given in Chapter 2 and in Section A-1 of this chapter. Note that vapor pressure of 3,5-DCP, which is a solid at room temperature, was high enough ($>1\text{ torr}$) to provide a low noise gas phase spectrum with only 64 scans.

Examination of Figure 4-13 reveals a much simpler spectrum in the C-H stretching region than was observed for pyridine. Some of the combination and overtone bands visible in the matrix spectrum are especially prominent in the spectrum of the crystal and a tentative assignment is given in the next section. The relatively strong combination-tones in the $1700 - 2200\text{ cm}^{-1}$ region experience a red shift compared to their equivalent in the pyridine spectrum.

Observation of Figure 4-14 shows that, as for monomeric pyridine, the matrix and gas phase spectra are in very close agreement. With frequency shifts never exceeding 4

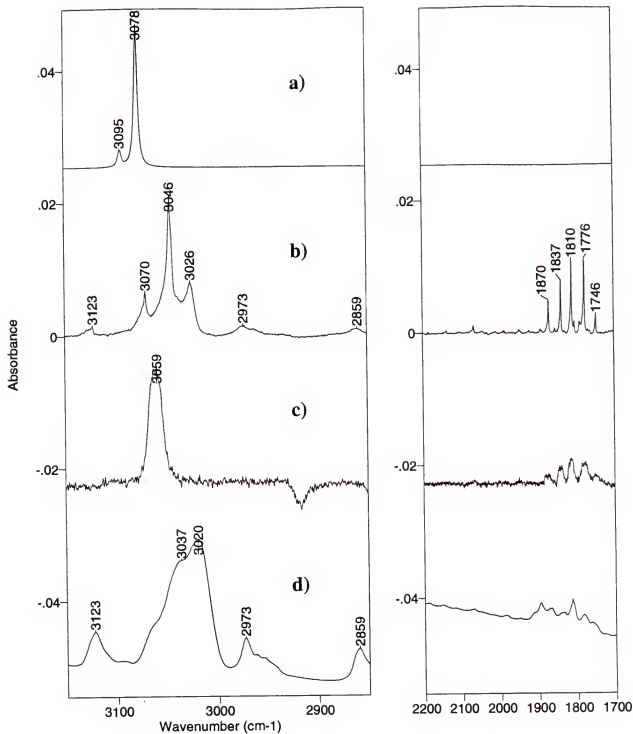


Figure 4-13. Infrared spectra of 3,5-dichloropyridine in the region from 3150 to 2850 cm^{-1} . The region from 2200 to 1700 cm^{-1} shows some strong overtones and combinations. a) Computed MP2/6-31+G(d,p). b) Isolated in an argon matrix at 10 K (baseline corrected). c) Gas phase at 300 K. d) Solid phase at 10 K.

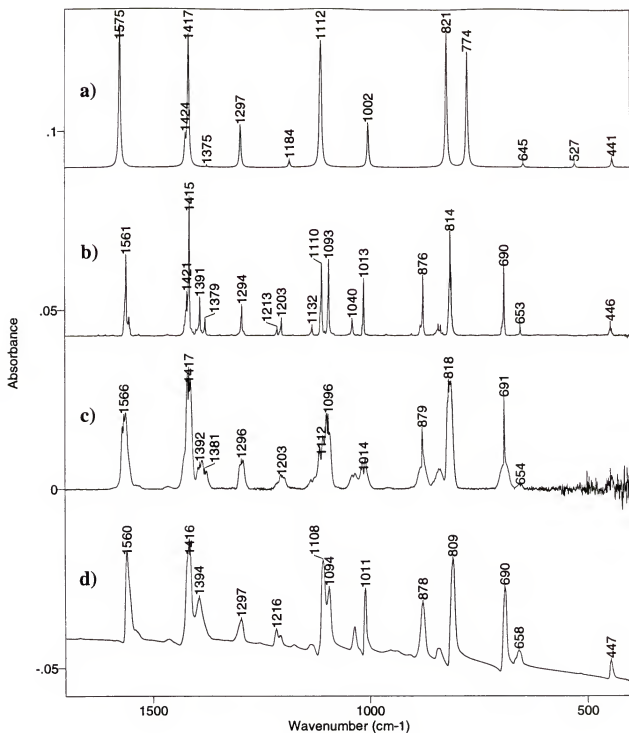


Figure 4-14. Infrared spectra of 3,5-dichloropyridine in the region from 1700 to 400 cm^{-1} . a) Computed MP2/6-31+G(d,p). b) Isolated in an argon matrix at 10 K (baseline corrected). c) Gas phase at 300 K. d) Solid phase at 10 K.

cm^{-1} (average frequency difference is 1.7 cm^{-1}), there is again no significant environmental effect. The spectra of the solid and gas phase are also close (maximum difference of 9 cm^{-1}), showing that the intermolecular interactions in the solid phase do not change substantially the frequencies of 3,5-DCP. The asymmetric shape of the bands in the solid spectrum, particularly pronounced for the absorption at 809 cm^{-1} , is typical of infrared dispersion effects by crystal lattices.

3. Vibrational Analysis of 3,5-DCP

The 3,5-DCP has C_{2v} symmetry with 27 fundamental vibrations, including three a_2 IR-inactive vibrations. Table 4-4 gives the proposed assignment for the matrix, gas phase and crystal frequencies with the MP2/6-31+G(d,p) calculation. Assignments of the experimental absorptions solely based on the ab initio results agree reasonably well with the symmetry assignments of Tanaka *et al.*,¹⁰⁷ using transferred force constants with a Urey-Bradley force field. Serious differences exist, however, compared with previous studies.^{108,109} For the calculated modes exhibiting obvious discrepancies with the experiment, such as the out-of-plane b_1 vibrations Q_{17} and Q_{19} at 774 cm^{-1} and 527 cm^{-1} , infrared and Raman studies and rotational band contours were quite helpful in determining the final assignment. Transitions with a_1 , b_1 and b_2 symmetry are expected to exhibit contours B, C and A respectively,¹⁰⁷ different than those of pyridine. Hence, the only two contour C bands observed at 876 and 690 cm^{-1} in Ar matrix, were directly assigned to Q_{17} (calculated at 774 cm^{-1}) and Q_{19} (calculated at 527 cm^{-1}).

Examination of Table 4-4 and Figure 4-13 reveals that, unlike most MP2/6-31+G(d,p) predictions, the calculated intensities of the C-H stretching region are too low relative to the rest of the spectrum. The band at 3026 cm^{-1} (Figure 4-13b) is not

Table 4-4. The 27 vibrational modes of 3,5-dichloropyridine from MP2/6-31+G(d,p) calculation, argon matrix at 10K, gas phase at 300K and solid crystal at 10K. Frequencies (ν , cm^{-1}), intensities (A, km mol^{-1}), PEDs (%), and IDs (km mol^{-1}).

MP2/6.31+G(d,p)							Ar Matrix		Gas	Cryst.
Q	v	$\nu_{\text{calc}}^{\text{a)}$	A	S_{vib}	(PED)	(ID)	v	A	v	v
1	3285	3095	.7	6a1 C4H	(99-)	[1]	3070	2.3		shld
2	3270	3081	.0	4a1 C2H	(99+)	[0]				
3	3268	3078	6.1	22b2 C2H	(100-)	[5]	3046	10.0	3059A	3038
4	1623	1575	67.9	21b2 C3C4 19b2 CN 26b2 C4Hb 27b2 R3 23b2 C3C1	(53+) (20-) (12-) (8+) (1-)	[19] [-7] [13] [10] [27]	1561	49.4	1564A	1560
5	1607	1559	.5	2a1 C2C3 3a1 C3C4 7a1 C2Hb 1a1 NC	(51+) (14-) (14+) (11-)	[0] [0] [1] [-1]	1554	2.4	1554	shld
6	1468	1424	10.5	7a1 C2Hb 3a1 C3C4	(50+) (32+)	[8] [3]	1421	6.2	shld	shld
7	1461	1417	59.5	24b2 C2Hb 20b2 C2C3 19b2 CN 26b2 C4Hb 23b2 C3C1	(35-) (28-) (20-) (12+) (2+)	[4] [29] [5] [9] [20]	1415	58.0	1417A	1416
8	1417	1375	.4	19b2 CN 20b2 C2C3 21b2 C3C4	(53+) (22-) (20+)	[-1] [2] [-1]	1391 1379 sum =	7.7 3.3 11.0	1392A 1381A	1394 shld
9	1337	1297	18.4	24b2 C2Hb 26b2 C4Hb 20b2 C2C3	(49-) (35-) (12+)	[-2] [8] [9]	shld 1294	16.3	1296A	1297
10	1221	1184	2.9	7a1 C2Hb 1a1 NC 3a1 C3C4 5a1 C3C1 2a1 C2C3 10a1 R1	(33+) (18+) (17-) (11+) (10-) (10+)	[-3] [-1] [1] [4] [0] [2]	1132	4.1	1132B	1135
11	1147	1113	39.0	26b2 C4Hb 20b2 C2C3 21b2 C3C4 23b2 C3C1	(38-) (28-) (16-) (9+)	[-10] [17] [5] [28]	1094	32.1	1096A	1094
12	1145	1111	33.5	1a1 NC 5a1 C3C1	(57-) (21+)	[7] [17]	1110	33.6	1112B	1108
13	1033	1002	19.7	10a1 R1 3a1 C3C4	(76-) (11-)	[14] [-1]	1013	20.1	1014B	1011
14	907	880	.0	11a2 C2Hw	(108+)	[0]				935 ^{bl}
15	879	853	.1	14b1 C2Hw 16b1 C4Hw	(58+) (51-)	[2] [-1]				
16	847	821	61.4	23b2 C3C1 27b2 R3	(50+) (35-)	[57] [9]	814 812	69.1	818A 815	809

Table 4-4 -- continued

MP2/6.31+G(d,p)								Ar Matrix		Gas	Cryst.
Q	v	$\nu_{\text{ref}}^{\text{a)}$	A	S _i	(PED)	[ID]		v	A	v	v
17	798	774	51.1	16b1 C4Hw 14b1 C2Hw	(54-) (50-)	[25] [27]		876	26.4	880C	878
18	665	645	1.8	9a1 R2 2a1 C2C3 5a1 C3C1	(60+) (16-) (15-)	[3] [0] [-2]		653	2.9	654B	658
19	543	527	1.8	17b1 R1o 18b1 R2o	(80-) (30+)	[11] [0]		690	27.3	691C	690
20	455	442	3.9	27b2 R3 23b2 C3C1	(57+) (34+)	[-1] [5]		441	5.8		447
21	447	433	.0	12a2 C3Clw 13a2 R3o	(71+) (34+)	[0] [0]					512 ^{bl}
22	403	391	3.3	5a1 C3C1 9a1 R2	(49+) (30+)	[3] [1]					393 ^{bl}
23	363	352	.2	25b2 C3Clb	(90+)	[0]					360 ^{bl}
24	298	290	.0	18b1 R2o 17b1 R1o 15b1 C3Clw 16b1 C4Hw	(65-) (29-) (15+) (-10+)	[0] [0] [0] [0]					
25	197	191	.4	8a1 C3Clb	(87+)	[0]					
26	185	180	.0	13a2 R3o 12a2 C3Clw	(74+) (29-)	[0] [0]					209 ^{bl}
27	156	151	.3	15b1 C3Clw 18b1 R2o	(90+) (14+)	[0] [0]					

a) Frequencies below 2000 cm⁻¹ scaled by 0.970, and by 0.942 above 2000 cm⁻¹.

b) Raman data from reference (107).

seen in spectra of matrices with lower concentrations and is attributed to higher aggregates of 3,5-DCP. Overtones and combinations appearing in the matrix spectrum between 2850 and 3150 cm^{-1} , and clearly visible in the solid, are unambiguously assigned as follows: 3123: 1561×2 (A_1); 2973: $1561 + 1415$ (A_1); 2859: $1561 + 1285$ (A_1). In the 1700 - 2200 cm^{-1} region, combination-tones involve several IR-inactive a_2 vibrations (reported in Table 4-4) with strong IR-active fundamentals. Their proposed assignment is: 1870: 935×2 (A_1); 1837: $1013 + 814$ (B_2); 1810: $935 + 879$ (B_2); 1776: $1415 + 360$ (A_1); 1746: $935 + 814$ (B_1).

The lower frequency region (Figure 4-14) is also complicated by combination bands and Fermi resonances with some fundamentals. Some ambiguity still exists for the region around 1390 cm^{-1} . From the gas phase spectrum, absorption bands at 1391 and 1379 cm^{-1} both have b_2 symmetry and can therefore couple or enter in resonance with the very strong mode Q_7 at 1415 cm^{-1} with b_2 symmetry. These two bands were unfortunately not reported by Tanaka,¹⁰⁷ and both were assigned by Green *et al.*¹⁰⁸ as overtone or combinations. We believe, however, that one of them (1391 cm^{-1}) is the weak fundamental calculated at 1375 cm^{-1} . The other (1379 cm^{-1}) was found to be polarized in the Raman spectra,¹⁰⁸ thus with a_1 symmetry, contradicting our identification from the gas phase band contour. It is consistent with an assignment as the overtone 691×2 (A_1).

The a_1 band observed at 1133 cm^{-1} is assigned to the mode Q_{10} (1184 cm^{-1}) because of its appropriate symmetry. The bands at 1203 and 1213 cm^{-1} that are closer to Q_{10} apparently have b_2 symmetries and one could arise from $512 + 690$ (B_2). There are no b_2 transitions calculated in this region that are not already assigned.

One important feature not visible in the simulated spectrum is the splitting of the band shown in the calculated spectrum at 1112 cm^{-1} (Figure 4-14a). Table 4-4 actually shows two fundamentals Q_{11} at 1111 cm^{-1} and Q_{12} at 1113 cm^{-1} with about equal intensities. This 2 cm^{-1} splitting is not resolved considering the chosen bandwidth and is quite smaller than the 17 cm^{-1} splitting of the vibrations at 1110 and 1093 cm^{-1} in the matrix spectrum. Ab initio results place the b_2 Q_{11} vibration at higher frequency than the a_1 Q_{12} . The gas phase envelopes, however, clearly indicate B contour (a_1) for the absorption at 1094 cm^{-1} and A contour (b_2) for that at 1110 cm^{-1} .

4. Infrared Spectra of the HBr:3,5-DCP Complex

The vapor source for the two components of the complex was provided by the sublimation of solid 3,5-dichloropyridinium bromide. This salt was prepared by dissolving 3,5-DCP solid (from Aldrich, 98% purity) in concentrated hydrobromic acid (48%) in equimolecular quantities at 50°C . The mixture was then evaporated to dryness in vacuum, and purification of the resulting residue by vacuum sublimation (10 torr) gave a colorless salt. There was no Chemical Abstract Service (CAS) registry number found for this salt. Its relatively high vapor pressure required the insertion of a Teflon needle valve for experiments where lower concentration was desired (see Chapter 2).

The baseline corrected spectra of a mixture of argon, HBr and 3,5-DCP before and after annealing (30 K) are presented in Figure 4-15 for the lower-frequency region ($400 - 1600\text{ cm}^{-1}$). They are compared with the spectrum of the 3,5-DCP monomer after annealing. The interference fringes (not shown) of the three component mixture yield a matrix thickness of $\ell = \ell_1 + \ell_2 = 82 + 2 = 84\text{ }\mu\text{m}$. This pathlength was used to determine the absolute concentrations of the HBr and 3,5-DCP monomers as well as those of

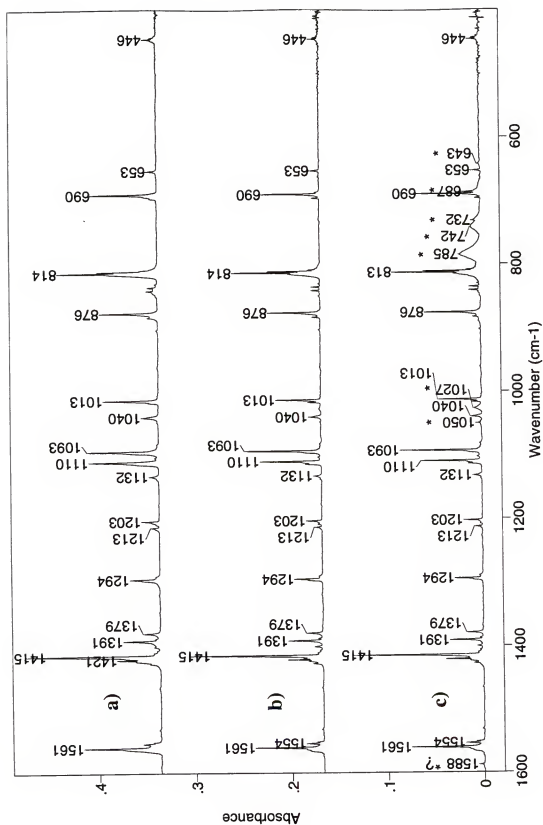


Figure 4-15. Experimental infrared matrix spectra, after baseline correction, in the region from 1600 to 400 cm⁻¹ for 3,5-DCP + Ar (a), and for HBr + 3,5-DCP + Ar before (b) and after (c) annealing.

impurities and associations such as H_2O , $(\text{HBr}:\text{H}_2\text{O})$ and $(\text{HBr})_2$. The computed MP2/6-31+G(d,p) integrated molar absorption coefficient for 3,5-DCP [$A(\text{Q}_{14}, 3,5\text{-DCP}) = 61 \text{ km mol}^{-1}$] and those given in Section A-3 of this chapter were also used. The absolute concentrations for the monomers of interest are $C(\text{HBr}) \approx 2 \times 10^{-2} \text{ mol L}^{-1}$ and $C(3,5\text{-DCP}) \approx 2 \times 10^{-2} \text{ mol L}^{-1}$. The absolute concentrations for the unwanted species are $C(\text{HBr})_2 \approx 7 \times 10^{-5} \text{ mol L}^{-1}$, $C(\text{H}_2\text{O}) \approx 3 \times 10^{-4} \text{ mol L}^{-1}$ and $C(\text{HBr}:\text{H}_2\text{O}) \approx 1 \times 10^{-5} \text{ mol L}^{-1}$. The absolute concentration of the complex was estimated to be $C(\text{BrH}:3,5\text{-DCP}) = 3 \times 10^{-4} \text{ mol L}^{-1}$ from the computed intensity [$A(\text{BrH}:3,5\text{-DCP}) = 4609 \text{ km mol}^{-1}$]. The latter was found by summing the most intense bands of the complex with absorption coefficients greater than 50 km mol^{-1} and with the H-Br stretch coordinate contributing more than 10% to the intensity of these bands (see later Table 4-6). Using the density of argon, the relative concentration of $[\text{Ar}:\text{HBr}:3,5\text{-Cl}_2\text{Py}:(\text{HBr}:3,5\text{-Cl}_2\text{Py})]$ is about [2000:1:1:0.01]. These results show that the concentrations of HBr and 3,5-DCP are about two to three orders of magnitude higher than the other species present in the matrix, so that the 1:1 BrH:3,5-Cl₂Py complex is likely to be the dominant hydrogen-bonded complex in the matrix after annealing.

The best experimental proof that the complex of BrH:3,5-DCP isolated in matrix is not a traditional hydrogen-bonded complex ($\text{X}-\text{H}\cdots\text{N}$) nor a fully ionic complex ($\text{X}^-\cdots^+\text{H}-\text{N}$) is the absence of absorption due to the complex above 1700 cm^{-1} . This higher frequency region presents only C-H stretch vibrations identical to the monomer, and absorptions of the HBr monomer similar to those shown in Figure 4-4 and briefly explained for the HBr:pyridine complex. Because there were no absorption bands of the complex, this frequency region is not shown here.

The lower frequency region, Figure 4-15, shows predominantly absorptions from the 3,5-DCP monomer. The annealed matrix of the mixture HBr/3,5-Cl₂Py/Ar shows new bands due to the 1:1 HBr:3,5-DCP complex and marked by asterisks. There are two dominant absorptions due to the complex at 784 and 741 cm⁻¹. Again, it is interesting to compare these values with the strongest absorption of the solid 3,5-dichloropyridinium bromide arising from the ⁺H-N vibration and centered at 2405 cm⁻¹ with a very broad width extending from 2100 to 2800 cm⁻¹.

The weak absorption at 1588 cm⁻¹ in Figure 4-15c is labeled with an asterisk (to indicate that it may be due to this complex) and a question mark (because it is in a region very close to the water bending vibration and could arise from the H₂O:3,5-Cl₂Py complex). The attribution to the HBr:3,5-DCP complex is made with some uncertainty.

5. Theoretical Prediction and Comparison

The optimized geometries of the HBr:3,5-DCP and HBr:3,5-DCP:2Ne complexes have been calculated at the MP2/6-31+G(d,p) level of theory in reference (105). Comparison with interatomic distances for HBr:Pyridine calculated at the same level help us to better understand the type of hydrogen bond involved in these complexes (Table 4-5). The fact that all three strong absorptions listed in Table 4-5 are predicted to be below 1700 cm⁻¹ indicates that these complexes have a proton-shared hydrogen bond type. The large N-Br intermolecular distance and the moderate increase in length $\Delta(\text{H-Br})$ in the HBr:3,5-DCP complex indicates that the hydrogen-bonded proton is not yet transferred.

Table 4-5. Computed MP2/6-31 +G(d,p) distances for HBr:Pyridine, HBr:3,5-DCP and HBr:3,5-DCP:2Ne. $\Delta(\text{H-Br})$ is the increase in length from monomeric H-Br. $\nu_{(\text{Br}\cdots\text{H}\cdots\text{N})}$ is the frequency of the strongest calculated absorption band.

	HBr:Pyridine ^a	HBr:3,5-DCP ^b	HBr:3,5-DCP:2Ne ^b
N-Br (Å)	2.958	3.094	2.936
H-Br (Å)	1.802	1.489	1.684
$\Delta(\text{H-Br})$ (Å)	0.395	0.082	0.277
$\nu_{(\text{Br}\cdots\text{H}\cdots\text{N})}$ (cm ⁻¹)	1561	1655	521

a) From reference (110).

b) From reference (105)

The frequencies, intensities, PEDs, IDs for the 33 modes of HBr:3,5-DCP and 39 modes of HBr:3,5-DCP:2Ne complexes are presented in Table 4-6. The PEDs for the mode Q_4 of the HBr:3,5-DCP complex at 1655 cm⁻¹ (Table 4-6) confirm that this mode has a predominant H-Br contribution. The HBr:pyridine complex, with a strong absorption calculated in the same frequency region, has much shorter N-Br and longer H-Br distances, suggesting that the hydrogen bond is rather ionic (consistent with the PEDs for that complex showing a 67% “NHs” contribution in Table 4-2). The HBr:3,5-DCP:2Ne complex has the shortest N-Br distance but a longer N-H distance than calculated for HBr:pyridine. The very low absorption frequency calculated for this complex suggests that it may be a “quasi-symmetric” hydrogen bond.

Examination of the bands in the C-H stretching region listed in Table 4-6 reveals that the mode Q_3 (b_2 symmetry), which was calculated to be the most intense in the monomer (Table 4-4), has zero intensity in the complex. The two a_1 symmetry modes,

Table 4-6. Computed MP2/6-31+G(d,p) frequencies (ν , cm^{-1}), intensities (A, km mol^{-1}), PEDs (%), and IDs (km mol^{-1}) for HBr:3,5-DCP and HBr: 3,5-DCP:2Ne.

HBr:3,5-DCP						HBr:3,5-DCP:2Ne					
Q	ν	A	S_i	(PED)	[ID]	Q	ν	A	S_i	(PED)	[ID]
1	3285	2	6a1 C4H	(99-)	[2]	1	3286	9	6a1 C4H 4a1 C2H	(85-) (14+)	[6] [5]
2	3274	4	4a1 C2H	(99+)	[5]	2	3285	8	4a1 C2H 6a1 C4H	(85+) (14+)	[12] [-2]
3	3271	0	26b2 C2H	(100-)	[0]	3	3283	4	26b2 C2H	(100-)	[5]
4	1655	3994	11a1 HBrs 12a1 NHs	(117+) (-26+)	[2238] [1725]						
5	1626	84	25b2 C3C4 23b2 CN 30b2 C4Hb 27b2 C3Cl	(51-) (23+) (11+) (1+)	[27] [-13] [14] [29]	5	1638	81	25b2 C3C4 23b2 CN 30b2 C4Hb 33b2 BrHb 27b2 C3Cl	(43+) (33-) (8-) (1-) (1-)	[30] [-20] [12] [19] [25]
6	1622	339	2a1 C2C3 7a1 C2Hb 3a1 C3C4 1a1 NC 11a1 HBrs 12a1 NHs	(48+) (13+) (11-) (11-) (9-) (-2-)	[-21] [-32] [9] [34] [184] [176]	4	1649	4	2a1 C2C3 7a1 C2Hb 1a1 NC	(47-) (18-) (16+)	[-4] [-5] [6]
7	1473	74	28b2 C2Hb 24b2 C2C3 23b2 CN 30b2 C4Hb 27b2 C3Cl 33b2 BrHb	(30-) (28-) (22-) (14+) (2+) (1-)	[10] [41] [9] [12] [25] [-15]	6	1516	92	23b2 CN 28b2 C2Hb 32b2 NHBrb 30b2 C4Hb 24b2 C2C3 25b2 C3C4 33b2 BrHb 27b2 C3Cl	(20+) (19+) (16+) (16-) (15+) (6+) (4+) (2-)	[14] [12] [5] [15] [41] [12] [-31] [30]
8	1462	71	7a1 C2Hb 3a1 C3C4 1a1 NC 11a1 HBrs 5a1 C3Cl 12a1 NHs	(44-) (35-) (8+) (3+) (2+) (-1+)	[-22] [-7] [11] [47] [-11] [49]	8	1464	19	7a1 C2Hb 3a1 C3C4 11a1 HBrs	(39-) (37-) (0-)	[13] [3] [10]
9	1442	2	23b2 CN 24b2 C2C3 25b2 C3C4	(47-) (26+) (22-)	[-3] [8] [-3]	7	1465	16	24b2 C2C3 23b2 CN 25b2 C3C4	(42+) (25-) (25-)	[34] [-8] [-11]
10	1335	11	28b2 C2Hb 30b2 C4Hb 24b2 C2C3	(53+) (34+) (10-)	[-5] [7] [8]	9	1329	7	28b2 C2Hb 30b2 C4Hb	(41-) (41-)	[-5] [6]
						10	1288	0	32b2 NHBrb 28b2 C2Hb 23b2 CN	(67-) (21+) (13+)	[0] [0] [0]
11	1217	8	7a1 C2Hb 3a1 C3C4 10a1 R1 5a1 C3Cl 2a1 C2C3 1a1 NC	(31+) (16-) (16+) (14+) (11-) (11+)	[-5] [1] [4] [9] [1] [-3]	11	1212	35	5a1 C3Cl 7a1 C2Hb 10a1 R1 3a1 C3C4 2a1 C2C3 12a1 NHs	(23-) (22-) (21-) (18+) (15+) (0-)	[25] [-10] [10] [3] [5] [10]
12	1154	36	30b2 C4Hb 24b2 C2C3 25b2 C3C4	(38+) (26+) (16+)	[-10] [21] [6]	13	1148	36	30b2 C4Hb 24b2 C2C3 25b2 C3C4	(34+) (26+) (15+)	[-10] [25] [7]

Table 4-6 -- continued

HBr:3,5-DCP						HBr:3,5-DCP:2Ne					
Q	v	A	S _i	(PED)	[ID]	Q	v	A	S _i	(PED)	[ID]
			27b2 C3C1	(9-)	[26]				27b2 C3C1	(11-)	[28]
13	1153	222	1a1 NC	(62+)	[36]	12	1177	475	1a1 NC	(63-)	[73]
			5a1 C3C1	(18-)	[49]				7a1 C2Hb	(18-)	[31]
			12a1 NHs	(0-)	[81]				5a1 C3C1	(7-)	[48]
			11a1 HBrs	(0+)	[31]				12a1 NHs	(6+)	[209]
									11a1 HBrs	(-2+)	[91]
14	1034	1	10a1 R1	(67-)	[2]	15	1063	759	10a1 R1	(58-)	[57]
			3a1 C3C4	(18-)	[0]				3a1 C3C4	(19-)	[-8]
			2a1 C2C3	(11-)	[0]				12a1 NHs	(8-)	[383]
									11a1 HBrs	(1+)	[342]
15	902	5	32b2 NHBrb	(80-)	[-4]	16	892	0	13a2 C2Hw	(108+)	[0]
			27b2 C3C1	(11-)	[8]	17	883	1	18b1 C4Hw	(59-)	[-3]
16	898	0	13a2 C2Hw	(108+)	[0]				16b1 C2Hw	(47-)	[4]
17	885	0	18b1 C4Hw	(55-)	[0]	18	852	62	27b2 C3C1	(51-)	[55]
			16b1 C2Hw	(53-)	[0]				31b2 R3	(32-)	[2]
18	841	61	27b2 C3C1	(41-)	[50]				25b2 C3C4	(10-)	[-5]
			31b2 R3	(29-)	[5]				33b2 Brf1b	(0+)	[12]
			32b2 NHBrb	(17+)	[7]	20	794	62	16b1 C2Hw	(58-)	[38]
19	796	53	16b1 C2Hw	(55-)	[31]				18b1 C4Hw	(46+)	[26]
			18b1 C4Hw	(48+)	[25]	14	1072	8	22b1 NHBrb	(95-)	[10]
20	740	13	22b1 NHBrb	(97+)	[12]	19	816	2052	12a1 NHs	(37-)	[1119]
21	702	44	9a1 R2	(56-)	[8]				9a1 R2	(36-)	[56]
			5a1 C3C1	(16+)	[-12]				2a1 C2C3	(16+)	[22]
			2a1 C2C3	(15+)	[1]				5a1 C3C1	(15+)	[-90]
			12a1 NHs	(7-)	[41]				11a1 HBrs	(-8-)	[964]
22	519	0	19b1 R1o	(66-)	[1]	21	521	4974	11a1 HBrs	(163-)	[2883]
			20b1 R2o	(39-)	[0]				12a1 NHs	(-78-)	[2136]
23	454	4	31b2 R3	(58+)	[-1]	22	497	0	19b1 R1o	(66+)	[-2]
			27b2 C3C1	(33-)	[5]				20b1 R2o	(42+)	[0]
24	417	0	14a2 C3C1w	(66+)	[0]	23	453	4	31b2 R3	(60+)	[0]
			15a2 R3o	(39-)	[0]				27b2 C3C1	(32-)	[5]
25	406	1	5a1 C3C1	(48+)	[2]	25	405	0	14a2 C3C1w	(70+)	[0]
			9a1 R2	(30+)	[0]				15a2 R3o	(34-)	[0]
26	365	0	29b2 C3C1b	(90-)	[-1]	24	408	28	5a1 C3C1	(44+)	[-8]
27	272	0	19b1 R1o	(58+)	[3]				9a1 R2	(34+)	[-4]
			20b1 R2o	(35-)	[0]				11a1 HBrs	(1+)	[21]
			17b1 C3C1w	(13+)	[-1]				12a1 NHs	(0+)	[18]
						26	368	0	29b2 C3C1b	(90-)	[-1]
						27	260	0	19b1 R1o	(53+)	[3]
									20b1 R2o	(35-)	[0]
									17b1 C3C1w	(19+)	[-2]
						28	225	96	12a1 NHs	(57+)	[66]
									8a1 C3C1b	(44-)	[-3]
									9a1 R2	(12-)	[-3]
									11a1 HBrs	(-27+)	[37]

Table 4-6 -- continued

HBr:3,5-DCP						HBr:3,5-DCP:2Ne					
Q	v	A	S _i	(PED)	[ID]	Q	v	A	S _i	(PED)	[ID]
28	199	6	8a1 C3Clb	(84-)	[-1]	31	155	51	12a1 NHs 8a1 C3Clb 11a1 HBrs	(71-) (42-) (-29-)	[35] [2] [17]
29	189	0	15a2 R3o 14a2 C3Clw	(69+) (33+)	[0] [0]	29	201	0	15a2 R3o 14a2 C3Clw	(66+) (29+)	[0] [0]
30	162	0	17b1 C3Clw 20b1 R2o	(64-) (28-)	[0] [0]	30	162	0	17b1 C3Clw 20b1 R2o	(62+) (29+)	[0] [0]
31	68	42	12a1 NHs 11a1 HBrs	(119+) (-29+)	[33] [10]						
32	64	1	21b1 BrHw 17b1 C3Clw 19b1 R1o	(86-) (28+) (-22-)	[0] [0] [0]	32	94	3	37b1 NeNs 21b1 BrHw 17b1 C3Clw	(58+) (41+) (14-)	[0] [3] [1]
33	23	1	33b2 BrHb	(99+)	[1]	35	30	3	33b2 BrHb 39b2 NeNCb	(87+) (11+)	[3] [0]
						33	56	0	34a1 NeNs	(100-)	[0]
						34	51	1	21b1 BrHw 37b1 NeNs	(59-) (41+)	[1] [0]
						36	22	0	35a1 NeNCb	(100+)	[0]
						37	20	0	36a2 NeNCo	(92+)	[0]
						38	17	0	39b2 NeNCb 33b2 BrHb	(89+) (11-)	[0] [0]
						39	12	0	38b1 NeNCb 21b1 BrHw	(118+) (-19+)	[0] [0]

on the other hand, have gained considerable intensity, even though no direct contribution from the “NHs” or “HBr” symmetry coordinates is present.

Comparison of Tables 4-4 and 4-6 indicate that the frequencies of most of the normal vibrations are not significantly changed upon formation of the complex. Their intensities, however, become negligible with respect to the most intense transitions associated with bands which have contributions from the N-H or H-Br stretch coordinates. Depending on the frequency region of the local proton stretching vibration, modes of the monomer with a_1 symmetry often experience noticeable changes in their intensity due to the strong coupling with the motion of the proton. One exception is the a_1 mode Q_{10} of 3,5-DCP at 1221 cm^{-1} (Table 4-4) which corresponds to the modes (Q_{11}) at 1217 cm^{-1} and 1212 cm^{-1} in the complex (Table 4-6) without any significant contributions from the N-H or H-Br stretch. Similarly, the a_1 mode Q_{13} at 1033 cm^{-1} (Table 4-4) is also not calculated to couple with the proton stretch upon formation of the complex.

The simulated spectra for the computed HBr:3,5-DCP and HBr:3,5-DCP:2Ne complexes are shown together with the experimental extracted spectrum in Figure 4-16. There are no bands observed in the higher frequency region that originate from the complex. Modes with a_1 symmetry that do not couple with the proton local oscillator are too weak to be seen in the computed spectra. Figure 4-16 illustrates graphically the dramatic effect that two neon atoms can have on the calculated spectrum of the complex. It is clear, however, that neither computed spectrum matches the extracted experimental spectrum. Even the computed spectrum for the HBr:3,5-DCP:2Ne complex, which has

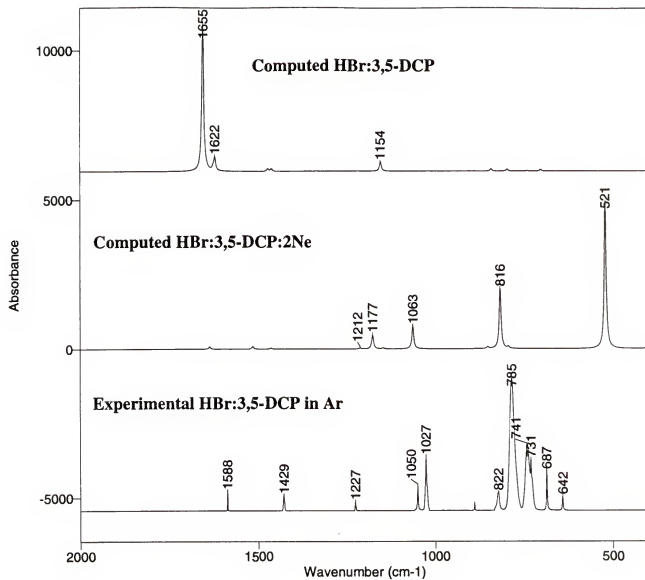


Figure 4-16. The computed MP2/6-31+G(d,p) spectra of HBr:3,5-DCP and HBr:3,5-DCP:2Ne, and the extracted experimental Ar matrix spectrum of HBr:3,5-DCP.

several strong absorptions below 1000 cm^{-1} , does not compare well with the experiment both in the intensity pattern and the frequencies.

6. Force Field Treatment

Possible causes for the discrepancies shown in the previous section have been proposed for the HBr:pyridine complex and can result from two factors. One limitation, of experimental nature, is the use of a matrix that may significantly affect forces and motions within the complex. Even though the MP2/6-31 +G(d,p) calculation including two neon atoms does not model a matrix, it shows that the environment potentially has a strong influence on the geometry and the spectral properties of a complex where the proton is on the brink of transfer.

The second limitation arises from the use of the harmonic approximation by the Gaussian program in the computation of the vibrational frequencies and intensities. In section A-5 of this Chapter, good agreement between the experimental spectrum and the theoretical calculation was obtained by reducing the effective force constant for the hydrogen-bonded proton stretch by multiplying the harmonic force constants by $(\nu_{\text{anh}}/\nu_{\text{har}})^2$, where ν_{anh} is the frequency for transition between the first two vibrational levels from the anharmonic potential.

At the MP2/6-31+G(d,p) level of theory, it was not possible to compute a series of single point energies along the normal coordinate for the proton stretch of the HBr:3,5-DCP complex in order to obtain a one dimensional anharmonic potential. A two dimensional treatment, as presented for the BrH:NH₃ complex,¹¹¹ would be even more difficult. In addition, it is likely that such treatments might still not account very well for

the discrepancy between experiment and theory since the environment may also be more influential for the HBr:3,5-DCP complex than for the HBr:pyridine complex.

In an attempt to account empirically for the effects of anharmonicity and environment, a dichotomy search was performed on the force constant scaling factors α for the NH and HBr stretch coordinates only. With our approach, all the symmetry force constants are assumed to be unchanged from the original calculation except for the effective force constant for the hydrogen-bonded proton stretching normal mode. The latter is a linear combination of three symmetry force constants: the diagonal HBr constant, the diagonal NHs constant and the off-diagonal interaction constant between them. If $F_{(\text{HBr}, \text{HBr})}$ is scaled by α_{HBr} and $F_{(\text{NHs}, \text{NHs})}$ is scaled by α_{NHs} then the coupling $F_{(\text{HBr}, \text{NHs})}$ is scaled by the geometric mean $(\alpha_{\text{HBr}}\alpha_{\text{NHs}})^{1/2}$. In addition, all off-diagonal coupling constants involving the HBr or NHs symmetry coordinate are also scaled by the geometric mean (here $\alpha_{\text{HBr}}^{1/2}$ or $\alpha_{\text{NHs}}^{1/2}$ since the other diagonal force constants are not modified). The method employed here is somewhat similar to the scaled quantum mechanical (SQM) force field proposed by Fogarasi and Pulay.¹¹² The theoretical force constant matrix \mathbf{F}^{th} is scaled according to:

$$\mathbf{F} = \mathbf{C}^{1/2} \mathbf{F}^{\text{th}} \mathbf{C}^{1/2}, \quad (4-2)$$

where \mathbf{C} is the diagonal matrix of the square root of the scale factors. The two scale factors α_{HBr} and α_{NHs} were optimized in order to minimize not only the deviation between the calculated and observed frequencies but also the deviation between calculated and experimental intensities. This empirical method of choosing these factors is not unique and several sets of factors are possible.

One of the best agreements between the frequencies and intensities of the experimental and the re-computed spectra involves a significant reduction of the HBr stretching force constant. Satisfactory agreement was obtained with the factors $\alpha_{\text{HBr}} = 0.30$ and $\alpha_{\text{NH}_3} = 0.67$. Table 4-7 presents the results for the most intense transitions of the HBr:3,5-DCP complex before (original) and after modification of the force field. Experimental frequencies and intensities are also given in brackets. The corresponding spectra are shown in Figure 4-17.

Since the force field in symmetry coordinate is block diagonal, the modes with symmetry other than a_1 are not affected by the scaling applied above. Because some of the b_2 symmetry modes are strong enough to appear in spectrum, it is logical to scale their frequencies (Figure 4-17b) by the usual 0.97 factor employed for the monomer. Frequencies in Table 4-7 are reported unscaled.

Regardless of the values chosen for α_{HBr} and α_{NH_3} , it was not possible to obtain two very strong absorptions in the calculation with frequencies below 800 cm^{-1} matching the extracted experimental results (784 and 741 cm^{-1}). Therefore the total integrated intensity from these two components at 784 and 741 cm^{-1} was represented as one single strong band in the reconstituted experimental spectrum in Figure 4-17c. Similar splittings in many other complexes have been observed and it has been suggested¹¹³ that Fermi resonance between the strong fundamental vibration of the complex ν_s and a combination involving a low-frequency lattice-mode ν_l ($\nu_s + \nu_l$) is responsible for the two bands. At the present time there is no definitive explanation for the existence of those two bands.

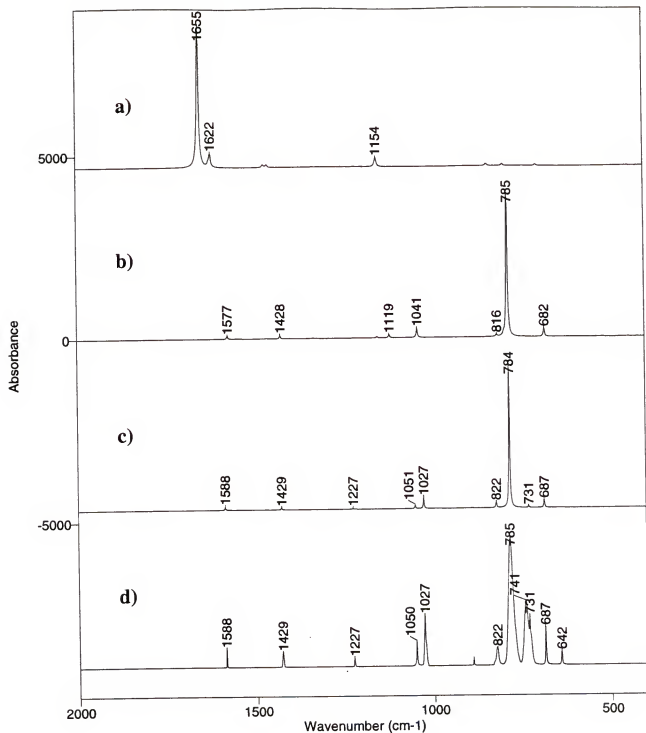


Figure 4-17. Infrared spectra for the HBr:3,5-DCP complex: a) computed harmonic; b) re-computed after force field treatment; c) experimental integrated intensity sum; and d) experimental extracted.

Table 4-7. Computed MP2/6-31+G(d,p) and re-computed^a frequencies (ν , cm^{-1}), intensities (A, km mol^{-1}), PEDs (%), and IDs (km mol^{-1}) for the most intense vibrations of the HBr:3,5-DCP complex. Comparison with experimental values^b given in brackets.

Original MP2/6-31+G(d,p)						Adjusted force field re-computed					
Q	ν	A	S_j	(PED)	[ID]	Q	ν	A	S_j	(PED)	[ID]
4	1655	3994	11a1 HBrS 12a1 NHs	(117+) (-26+)	[2238] [1725]						
5	1626	84	25b2 C3C4 23b2 CN 30b2 C4Hb 27b2 C3C1	(51-) (23+) (11+) (1+)	[27] [-13] [14] [29]	4	1626 (1588)	84 (75)	25b2 C3C4 23b2 CN 30b2 C4Hb 27b2 C3C1	(51-) (23+) (11+) (1+)	[27] [-13] [14] [29]
6	1622	339	2a1 C2C3 7a1 C2Hb 3a1 C3C4 1a1 NC 11a1 HBrS 12a1 NHs	(48+) (13+) (11-) (11-) (9-) (-2-)	[-21] [-32] [9] [34] [184] [176]	5	1624	0	2a1 C2C3 7a1 C2Hb 1a1 NC 3a1 C3C4	(50-) (17-) (13+) (11+)	[0] [-1] [1] [0]
7	1473	74	28b2 C2Hb 24b2 C2C3 23b2 CN 30b2 C4Hb 27b2 C3C1 33b2 BrHb	(30-) (28-) (22-) (14+) (2+) (1-)	[10] [41] [9] [12] [25] [-15]	6	1473 (1429)	74 (52)	28b2 C2Hb 24b2 C2C3 23b2 CN 30b2 C4Hb 27b2 C3C1 33b2 BrHb	(30-) (28-) (22-) (14+) (2+) (1-)	[10] [41] [9] [12] [25] [-15]
8	1462	71	7a1 C2Hb 3a1 C3C4 1a1 NC 11a1 HBrS 5a1 C3C1 12a1 NHs	(44-) (35-) (8+) (3+) (2+) (-1+)	[-22] [-7] [11] [47] [-11] [49]	7	1467	12	7a1 C2Hb 3a1 C3C4	(45-) (35-)	[9] [3]
10	1335	11	28b2 C2Hb 30b2 C4Hb 24b2 C2C3	(53+) (34+) (10-)	[-5] [7] [8]	9	1335 (1227)	11 (22)	28b2 C2Hb 30b2 C4Hb 24b2 C2C3	(53+) (34+) (10-)	[-5] [7] [8]
12	1154	36	30b2 C4Hb 24b2 C2C3 25b2 C3C4 27b2 C3C1	(38+) (26+) (16+) (9-)	[-10] [21] [6] [26]	12	1154	36	30b2 C4Hb 24b2 C2C3 25b2 C3C4 27b2 C3C1	(38+) (26+) (16+) (9-)	[-10] [21] [6] [26]
13	1153	222	1a1 NC 5a1 C3C1 12a1 NHs 11a1 HBrS	(62+) (18-) (0-) (0+)	[36] [49] [81] [31]	11	1154 (1051)	87 (83)	1a1 NC 5a1 C3C1 12a1 NHs	(62+) (18-) (0-)	[23] [31] [27]
14	1034	1	10a1 R1 3a1 C3C4 2a1 C2C3	(67-) (18-) (11-)	[2] [0] [0]	13	1041 (1027)	242 (276)	10a1 R1 3a1 C3C4 11a1 HBrS 12a1 NHs	(68-) (17-) (2+) (1-)	[29] [-5] [92] [108]
15	902	5	32b2 NHBrb 27b2 C3C1	(80-) (11-)	[-4] [8]	14	902 (890)	5 (15)	32b2 NHBrb 27b2 C3C1	(80-) (11-)	[-4] [8]
18	841	61	27b2 C3C1 31b2 R3 32b2 NHBrb	(41-) (29-) (17+)	[50] [5] [7]	17	841 (822)	61 (152)	27b2 C3C1 31b2 R3 32b2 NHBrb	(41-) (29-) (17+)	[50] [5] [7]
20	740	13	22b1 NHBrb	(97+)	[12]	19	786 (784)	4075 (3960)	11a1 HBrS 12a1 NHs	(116-) (-31-)	[2220] [1867]
						20	740 (731)	13 (43)	22b1 NHBrb	(97+)	[12]

Table 4-7 -- continued

Original MP2/6-31+G(d,p)						Adjusted force field re-computed					
Q	v	A	S _j	(PED)	[ID]	Q	v	A	S _j	(PED)	[ID]
21	702	44	9a1 R2	(56-)	[8]	21	682	239	9a1 R2	(48-)	[-17]
			5a1 C3C1	(16+)	[-12]		{687	222}	11a1 HBrs	(24-)	[185]
			2a1 C2C3	(15+)	[1]				5a1 C3C1	(14+)	[26]
			12a1 NHs	(7-)	[41]				2a1 C2C3	(12+)	[-3]
									12a1 NHs	(-5-)	[59]

a) Re-computed with scale factors $\alpha_{\text{HBrs}} = 0.30$ and $\alpha_{\text{NHs}} = 0.67$ (see text).

b) Experimental data are assigned based on the re-computed results.

C. The HBr:4-chloropyridine Complex

1. Infrared Spectra and Analysis of 4-chloropyridine

Isolating 4-chloropyridine (4-CP) in Ar matrix required a slight modification to the experimental set-up described in Chapter 2. Solid 4-CP is not obtainable commercially because of excessive decomposition at room temperature. The source of 4-CP vapor was instead provided by the fractionation under reduced pressure of 4-chloropyridinium chloride (from Aldrich, 99% purity). In order to avoid the deposition of hydrogen chloride on the cold window, a thin (~ 1 mm inner diameter) and long (~ 30 cm) tubular copper coil was inserted between the source container and the quick connect of the cryostat chamber. The copper surface acted as a very efficient trap for HCl. The spectra thus obtained revealed no visible trace of monomeric HCl.

The experimental spectrum of 4-CP isolated in argon matrix is compared with computed MP2/6-31+G(d,p) and B3LYP/6-31G(d,p) simulated spectra, in Figures 4-18 and 4-19. Besides pyridine, 4-CP is the only system for which a DFT calculation was carried out. This comparison compares the two computation methods and proved to be useful for the final assignment of 4-CP. The latter is given in Table 4-8 with the 27 normal frequencies, intensities, symmetry coordinates, PEDs and IDs from both calculations together with the tabulated experimental results. The experimental absolute intensities are based on the DFT results excluding modes below 400 cm^{-1} and the C-H stretch intensities.

Examination of the experimental spectrum in the C-H stretch region (Figure 4-18b) shows three bands where two unresolved doublets are expected according to both calculations (Table 4-8). One of the two bands at 3057 cm^{-1} and 3050 cm^{-1} (Figure

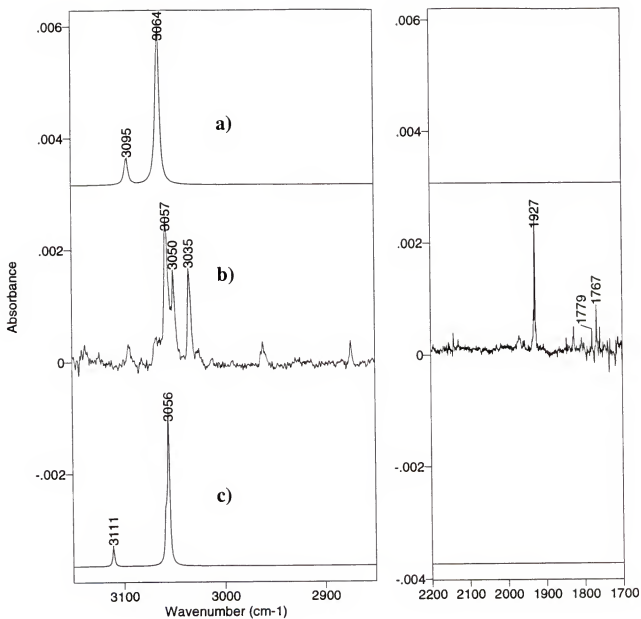


Figure 4-18. Infrared spectra of 4-chloropyridine in the region from 3150 to 2850 cm^{-1} . The region from 2200 to 1700 cm^{-1} shows some strong overtones and combinations. a) Computed MP2/6-31+G(d,p). b) Isolated in an argon matrix at 10 K (baseline corrected). c) Computed B3LYP/6-31G(d,p).

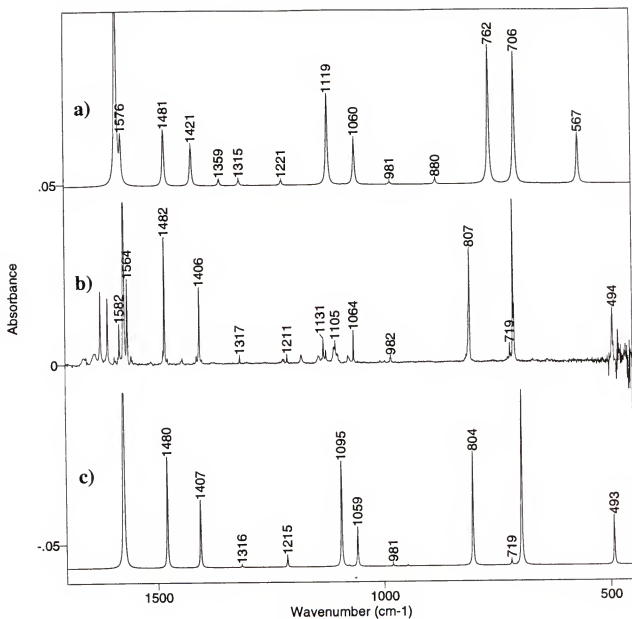


Figure 4-19. Infrared spectra of 4-chloropyridine in the region from 1700 to 400 cm^{-1} . The strongest band around 1570 cm^{-1} is off-scaled in order to better view the weaker ones. a) Computed MP2/6-31+G(d,p). b) Isolated in an argon matrix at 10 K (baseline corrected). c) Computed B3LYP/6-31G(d,p).

Table 4-8. The 27 vibrational modes of 4-chloropyridine from ab initio calculations at the MP2/6-31+G(d,p) and B3LYP/6-31G(d,p) level of theory, and from argon matrix at 10K. Frequencies (ν , cm^{-1}), intensities (A, km mol^{-1}), PEDs (%), and IDs (km mol^{-1}).

MP2/6-31+G(d,p)						Ar Matrix		B3LYP/6-31G(d,p)							
Q	V	V_{ex}^{a}	A	S_i	(PED)	[ID]	V	A	Q	V	V_{ex}^{b}	A	S_i	(PED)	[ID]
1	3287	3096	.2	5a1 C3H	(93+)	[0]			1	3227	3111	.1	5a1 C3H	(97+)	[0]
2	3286	3096	3.5	23b2 C3H	(95+)	[1]			2	3227	3111	3.6	23b2 C3H	(98+)	[2]
3	3255	3066	3.1	4a1 C2H	(93-)	[2]	3058 7.5 3050 1.4 3035 1.6 sum = 10.5		3	3173	3059	9.8	4a1 C2H	(97-)	[7]
4	3253	3064	20.0	22b2 C2H	(95-)	[17]			4	3170	3056	30.2	22b2 C2H	(98-)	[25]
5	1635	1586	99.7	2a1 C2C3 3a1 C3C4 8a1 C3Hb 9a1 R2 1a1 NC 6a1 C4C1	(46-) (16+) (14+) (8-) (29) (7+) (16) (20)	[15] [11] [16] [29] [16] [20]	1572 93.5		6	1619	1575	116.3	2a1 C2C3 7a1 C2Hb 3a1 C3C4 8a1 C3Hb 1a1 NC 9a1 R2 6a1 C4C1	(47-) (13-) (12+) (11+) (17) (10+) (8-) (33) (19) (0+)	[25] [10] [13] [17] [20] [33] [19]
6	1625	1576	13.5	21b2 C3C4 19b2 CN	(55-) (26+)	[-1] [8]	1564 21.0		5	1620	1576	25.8	21b2 C3C4 19b2 CN	(49-) (32+)	[3] [15]
7	1527	1482	18.8	7a1 C2Hb 8a1 C3Hb 3a1 C3C4 1a1 NC	(45-) (23-) (15-) (14+)	[7] [8] [4] [-8]	1482 29.4		7	1521	1480	32.4	7a1 C2Hb 8a1 C3Hb 3a1 C3C4 1a1 NC 6a1 C4C1	(38-) (28-) (18-) (14+) (1+)	[8] [12] [18] [-10] [13]
8	1465	1421	13.5	20b2 C2C3 24b2 C2Hb 25b2 C3Hb	(48+) (39+) (12-)	[11] [3] [4]	1406 18.5		8	1446	1407	19.4	24b2 C2Hb 20b2 C2C3 25b2 C3Hb	(49+) (30+) (11-)	[4] [11] [4]
9	1402	1359	2.0	19b2 CN 24b2 C2Hb 21b2 C3C4	(59-) (20-) (13-)	[4] [1] [0]			10	1294	1259	.0	19b2 CN 21b2 C3C4 20b2 C2C3	(49+) (37+) (12-)	[0] [0] [0]
10	1356	1315	1.8	25b2 C3Hb 24b2 C2Hb 21b2 C3C4	(46-) (24-) (21+)	[2] [-1] [0]	1317 1.2		9	1352	1316	.6	25b2 C3Hb 24b2 C2Hb 20b2 C2C3	(48-) (32-) (12+)	[1] [0] [1]
11	1259	1221	1.7	7a1 C2Hb	(41-)	[1]	1221 2.0		11	1249	1215	3.1	7a1 C2Hb	(44-)	[2]

Table 4-8 -- continued

MP2/6-31+G(d,p)										B3LYP/6-31G(d,p)									
Ar Matrix																			
Q	V	V _{calc} ^{a)}	A	S _i	(PED)	[ID]	v	A		Q	V	V _{calc} ^{b)}	A	S _i	(PED)	[ID]			
22	584	567	16.8	17b1 R1o 18b1 R2o 15b1 C3Hw 14b1 C2Hw	(91+) (15-) (11-) (-14-)	[-5] [12] [17] [-10]	719	2.4		20	739	719	1.6	17b1 R1o 14b1 C2Hw	(118-) (-10+)	[1] [-2]			
23	420	407	.6	9a1 R2 6a1 C4Cl	(46-) (40+)	[-1] [2]				24	412	401	2.0	6a1 C4Cl 9a1 R2	(46+) (41-)	[4] [-2]			
24	385	374	7.3	16b1 C4Clw 18b1 R2o	(59-) (42-)	[-8] [17]	494	17.7		23	506	493	14.1	18b1 R2o 16b1 C4Clw	(61+) (43+)	[24] [-10]			
25	368	357	.0	13a2 R3o	(115+)	[0]				25	393	382	.0	13a2 R3o	(116+)	[0]			
26	300	291	1.4	26b2 C4Clb	(90+)	[1]				26	299	291	1.5	26b2 C4Clb	(90+)	[1]			
27	173	168	2.0	18b1 R2o 16b1 C4Clw	(52+) (41-)	[3] [1]				27	188	183	2.7	18b1 R2o 16b1 C4Clw	(54+) (40-)	[3] [1]			
Total IR int.					343.2					Total IR int.					398.0				

a) Frequencies below 2000 cm⁻¹ scaled by 0.970, by 0.942 above 2000 cm⁻¹.b) Frequencies below 2000 cm⁻¹ scaled by 0.973, by 0.964 above 2000 cm⁻¹.

c) Raman data from reference (115).

4-18b) is definitely the combination $1572 + 1484$ (B_2) in Fermi resonance with the b_2 fundamental. Since all three transitions have b_2 symmetry, this resonance may modify the intensity distribution of the fundamentals. Hence, no precise assignment is given for this region. Fewer strong combination bands appear in the region from 1700 cm^{-1} to 2200 cm^{-1} than for pyridine or 3,5-DCP. Cook and Church¹¹⁴ proposed that the position and intensity of the combination-tones in this region were characteristic of the position of the substituent. The few Raman data available^{115,116} allow us to propose the assignment of some of these bands. As for pyridine and 3,5-DCP, several of these absorptions arise from combinations of out-of-plane C-H wagging fundamentals, in particular the a_2 mode reported¹¹⁵ at 955 cm^{-1} (which is in good agreement with the scaled DFT result Q_{16} at 968 cm^{-1} (Table 4-8)). Thus, we assign $1927: 955 \times 2$ (A_1) or $712 + 1211$ (A_1); $1826: 914 \times 2$ (A_1); $1766: 955 + 807$ (B_2).

In general there is a remarkable agreement between the B3LYP/6-31G(d,p) simulated spectrum and the experimental spectrum shown in Figure 4-19 for the lower spectral region. The comparison with the MP2/6-31+G(d,p) spectrum (Figure 4-19a) shows the problems in predicting accurately the frequencies and intensities of the out-of-plane modes at this level of theory. The frequencies of the modes Q_{19} at 762 cm^{-1} (observed at 807 cm^{-1}) and Q_{22} at 567 cm^{-1} (observed at 719 cm^{-1}) are too low and their intensities are overestimated.

The band observed at 1582 cm^{-1} (figure 4-19b) originates from the $\text{H}_2\text{O}:4\text{-CP}$ complex. The assignment of the bands observed around 1100 cm^{-1} is difficult because there are a number of weak bands spread over a wide frequency range. They are grouped together in Table 4-8 and assigned to the mode Q_{19} at 1119 cm^{-1} .

2. Infrared Spectra of the HBr:4-CP Complex

The 4-chloropyridinium bromide was prepared by addition of 20% potassium carbonate to a cold aqueous solution of 4-CP hydrochloride. The basic solution obtained was extracted with methylene chloride, into which 4-CP was extracted. The methylene chloride solution was washed with water four times and then evaporated. The residue was mixed with aqueous 48% hydrobromic acid in equivalent amounts to give 4-CP hydrobromide. Water was evaporated under vacuum, and the colorless salt was sublimed at 13 torr. There was no CAS registry number found for this salt. The salt sublimed well by itself at room temperature and did not require additional heating.

The spectrum of 4-CP in the argon matrix after annealing is compared with the spectra of the mixture Ar + HBr + 4-CP before and after annealing in Figure 4-20 for the lower spectral region. No new bands were observed above 1700 cm^{-1} for the three component mixture except for those due to HBr and the HBr:water complex.

The concentrations of the different species were obtained, as explained in Chapter 2, in a sample with matrix thickness $\ell = \ell_1 + \ell_2 = 144 + 6 = 150\text{ }\mu\text{m}$, using the measured integrated absorbances and calculated intensities for those species. Using the MP2/6-31+G(d,p) integrated molar absorption coefficients given in Section A-3 of this chapter and $[A(Q_7;4\text{-CP}) = 18.8\text{ km/mol}]$, the concentrations before annealing were: $C(\text{HBr}) \approx C(4\text{-CP}) \approx 1 \times 10^{-2}\text{ mol L}^{-1}$; $C(\text{HBr})_2 \approx 8 \times 10^{-6}\text{ mol L}^{-1}$, $C(\text{H}_2\text{O}) \approx 1 \times 10^{-3}\text{ mol L}^{-1}$ and $C(\text{HBr:H}_2\text{O}) \approx 1 \times 10^{-5}\text{ mol L}^{-1}$. The absolute concentration of the complex after annealing was estimated to be $C(\text{BrH:4-CP}) = 8 \times 10^{-5}\text{ mol L}^{-1}$ from the computed intensity $[A(\text{BrH:4-CP}) = 8260\text{ km mol}^{-1}]$ (sum of the strong a_1 modes of the complex

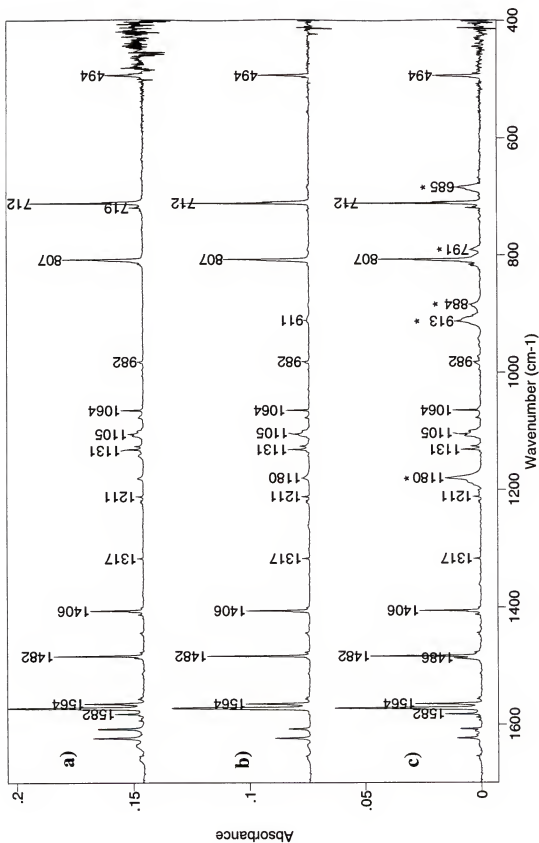


Figure 4-20. Experimental infrared matrix spectra, after correction to a horizontal baseline, in the region from 1700 to 400 cm⁻¹ for 4-CP + Ar (a), and for HBr + 4-CP + Ar before (b) and after (c) annealing.

above 400 cm^{-1}). The relative concentration [Ar:HBr:4-CP:complex] was estimated to be [4000:1:1:0.008].

Examination of the spectrum after annealing (Figure 4-20c) shows the emergence of three strong absorptions around 1180 cm^{-1} , $913/884\text{ cm}^{-1}$ and 685 cm^{-1} , which were attributed to the one-to-one HBr:4-CP complex. The integrated intensity of these four bands increases after annealing by a factor of about nine. Two smaller bands at 1361 cm^{-1} and 791 cm^{-1} are also attributed to the complex but with greater uncertainty given the difficulty of evaluating their rate of growth. As before, the number of new bands (after annealing) related to the complex is much smaller than the number of IR-active modes expected for the complex ($3N-6-3(a_2) = 30$). The majority of these 30 modes are not observed because they are too weak (see Table 4-9) to be detected in very dilute matrices. The frequencies of the bands of the HBr:4-CP complex are much lower than that of the monomeric HBr vibration at 2568 cm^{-1} . The spectrum of solid 4-chloropyridinium bromide (not shown) annealed to 221K and recorded at 10K revealed that the frequency of the strongest absorption of the solid (2562 cm^{-1}), associated with the N-H stretching vibration, is much higher than that of the complex, as was also the case for pyridinium bromide described in Section A-3.

3. Theoretical Prediction and Force Field Treatment

The geometry of the HBr:4-CP complex (C_{2v} symmetry), calculated at the MP2/6-31+G(d,p) level of theory, is comparable to that for the HBr:pyridine complex in terms of distances between the three hydrogen-bonded atoms. The intermolecular Br-N distance of 2.948 \AA and the Br-H distance of 1.775 \AA are fairly close to the corresponding values for the HBr:pyridine homologue (2.958 \AA and 1.802 \AA respectively). The left

column of Table 4-9 presents the 33 normal frequencies, intensities, PEDs and IDs of the HBr:4-CP complex. Examination of the PEDs and IDs in this column confirms that the proton is transferred towards the nitrogen, as shown by the 83% contribution of the N-H stretch to the potential energy for the strongest mode Q_{10} at 1413 cm^{-1} . This frequency compares with 1561 cm^{-1} calculated for HBr:pyridine. Its value indicates that the proton is transferred to a lesser extent in HBr:4-CP than it is in HBr:pyridine. Comparison of the MP2/6-31+G(d,p) calculations for the complex (Table 4-9) and for the monomer (Table 4-8) shows that the frequencies of most vibrations are very close. However, normal modes of 4-CP that couple with the “NHs” and “HBrs” coordinates in the complex, exhibit much greater changes. The latter modes are often unique and generally cannot be correlated with modes of the monomer. As can be seen from the original calculation for the complex, only modes belonging to the a_1 symmetry group have relatively large molar absorption coefficients (100 km mol^{-1} or more).

The MP2/6-31+G(d,p) simulated spectrum and the experimental extracted spectrum are presented in Figure 4-21a and 4-21b for the region from 450 to 1650 cm^{-1} . It is obviously not possible to assign the experimental spectrum of the complex from this comparison, since neither the frequencies nor the intensity pattern match those of the computed spectrum. Here again, the anharmonicity of the proton stretching mode is likely to be the major factor contributing to the discrepancy between these results. The “NHs” and “HBrs” force constants from the harmonic calculation were adjusted as described in Section B-6 of this chapter. The new frequencies and intensities thus obtained were compared with the experimental values after each trial. As a starting point for the scaling factors, a rough evaluation of the anharmonicity correction was made

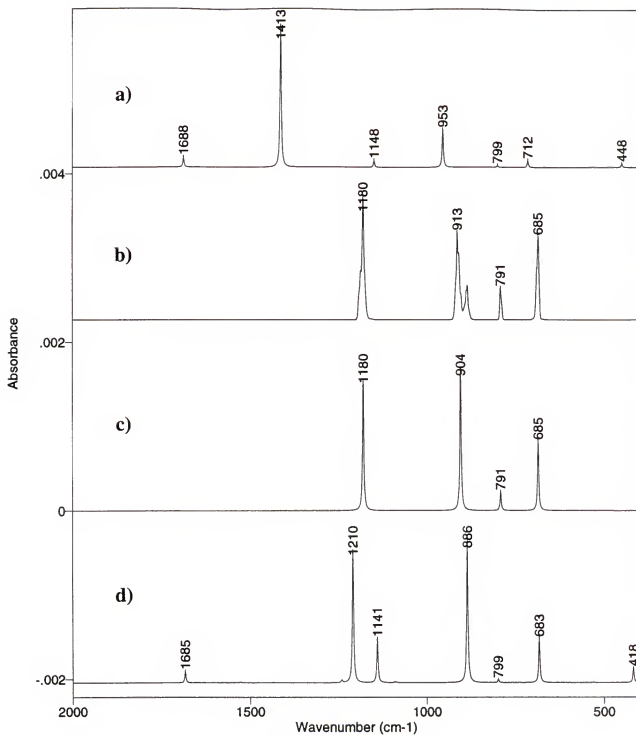


Figure 4-21. Infrared spectra for the HBr:4-CP complex: a) computed MP2/6-31+G(d,p); b) experimental extracted; c) experimental integrated intensity sum; and d) re-computed after force field treatment.

Table 4-9. Computed MP2/6-31+G(d,p) and re-computed^a frequencies (ν , cm^{-1}), intensities (A, km mol^{-1}), PEDs (%), and IDs (km mol^{-1}) for the HBr:4-CP complex. Comparison with experimental values^b given in brackets.

Original MP2/6-31+G(d,p)						Adjusted force field re-computed					
Q	ν	A	S_j	(PED)	[ID]	Q	ν	A	S_j	(PED)	[ID]
1	3302	0	5a1 C3H 4a1 C2H	(80+) (19+)	[0] [1]	1	3302	1	5a1 C3H 4a1 C2H	(80+) (19+)	[0] [1]
2	3301	3	27b2 C3H 26b2 C2H	(86+) (13+)	[3] [1]	2	3301	3	27b2 C3H 26b2 C2H	(86+) (13+)	[3] [1]
3	3285	7	4a1 C2H 5a1 C3H	(80-) (19+)	[8] [0]	3	3285	9	4a1 C2H 5a1 C3H	(81-) (19+)	[9] [0]
4	3285	0	26b2 C2H 27b2 C3H	(86-) (14+)	[1] [0]	4	3285	0	26b2 C2H 27b2 C3H	(86-) (14+)	[1] [0]
5	1688	373	2a1 C2C3 1a1 NC 7a1 C2Hb 9a1 R2 12a1 NHs 11a1 HBrs	(44+) (14-) (14+) (10+) (2+) (0+)	[18] [68] [-37] [66] [114] [66]	5	1685	218	2a1 C2C3 7a1 C2Hb 1a1 NC 9a1 R2 12a1 NHs 6a1 C4C1	(46+) (14+) (13-) (9+) (0+) (0+)	[14] [-28] [51] [50] [54] [24]
6	1654	8	23b2 CN 25b2 C3C4 32b2 NHBrb	(37+) (35-) (11+)	[10] [-6] [2]	6	1654	8	23b2 CN 25b2 C3C4 32b2 NHBrb	(37-) (35+) (11-)	[10] [-6] [2]
7	1540	3	8a1 C3Hb 7a1 C2Hb 3a1 C3C4 1a1 NC 12a1 NHs	(31-) (29-) (21-) (15+) (2-)	[-3] [-4] [-3] [6] [10]	7	1538	7	7a1 C2Hb 8a1 C3Hb 3a1 C3C4 1a1 NC	(32-) (31-) (20-) (14+)	[7] [5] [5] [-8]
8	1529	18	28b2 C2Hb 24b2 C2C3 32b2 NHBrb 25b2 C3C4	(29+) (26+) (26+) (10+)	[9] [19] [3] [4]	8	1529	18	28b2 C2Hb 24b2 C2C3 32b2 NHBrb 25b2 C3C4	(29+) (26+) (26+) (10+)	[9] [19] [3] [4]
9	1479	6	24b2 C2C3 25b2 C3C4 23b2 CN 32b2 NHBrb	(31+) (27-) (22-) (13-)	[13] [-4] [-7] [-1]	9	1479	6	24b2 C2C3 25b2 C3C4 23b2 CN 32b2 NHBrb	(31-) (27+) (22+) (13+)	[13] [-4] [-7] [-1]
10	1413	5675	12a1 NHs 10a1 R1 11a1 HBrs	(83-) (12-) (-9-)	[2729] [-24] [2878]	13	1210 (1180 2453)	2788 (1180 2453)	12a1 NHs 10a1 R1 11a1 HBrs	(47-) (24-) (-7-)	[1452] [-23] [1388]
11	1350	0	29b2 C3Hb 28b2 C2Hb 25b2 C3C4	(51-) (29-) (15+)	[0] [0] [0]	10	1350	0	29b2 C3Hb 28b2 C2Hb 25b2 C3C4	(51-) (29-) (15+)	[0] [0] [0]
12	1329	2	32b2 NHBrb 23b2 CN 28b2 C2Hb	(44+) (29-) (24-)	[-1] [3] [2]	11	1329	2	32b2 NHBrb 23b2 CN 28b2 C2Hb	(44+) (29-) (24-)	[-1] [3] [2]
13	1242	7	7a1 C2Hb 8a1 C3Hb 2a1 C2C3 1a1 NC	(44-) (26+) (14+) (13-)	[6] [-3] [1] [5]	12	1242	55	7a1 C2Hb 8a1 C3Hb 1a1 NC 2a1 C2C3 12a1 NHs 11a1 HBrs	(46-) (24+) (15-) (13+) (0+) (0+)	[16] [-9] [16] [2] [16] [14]
14	1148	264	3a1 C3C4 6a1 C4C1	(40+) (25-)	[29] [98]	14	1141	918	3a1 C3C4 2a1 C2C3	(34+) (23+)	[51] [-12]

Table 4-9 -- continued

Original MP2/6-31+G(d,p)							Adjusted force field re-computed						
Q	v	A	S _q	(PED)	[ID]		Q	v	A	S _q	(PED)	[ID]	
			2a1 C2C3	(16+)	[-5]					6a1 C4C1	(21-)	[164]	
			8a1 C3Hb	(10-)	[-11]					12a1 NHs	(9-)	[355]	
			12a1 NHs	(2-)	[72]					11a1 HBrs	(-2-)	[309]	
			11a1 HBrs	(-1-)	[60]								
15	1124	1	24b2 C2C3	(36-)	[-3]		15	1124	1	24b2 C2C3	(36-)	[-3]	
			29b2 C3Hb	(32-)	[1]					29b2 C3Hb	(32-)	[1]	
			28b2 C2Hb	(16+)	[1]					28b2 C2Hb	(16+)	[1]	
			23b2 CN	(10-)	[-1]					23b2 CN	(10-)	[-1]	
16	1095	4	1a1 NC	(32-)	[-6]		16	1091	23	10a1 R1	(41-)	[-3]	
			10a1 R1	(29-)	[-1]					1a1 NC	(23-)	[-13]	
			8a1 C3Hb	(22-)	[-2]					8a1 C3Hb	(20-)	[-4]	
			11a1 HBrs	(1+)	[10]					12a1 NHs	(1-)	[18]	
										11a1 HBrs	(0+)	[25]	
17	1085	6	22b1 NHBrb	(94-)	[9]		17	1085	6	22b1 NHBrb	(94-)	[9]	
18	953	1518	10a1 R1	(44-)	[21]		20	886	2972	12a1 NHs	(43+)	[1242]	
			1a1 NC	(18+)	[-68]			{913	2674}	10a1 R1	(20-)	[19]	
			12a1 NHs	(12+)	[577]			{884}		1a1 NC	(16+)	[-85]	
			11a1 HBrs	(7-)	[893]					9a1 R2	(13+)	[99]	
										11a1 HBrs	(-9+)	[1587]	
19	941	0	13a2 C2Hw	(87+)	[0]		18	941	0	13a2 C2Hw	(87+)	[0]	
			14a2 C3Hw	(27+)	[0]					14a2 C3Hw	(27+)	[0]	
			15a2 R3o	(-14+)	[0]					15a2 R3o	(-14+)	[0]	
20	902	4	16b1 C2Hw	(77+)	[12]		19	902	4	16b1 C2Hw	(77+)	[12]	
			17b1 C3Hw	(30+)	[-7]					17b1 C3Hw	(30+)	[-7]	
21	859	0	14a2 C3Hw	(81+)	[0]		21	859	0	14a2 C3Hw	(81+)	[0]	
			13a2 C2Hw	(20-)	[0]					13a2 C2Hw	(20-)	[0]	
22	799	65	17b1 C3Hw	(69-)	[45]		22	799	65	17b1 C3Hw	(69-)	[45]	
			16b1 C2Hw	(28+)	[34]			{791	345}	16b1 C2Hw	(28+)	[34]	
			18b1 C4Clw	(3+)	[10]					18b1 C4Clw	(3+)	[10]	
			21b1 BrHw	(1-)	[30]					21b1 BrHw	(1-)	[30]	
			20b1 R2o	(-8-)	[-55]					20b1 R2o	(-8-)	[-55]	
23	712	275	9a1 R2	(35+)	[-50]		23	683	922	6a1 C4C1	(30+)	[-107]	
			6a1 C4C1	(29+)	[-61]			{685	1274}	9a1 R2	(25+)	[-77]	
			3a1 C3C4	(15+)	[10]					12a1 NHs	(19-)	[432]	
			11a1 HBrs	(11+)	[250]					3a1 C3C4	(14+)	[16]	
			12a1 NHs	(-1+)	[128]					10a1 R1	(12+)	[5]	
										11a1 HBrs	(-4-)	[671]	
24	662	0	31b2 R3	(88+)	[0]		24	662	0	31b2 R3	(88-)	[0]	
25	530	11	19b1 R1o	(80-)	[8]		25	530	11	19b1 R1o	(80-)	[8]	
			20b1 R2o	(26-)	[29]					20b1 R2o	(26-)	[29]	
			17b1 C3Hw	(11-)	[12]					17b1 C3Hw	(11-)	[12]	
			21b1 BrHw	(-2-)	[-31]					21b1 BrHw	(-2-)	[-31]	
			16b1 C2Hw	(-13+)	[-9]					16b1 C2Hw	(-13+)	[-9]	
26	448	155	6a1 C4C1	(36-)	[29]		26	418	304	9a1 R2	(48-)	[-31]	
			9a1 R2	(32+)	[-19]					6a1 C4C1	(34+)	[37]	
			11a1 HBrs	(25+)	[116]					11a1 HBrs	(7-)	[213]	
			12a1 NHs	(-6+)	[29]					12a1 NHs	(-1-)	[87]	
27	383	0	15a2 R3o	(116+)	[0]		27	383	0	15a2 R3o	(116+)	[0]	
28	371	4	18b1 C4Clw	(71-)	[-13]		28	371	4	18b1 C4Clw	(71+)	[-13]	
			20b1 R2o	(25-)	[25]					20b1 R2o	(25+)	[25]	

Table 4-9 -- continued

Original MP2/6-31+G(d,p)							Adjusted force field re-computed						
Q	v	A	S _j		(PED)	[ID]	Q	v	A	S _j		(PED)	[ID]
29	305	0	30b2	C4Clb	(89-)	[1]	29	305	0	30b2	C4Clb	(89-)	[1]
30	206	0	20b1	R2o	(30+)	[-1]	30	206	0	20b1	R2o	(30-)	[-1]
			21b1	BrHw	(28-)	[1]				21b1	BrHw	(28+)	[1]
			18b1	C4Clw	(24-)	[0]				18b1	C4Clw	(24+)	[0]
			19b1	R1o	(20-)	[0]				19b1	R1o	(20+)	[0]
31	191	24	11a1	HBrs	(67-)	[24]	31	119	89	11a1	HBrs	(114+)	[77]
			9a1	R2	(18+)	[2]				12a1	NHs	(-20+)	[11]
32	56	5	21b1	BrHw	(67-)	[3]	32	56	5	21b1	BrHw	(67-)	[3]
			20b1	R2o	(31-)	[2]				20b1	R2o	(31-)	[2]
33	42	6	33b2	BrHb	(98+)	[5]	33	42	6	33b2	BrHb	(98+)	[5]

a) Re-computed with scale factors $\alpha_{\text{HBrs}} = 0.35$ and $\alpha_{\text{NHs}} = 0.55$ (see text).

b) Experimental data are assigned based on the re-computed results.

based on the strongest band of the computed and experimental spectra. The computed frequency for this band is about 63% higher than the experimental one. The conversion of this correction factor from frequency to force constant gave the initial value $\alpha_{\text{HBr}} = \alpha_{\text{NH}_3} = (0.63)^2 = 0.40$. One of the most acceptable comparisons between the adjusted calculated spectrum and the experimental one was attained with the scale factors $\alpha_{\text{HBr}} = 0.35$ and $\alpha_{\text{NH}_3} = 0.55$. This result is graphically represented in Figure 4-21d and is in reasonably good agreement with the experimental intensity sum spectrum (Figure 4-21c). In the latter, the absorptions at 913 and 884 cm^{-1} were summed into one band for comparison purposes. The outcome is satisfactory considering the simplicity of the model.

The adjusted force field re-computed results are also shown in the right column of Table 4-9. The experimental frequencies and intensities are given in brackets. Note that the observed absorption at 791 cm^{-1} is assigned with much uncertainty to the b_1 symmetry mode Q_{22} at 799 cm^{-1} . This band is absent in Krypton matrices while all other transitions of the complex display very similar frequencies and intensities (see later in Chapter 5). In argon matrices however, this band grows systematically after annealing at the same rate as the other complex bands.

D. The HBr:4-methylpyridine Complex

1. Infrared Spectra and Analysis of 4-methylpyridine

The infrared spectra for 4-methylpyridine (4-MP) isolated in argon matrix at 10 K, in the gas phase at 300 K and from MP2/6-31+G(d,p) calculations are shown in Figure 4-22 for the spectral region from 1700 to 2200 cm^{-1} and from 2850 to 3150 cm^{-1} and in

Figure 4-23 for the spectral region from 400 to 1700 cm^{-1} . Like pyridine, 4-MP is a liquid at room temperature and the experimental procedures for the acquisition of the vapor and matrix spectra are identical to those described for pyridine in Section A-1 of this chapter.

The assignment from *ab initio* results is given in Table 4-10. Because the presence of the methyl group breaks the C_{2v} symmetry, the geometry optimization and frequency calculation were carried out for C_s symmetry. The symmetry coordinate definition for 4-MP is given in Appendix C. This approach contrasts with existing calculations,¹¹⁷⁻¹¹⁹ all performed in C_{2v} symmetry with the methyl rotational mode (torsion) treated separately. When 4-MP is assumed to have C_{2v} symmetry, the 36 fundamental vibrations are divided into $12a_1 + 12b_1 + 8b_2 + 3a_2$, plus the methyl torsion, where in C_s symmetry 4-MP possesses $20a'$ and $16a''$ modes including the methyl torsion. Although all modes are supposed to be IR-active in C_s symmetry, the a_2 -equivalent modes are not expected to show significant absorption because the geometry of the ring does not deviate notably from that for C_{2v} symmetry in the conformation chosen for the molecule (no hydrogens from the methyl group are in the plane of the ring).

Observation of Figure 4-22 reveals a more complex C-H stretch region due to the increase in the number of C-H bonds. The Fermi resonances between fundamentals and combination-tones complicate the experimental spectra and are particularly noticeable in the matrix spectrum where the absorptions do not overlap as much as in the gas phase. Surprisingly, the band observed at 3000 cm^{-1} in the matrix and also prominent in the vapor spectrum was not reported in the most recent paper on 4-MP by Inoue *et al.*¹¹⁹ The impressive assignment they propose becomes questionable since it was made by

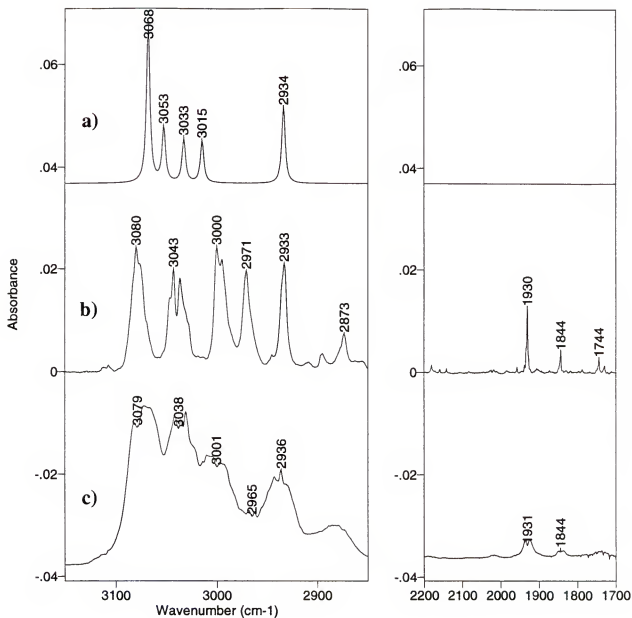


Figure 4-22. Infrared spectra of 4-methylpyridine in the region from 3150 to 2850 cm⁻¹. The region from 2200 to 1700 cm⁻¹ shows some strong overtones and combinations. a) Computed MP2/6-31+G(d,p). b) Isolated in an argon matrix at 10 K (baseline corrected). c) Gas phase at 300 K.

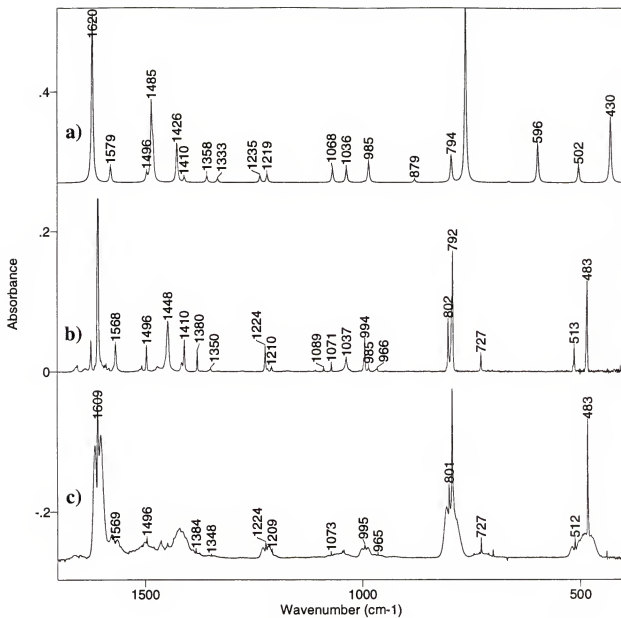


Figure 4-23. Infrared spectra of 4-methylpyridine in the region from 1700 to 400 cm^{-1} . The strongest band around 1610 cm^{-1} is off-scaled in order to better view the weaker ones. a) Computed MP2/6-31+G(d,p). b) Isolated in an argon matrix at 10 K (baseline corrected). c) Gas phase at 300 K.

Table 4-10. The 36 modes of vibration of 4-methylpyridine from MP2/6-31+G(d,p) calculation, Ar matrix at 10K and gas phase at 300K. Frequencies (ν , cm^{-1}), intensities (A, km mol^{-1}), PEDs (%), IDs (km mol^{-1}). Computation was carried out in Cs symmetry.

MP2/6-31+G(d,p)							C _{2v} class ^{c)}	Ar Matrix		Gas	
Q	ν	ν_{calc}	A	S _j	(PED)	[ID]		ν	A	ν	
1	3260	3071	.0	5a' C3H 4a' C2H	(60-) (39-)	[0] [0]	a1/b2				
2	3257	3068	42.1	29a" C3H 28a" C2H	(68-) (31-)	[20] [18]		3080 3043 3037 3000 2995 sum	14.2 15.6 13.3 43.1	3079B 3038B 3001B	
3	3241	3053	8.9	4a' C2H 5a' C3H	(60+) (39-)	[4] [4]					
4	3241	3053	5.7	28a" C2H 29a" C3H	(69-) (31+)	[10] [-5]					
5	3220	3033	11.6	34a" aMe	(100-)	[12]		2971 2933 2895 2873 sum =	10.6 8.6 5.1 24.3	2965 2936	
6	3200	3015	11.3	19a' Me o	(99-)	[11]					
7	3115	2934	20.4	11a' sMe	(99+)	[21]					
8	1670	1620	38.5	2a' C2C3 3a' C3C4 8a' C3Hb 9a' R2	(39-) (23+) (16+) (9-)	[3] [5] [9] [17]	a1	1608	46.8	1609A	
9	1628	1579	3.6	27a" C3C4 25a" CN	(49+) (23-)	[0] [3]	b2	1568	7.4	1569B	
10	1542	1496	1.8	7a' C2Hb 1a' NC 8a' C3Hb 3a' C3C4	(47+) (17-) (17+) (12+)	[2] [-3] [2] [1]	a1	1496	4.2	1497A	
11	1531	1485	16.6	36a" aMe s	(87+)	[11]	b2/b1	1448	23.6		
12	1527	1481	7.4	20a' Me sc	(92-)	[8]	b2/b1	1470	3.2		
13	1471	1426	8.9	26a" C2C3 30a" C2Hb 31a" C3Hb	(47+) (36-) (14+)	[6] [2] [3]	b2	1416 1410 sum =	3.1 4.7 7.8		
14	1453	1410	1.2	12a' Me um	(95+)	[1]	a1	1380	2.4	1384A	
15	1400	1358	1.4	25a" CN 30a" C2Hb 27a" C3C4	(61+) (17-) (12+)	[3] [0] [0]	b2	1350	0.7	1348B	
16	1374	1333	.9	31a" C3Hb 30a" C2Hb 27a" C3C4	(41-) (29-) (14-)	[1] [-1] [0]					
17	1273	1235	1.6	6a' C4Me 7a' C2Hb 2a' C2C3	(29-) (28-) (24+)	[-1] [1] [0]	a1	1224	4.7	1223A	
18	1257	1219	1.9	8a' C3Hb 7a' C2Hb 1a' NC 6a' C4Me	(39+) (17-) (16-) (11+)	[-2] [1] [2] [1]		1210	1.0	1209A	
19	1131	1097	.0	31a" C3Hb 26a" C2C3	(39+) (33-)	[0] [0]		1089	0		

Table 4-10 -- continued

MP2/6-31+G(d,p)							C _{2v} class ^{c)}	Ar Matrix		Gas
Q	v	v _{ref} ^{a)}	A	S _i	(PED)	[ID]		v	A	
				30a" C2Hb	(11-)	[0]				
20	1101	1068	3.1	10a' R1	(28+)	[-1]	a1	1071	0.8	1073A
				1a' NC	(27+)	[2]				
				8a' C3Hb	(25+)	[2]				
				3a' C3C4	(13-)	[-1]				
21	1068	1036	3.3	18a' Me ro	(85+)	[2]	b1	1037	6.1	1043
22	1027	996	.1	35a" Me ro	(71+)	[0]	b2?	966	0.9	965A
				27a" C3C4	(14-)	[0]				
23	1015	985	4.8	10a' R1	(42-)	[1]	a1	994	5.4	995A
				1a' NC	(32+)	[3]		985	0.9	
				2a' C2C3	(16+)	[0]			6.3	
24	941	913	.0	21a" C2Hw	(98-)	[0]	a2			969 ^{bi}
				22a" C3Hw	(14+)	[0]				
				23a" R3o	(-12-)	[0]				
25	906	879	.7	13a' C2Hw	(75-)	[4]				932
				14a' C3Hw	(37+)	[-3]				
				16a' R1o	(-12+)	[0]				
26	867	841	.0	22a" C3Hw	(93-)	[0]	a2			870 ^{bi}
				21a" C2Hw	(10-)	[0]				
27	819	795	6.1	6a' C4Me	(33+)	[1]	a1	802	9.1	801A
				3a' C3C4	(30+)	[-1]				
				9a' R2	(18+)	[4]				
				10a' R1	(13+)	[0]				
28	785	762	41.8	14a' C3Hw	(61-)	[31]	b1	792	26.6	793C
				13a' C2Hw	(34-)	[25]				
				17a' R2o	(-8-)	[-12]				
29	683	663	.3	33a" R3	(87-)	[0]				
30	615	596	8.5	16a' R1o	(99+)	[3]	b1	727	2.6	727C
				14a' C3Hw	(6-)	[11]				
				13a' C2Hw	(-12-)	[-8]				
31	518	503	3.8	9a' R2	(74+)	[4]	a1	513	3.3	513A
				6a' C4Me	(14-)	[0]				
32	443	430	14.6	17a' R2o	(54-)	[17]	b1	483	15.7	483C
				15a' C4Mew	(49-)	[1]				
33	367	356	.0	23a" R3o	(115+)	[0]	a2			385 ^{bi}
34	341	331	.1	32a" C4Meb	(84-)	[0]				
35	190	184	.1	17a' R2o	(51+)	[0]				
				15a' C4Mew	(40-)	[0]				
				16a' R1o	(10+)	[0]				
36	64	62	.2	24a" Me to	(99-)	[0]				

a) Frequencies below 2000 cm⁻¹ scaled by 0.970, by 0.942 above 2000 cm⁻¹.

b) From reference (117).

c) When possible, the class equivalent in C_{2v} symmetry is given (from ref. (117)).

optimizing the entire force field based on an incomplete set of observables. Experimental vibrations from the methyl and the ring C-H stretches (Figure 4-22b and 4-22c) are simply grouped in Table 4-10.

While the majority of the characteristic vibrations of 4-MP are well established,¹¹⁷⁻¹²³ we found some important differences. One of the most significant concerns the mode Q_{28} observed at 792 cm^{-1} and assigned by Inoue¹¹⁹ as a characteristic vibration with a_1 symmetry and a large PED contribution from the carbon - methyl stretch. Figure 4-23c shows that this band exhibits a contour C envelope and therefore cannot belong to the a_1 symmetry group. This intense vibration, which has large PED and ID contributions from the out-of-plane C-H waggings (Table 4-10), can be related to the most intense mode of pyridine at 700 cm^{-1} (Table 4-1).

Another discrepancy appears for the mode Q_{27} observed at 802 cm^{-1} in argon matrix and with a contour A envelope in the gas phase. Table 4-10 reveals a molecular motion with predominant PED contributions from the C4 - methyl stretch and ring stretches and bends. While Inoue¹¹⁹ attributes this band to out-of-plane C-H vibrations, Raman data¹¹⁸ confirm the in-plane nature of the molecular motion in view of its polarization. This mode is equivalent to the intense absorption in 4-CP observed at 712 cm^{-1} .

Examination of Figure 4-23 between 1400 and 1480 cm^{-1} reveals that the methyl scissors vibrations seem particularly sensitive to the matrix environment. The overlap of the rotational contours in this region prevent a reliable marking of the bands for the vapor spectrum, but it is clear that the broad absorption around 1420 cm^{-1} in the gas phase corresponds mostly to the band at 1448 cm^{-1} in the matrix. This blue shift of about 30

cm^{-1} is quite important for a matrix isolated monomer. Its assignment to the asymmetry methyl scissors (mode Q_{11}), as opposed to the symmetric scissors, was based solely on the similar values of the calculated and experimental intensities.

2. Infrared Spectra of the HBr:4-MP Complex

The salt of 4-methylpyridinium bromide is not available commercially but is easy to prepare and stable at room temperature. Equimolar amounts of 4-MP (Aldrich, 99% purity) and concentrated hydrobromic acid (48%) were mixed at 5 °C, evaporated to dryness and sublimed in vacuum to yield a colorless salt. A registry number was found for this salt and its crystallographic structure has been studied.¹²⁴ The sublimation of 4-methylpyridinium bromide was not sufficient at room temperature to provide enough deposition within a few hours. The results presented here were obtained by heating the salt to about 40 °C.

The spectra of 4-MP isolated in argon matrix and of a matrix containing Ar, HBr, 4-MP before and after annealing are presented in Figure 4-24 for the spectral region between 400 and 1700 cm^{-1} . The interference fringes (not shown) allowed the evaluation of the matrix thickness $\ell = \ell_1 + \ell_2 = 85 + 4 = 89 \mu\text{m}$. The concentrations of monomers and impurities before annealing were estimated to be $C(\text{HBr}) \approx C(Q_8, 4\text{-CP}) \approx 2 \times 10^{-2} \text{ mol L}^{-1}$; $C(\text{HBr})_2 \approx 4 \times 10^{-5} \text{ mol L}^{-1}$, $C(\nu_3, \text{H}_2\text{O}) \approx 1 \times 10^{-3} \text{ mol L}^{-1}$ and $C(\text{HBr}:\text{H}_2\text{O}) \approx 4 \times 10^{-6} \text{ mol L}^{-1}$. These results show that the HBr:4-MP is the hydrogen-bonded species most likely to be formed when diffusion is allowed. After the first annealing, the relative concentration [Ar:HBr:4-MP:complex] was estimated to be about [2000:1:1:0.02].

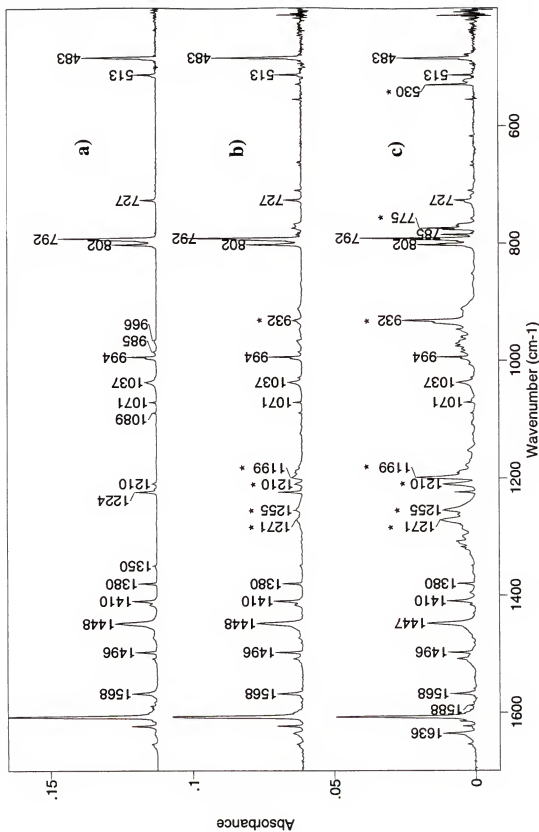


Figure 4-24. Experimental infrared matrix spectra, after correction to a horizontal baseline, in the region from 1700 to 400 cm⁻¹ for 4-MP + Ar (a), and for HBr + 4-MP + Ar before (b) and after (c) annealing.

A closer look at the isolated monomer and the three component mixture (Figures 4-24a and 4-24b) reveals that even with the very low concentration level estimated above for HBr and 4-MP, a non-negligible amount of one-to-one HBr:4-MP complex is present in the matrix before annealing. The four regions of strong absorption around 1272, 1199, 932 and 775 cm^{-1} are already visible after deposit (Figure 4-24b) and become quite prominent after annealing the matrix to 30 K. They are marked by asterisks in Figure 4-24c. Further annealing to higher temperatures shows a sharp decrease in the absorption of monomeric HBr and a corresponding increase in the formation of oligomers, higher order complexes and aggregates. There are no bands attributed to the one-to-one complex observed in the higher frequency region (not shown). This fact is important and proves that the matrix isolated HBr:4-MP is a proton-shared complex. However, because the methyl substituent is more electropositive than Cl or H, the hydrogen-bonded proton is expected to be transferred to a greater extent towards the nitrogen.

Figure 4-24c shows many strong absorption bands arising from the HBr:4-MP complex over a large spectral region. While possible origins have been proposed in Section A for the multiple components of the HBr:pyridine complex, it is clear that the coupling of the hydrogen-bonded proton stretch with the methyl characteristic vibrations and the rest of the pyridine gives rise to a higher number of components and larger spectral coverage.

3. Theoretical Prediction and Force Field Treatment

The structure and the fundamental vibrations of the HBr:4-MP complex were computed at the MP2/6-31+G(d,p) level of theory in C_s symmetry. The distances between the three hydrogen-bonded atoms are strikingly similar to those of the

HBr:pyridine complex. At 2.959 Å, the intermolecular Br-N distance is only 0.001 Å longer than that of HBr:pyridine and the N-H distance is only 0.012 Å shorter (1.144 Å). These distances confirm, however, that the proton is slightly more transferred towards the nitrogen than for the unsubstituted complex, while the HBr:4-CP, also a 4-monosubstituted complex, exhibits a smaller transfer ($r_{\text{NH}} = 1.173$ Å, 0.017 Å longer than in HBr:pyridine).

The unmodified ab initio results for the HBr:4-MP complex are presented in the left column of Table 4-11 and the corresponding simulated spectrum is shown in Figure 4-25a. Considering that the strongest modes of HBr:pyridine are calculated to be (Table 4-2) at 1708 cm^{-1} (Q_6), 1561 cm^{-1} (Q_9 , the strongest) and 1533 cm^{-1} (Q_{10}), it is not surprising to see that these modes are also the most prominent in the case of HBr:4-MP. The higher proton affinity of 4-MP is expected to shift the local proton oscillator to a higher frequency, which explains why the mode Q_8 at 1737 cm^{-1} in Table 4-11 (equivalent to the mode Q_6 of HBr:pyridine) has a much greater intensity, almost equal to that of mode Q_{10} at 1659 cm^{-1} . While in both complexes the molar absorption coefficients are determined mainly by the contribution from the “NHs” and the “HBr” coordinates (see IDs of $Q_{6,\text{HBr:py}}$ and $Q_{8,\text{HBr:4-MP}}$), the N-H stretch is now the dominant contribution (38%) to the potential energy of mode $Q_{8,\text{HBr:4-MP}}$. The frequencies and PEDs of the modes $Q_{9,\text{HBr:py}}$ and $Q_{10,\text{HBr:4-MP}}$ are very similar but the intensity of the latter is decreased when compared to the HBr:pyridine complex and considering that both complexes have comparable total vibrational intensities. The mode $Q_{12,\text{HBr:4-MP}}$ at 1557 cm^{-1} , equivalent to $Q_{10,\text{HBr:py}}$, is farther away from the proton local oscillator and exhibits

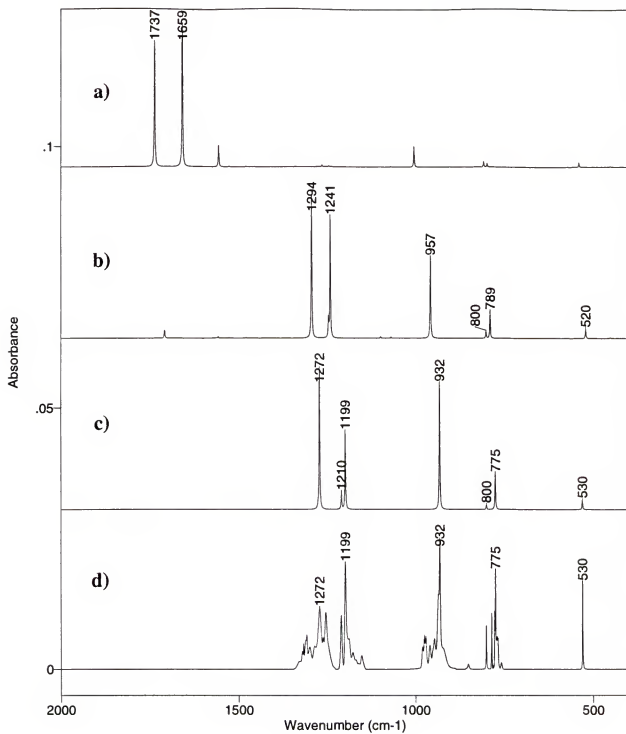


Figure 4-25. Infrared spectra for the HBr:4-MP complex: a) computed MP2/6-31+G(d,p); b) re-computed after force field treatment; c) experimental integrated intensity sum; and d) experimental extracted.

Table 4-11. Computed MP2/6-31+G(d,p) and re-computed^a frequencies (ν , cm^{-1}), intensities (A, km mol^{-1}), PEDs, and IDs (km mol^{-1}) for the HBr:4-MP complex. Comparison with experimental values^b given in brackets.

Original MP2/6-31+G(d,p)						Adjusted force field re-computed					
Q	ν	A	S_i	(PED)	[ID]	Q	ν	A	S_i	(PED)	[ID]
1	3293	5	4a C2H 5a C3H	(81+) (18+)	[7] [1]	1	3293	7	4a C2H 5a C3H	(81+) (18+)	[8] [1]
2	3291	0	32a" C2H 33a" C3H	(83+) (17+)	[0] [0]	2	3291	0	32a" C2H 33a" C3H	(83-) (17-)	[0] [0]
3	3275	2	33a" C3H 32a" C2H	(83-) (17+)	[1] [1]	3	3275	2	33a" C3H 32a" C2H	(83+) (17-)	[1] [1]
4	3274	0	5a C3H 4a C2H	(81+) (18-)	[0] [0]	4	3274	0	5a C3H 4a C2H	(81+) (18-)	[0] [0]
5	3231	6	38a" aMe	(100-)	[7]	5	3231	6	38a" aMe	(100+)	[7]
6	3210	6	23a Me o	(98-)	[6]	6	3210	6	23a Me o	(98+)	[6]
7	3121	8	11a sMe	(98+)	[9]	7	3121	8	11a sMe	(98-)	[9]
8	1737	2909	20a NHs 2a C2C3 1a NC 9a R2 19a HBrs	(38-) (22-) (13+) (10-) (-4-)	[1228] [-7] [190] [165] [1320]	8	1710	154	2a C2C3 3a C3C4 7a C2Hb 1a NC 9a R2 8a C3Hb 20a NHs 19a HBrs	(42-) (14+) (11-) (11+) (10-) (10+) (1-) (0-)	[-2] [14] [-22] [40] [41] [13] [45] [22]
9	1667	3	29a" CN 31a" C3C4 40a" NHBrb	(35-) (30+) (15-)	[4] [-1] [1]	9	1667	3	29a" CN 31a" C3C4 40a" NHBrb	(35-) (30+) (15-)	[4] [-1] [1]
10	1659	3251	20a NHs 2a C2C3 3a C3C4 19a HBrs	(57+) (21-) (11+) (-5+)	[1548] [6] [-53] [1865]	10	1563	8	7a C2Hb 8a C3Hb 3a C3C4 1a NC 20a NHs	(32+) (25+) (19+) (17-) (1+)	[-8] [-4] [-3] [10] [11]
11	1558	25	40a" NHBrb 42a" aMe s 34a" C2Hb 30a" C2C3 31a" C3C4	(25+) (21+) (15-) (13+) (11+)	[4] [7] [8] [10] [2]	11	1558	25	40a" NHBrb 42a" aMe s 34a" C2Hb 30a" C2C3 31a" C3C4	(25+) (21+) (15-) (13+) (11+)	[4] [7] [8] [10] [2]
12	1557	431	7a C2Hb 8a C3Hb 3a C3C4 1a NC 20a NHs 19a HBrs	(35+) (24+) (15+) (14-) (4-) (1+)	[58] [27] [21] [-67] [146] [234]	12	1527	9	24a Me sc	(90+)	[10]
13	1527	10	24a Me sc	(90-)	[8]	13	1519	0	42a" aMe s 34a" C2Hb	(67-) (10-)	[2] [-1]
14	1519	0	42a" aMe s 34a" C2Hb	(67+) (10+)	[2] [-1]	14	1480	11	30a" C2C3 31a" C3C4 29a" CN 40a" NHBrb	(37+) (22-) (18-) (11-)	[12] [-2] [-5] [-2]
15	1480	11	30a" C2C3 31a" C3C4 29a" CN 40a" NHBrb	(37+) (22-) (18-) (11-)	[12] [-2] [-5] [-2]	15	1480	11	30a" C2C3 31a" C3C4 29a" CN 40a" NHBrb	(37+) (22-) (18-) (11-)	[12] [-2] [-5] [-2]

Table 4-11 -- continued

Original MP2/6-31+G(d,p)						Adjusted force field re-computed					
Q	v	A	S _i	(PED)	[ID]	Q	v	A	S _i	(PED)	[ID]
16	1457	4	12a Me um	(93-)	[2]	15	1457	1	12a Me um	(93-)	[1]
17	1372	0	35a* C3Hb 34a* C2Hb 31a* C3C4	(50+) (16+) (12+)	[0] [0] [0]	16	1372	0	35a* C3Hb 34a* C2Hb 31a* C3C4	(50-) (16-) (12-)	[0] [0] [0]
18	1339	1	34a* C2Hb 40a* NHBrb 29a* CN	(39-) (35-) (29+)	[2] [-1] [1]	17	1339	1	34a* C2Hb 40a* NHBrb 29a* CN	(39-) (35-) (29+)	[2] [-1] [1]
20	1245	17	7a C2Hb 8a C3Hb 1a NC 2a C2C3	(42-) (30+) (13-) (11+)	[9] [-5] [8] [0]	19	1246 (1210)	307 295	7a C2Hb 2a C2C3 8a C3Hb 20a NHs 19a HBrs	(38+) (28-) (16-) (6+) (0+)	[-37] [1] [14] [162] [179]
19	1264	41	6a C4Me 2a C2C3 3a C3C4 8a C3Hb 20a NHs 19a HBrs	(42+) (17-) (11-) (10+) (1+) (0+)	[5] [0] [4] [-4] [17] [19]	20	1241 (1199)	2034 1274	20a NHs 6a C4Me 8a C3Hb 1a NC 19a HBrs	(29-) (20-) (15-) (15+) (-4-)	[884] [25] [-39] [103] [958]
21	1139	1	35a* C3Hb 30a* C2C3 34a* C2Hb	(35-) (31+) (15+)	[1] [-2] [1]	21	1139	1	35a* C3Hb 30a* C2C3 34a* C2Hb	(35-) (31+) (15+)	[1] [-2] [1]
22	1102	4	1a NC 8a C3Hb 10a R1 3a C3C4	(37+) (22+) (19+) (10-)	[-6] [-2] [0] [1]	22	1099	11	21a NHBrb 1a NC 10a R1 8a C3Hb 19a HBrs	(37+) (18-) (15-) (12-) (0+)	[3] [-7] [1] [-2] [11]
23	1099	5	21a NHBrb	(89+)	[8]	23	1098	18	21a NHBrb 1a NC 10a R1 19a HBrs	(53+) (13+) (12+) (0-)	[5] [-7] [1] [14]
24	1069	13	18a Me ro	(81+)	[5]	24	1069	19	18a Me ro	(81-)	[7]
25	1032	0	39a* Me ro 31a* C3C4	(70+) (13-)	[0] [0]	25	1032	0	39a* Me ro 31a* C3C4	(70+) (13-)	[0] [0]
26	1003	405	10a R1 1a NC 3a C3C4 2a C2C3 19a HBrs 20a NHs	(45-) (18+) (14+) (11+) (5-) (3+)	[-6] [-42] [-12] [-1] [315] [144]	26	957 (932)	1487 2121	10a R1 20a NHs 1a NC 3a C3C4 19a HBrs	(25+) (21-) (19-) (16-) (2+)	[-8] [608] [-78] [-22] [948]
27	941	0	25a* C2Hw 26a* C3Hw 27a* R3o	(74+) (41-) (-15+)	[0] [0] [0]	27	941	0	25a* C2Hw 26a* C3Hw 27a* R3o	(74+) (41-) (-15+)	[0] [0] [0]
28	903	1	13a C2Hw 14a C3Hw 16a R1o	(63+) (46-) (-10-)	[6] [-5] [-1]	28	903	1	13a C2Hw 14a C3Hw 16a R1o	(63-) (46+) (-10-)	[6] [-5] [-1]

Table 4-11 -- continued

Original MP2/6-31+G(d,p)							Adjusted force field re-computed						
Q	v	A	S _i	(PED)	[ID]		Q	v	A	S _i	(PED)	[ID]	
29	877	0	26a* C3Hw 25a* C2Hw	(67+) (34+)	[0] [0]		29	877	0	26a* C3Hw 25a* C2Hw	(67+) (34+)	[0] [0]	
30	807	114	6a C4Me 3a C3C4 10a R1 14a C3Hw 9a R2 19a HBrs 20a NHs	(24+) (22+) (14+) (12-) (11+) (2+) (0-)	[-3] [6] [-1] [7] [-18] [85] [36]		30	800 (800)	134 (87)	14a C3Hw 13a C2Hw 20a NHs 19a HBrs 17a R2o	(47-) (35-) (1-) (0+) (-6-)	[29] [33] [32] [55] [-20]	
31	797	75	14a C3Hw 13a C2Hw 19a HBrs 22a BrHw 17a R2o	(43+) (32+) (1+) (1-) (-6+)	[28] [30] [22] [11] [-19]		31	789 (775)	436 (738)	6a C4Me 3a C3C4 10a R1 20a NHs 19a HBrs	(26+) (20+) (19+) (6-) (1+)	[-8] [11] [-3] [172] [303]	
32	670	0	37a* R3	(87-)	[0]		32	670	0	37a* R3	(87-)	[0]	
33	572	3	16a R1o	(92+)	[8]		33	572	3	16a R1o	(92-)	[8]	
34	538	93	9a R2 19a HBrs 6a C4Me 20a NHs	(61+) (17+) (14-) (-4+)	[-24] [94] [2] [21]		34	520 (530)	175 (175)	9a R2 6a C4Me 19a HBrs 20a NHs	(69-) (13+) (10-) (-2-)	[-33] [2] [156] [52]	
35	450	12	15a C4Mew 17a R2o	(58+) (45+)	[0] [23]		35	450	12	15a C4Mew 17a R2o	(58+) (45+)	[0] [24]	
36	387	0	27a* R3o	(115-)	[0]		36	387	0	27a* R3o	(115+)	[0]	
37	346	0	36a* C4Meb	(84-)	[0]		37	346	0	36a* C4Meb	(84-)	[0]	
38	239	1	17a R2o 22a BrHw 16a R1o 15a C4Mew	(33-) (24-) (23-) (20+)	[-3] [2] [1] [0]		38	239	1	17a R2o 22a BrHw 16a R1o 15a C4Mew	(32+) (24+) (24-) (20-)	[-3] [2] [1] [0]	
39	198	43	19a HBrs 9a R2	(82-) (13+)	[40] [3]		39	147	53	19a HBrs	(94-)	[50]	
40	71	1	22a BrHw 17a R2o	(70-) (28+)	[1] [1]		40	71	1	22a BrHw 17a R2o	(70-) (28+)	[1] [1]	
41	62	0	28a* Me to	(99-)	[0]		41	62	0	28a* Me to	(99-)	[0]	
42	45	3	41a* BrHb	(98+)	[3]		42	45	3	41a* BrHb	(98+)	[3]	

a) Re-computed with scale factors $\alpha_{\text{HBrs}} = 0.508$ and $\alpha_{\text{NHs}} = 0.508$ (see text). Note that a better agreement with the experiment was obtained, in terms of frequency, with $\alpha_{\text{HBrs}} = 0.50$ and $\alpha_{\text{NHs}} = 0.45$ (but with a greater discrepancy in the intensity pattern).

b) Experimental data are assigned based on the re-computed results.

a reduced participation of the proton stretch coordinates to the intensity and to the potential energy.

The multiple components of the strong absorption regions visible in the experimental extracted spectrum (Figure 4-25d) are summed in Figure 4-25c to simplify and clarify the comparison with the calculated spectra. It is clearly not possible to make a direct band-by-band assignment of the intensity sum spectrum (Figure 4-25c) from the original computed spectrum (Figure 4-25a). Again, it seems likely that the neglect of anharmonicity in the calculation is responsible for the difference between the calculated and the experimental spectrum, although there may also be some effect due to the environment.

In order to adjust the harmonic force constants to account for the anharmonicity of the hydrogen-bonded proton stretching local coordinate, the diagonal and off-diagonal symmetry force constants involving the "HBrs" and "NHs" coordinates were scaled before solving the secular equation (see Section B-6 of this chapter). The search on the scale factors α_{HBrs} and α_{NHs} was initiated with the value 0.45 for both, corresponding to $(v_{\text{exp}}/v_{\text{har}})^2$, where v_{exp} and v_{har} are the intensity average frequencies of the experimental and ab initio strong absorptions respectively. Better agreement with the experimental results was finally obtained with $\alpha_{\text{HBrs}} = \alpha_{\text{NHs}} = 0.508$. Note that these factors are very close to those used in the HBr:pyridine complex treatment (0.52 for both α_{HBrs} and α_{NHs}).

The re-computed results are presented in the right column of Table 4-11 and the corresponding spectrum is shown in Figure 4-25b. The agreement between the experimental intensity sum and the re-computed spectra is remarkable considering the simplicity of the scaling. The assignment of the strong experimental bands is now

possible (see values in brackets, Table 4-11). The interaction of the modes Q_{17} and Q_{18} of 4-MP (Table 4-10) with the Br-H and N-H stretch vibrations gives rise to the three intense modes Q_{18} , Q_{19} and Q_{20} at 1294, 1246 and 1241 cm^{-1} (Table 4-11). Their intensities arise mostly from the proton stretch coordinates as revealed by the IDs. The “HBrs” coordinate has no (or negative) contribution to the potential energy, which confirms the proton transfer. An interesting remark can be made concerning the mode Q_{22} and Q_{23} at 1099 and 1098 cm^{-1} . These almost degenerate vibrations allow the mixing of the NHB linear bend and HBr stretch coordinates, which is normally forbidden in C_{2v} symmetry. However, the contribution from the “HBrs” coordinates appears only in terms of intensity.

E. The HBr:3,5-dimethylpyridine Complex

1. Infrared Spectra and Analysis of 3,5-dimethylpyridine

The spectra of 3,5-dimethylpyridine (3,5-DMP) obtained in argon matrix, in the gas phase at 300 K and in the solid at 10 K are presented in Figures 4-26 for the lower spectral region (450 - 1700 cm^{-1}). Since 3,5-DMP is liquid at room temperature, the experimental procedure employed here was similar to that described for pyridine in Section A-1. No ab initio calculation was made for 3,5-DMP. The assignment given in Table 4-12 is based mostly on those for other substituted pyridines, in particular 4-MP and 3,5-DCP, and on a computational treatment explained below.

The calculation reported in Table 4-12 has been made using the DFT B3LYP/6-31G(d,p) ab initio force field for pyridine and treating the methyl groups as point masses of 15 a.m.u. Since the symmetry force constants for the stretchings,

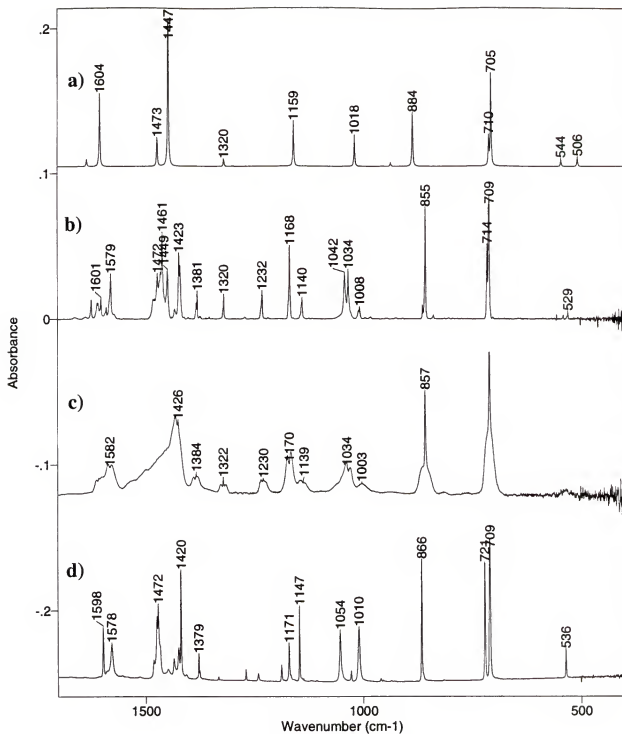


Figure 4-26. Infrared spectra of 3,5-dimethylpyridine in the region from 1700 to 400 cm^{-1} . a) From imported force field calculation (see text). b) Isolated in an argon matrix at 10 K (baseline corrected). c) Gas phase at 300 K. d) Solid crystal at 10 K after annealing to 210 K.

Table 4-12. Observed vibrational frequencies (cm^{-1}) of 3,5-dimethylpyridine from Ar matrix at 10K, gas phase at 300K, solid crystal at 10K, and tentative assignment from imported force field calculation^{a)}. Intensities A^{b)} given in km/mol.

Ar Matrix		Gas	Cryst.	Imported force field calculation					
v	A	v	v	Q	v	A	S ₁	(PED)	[ID]
3021	24	3028 ^{c)}	3024	1	3079	12	6a1 C4H	(100+)	[10]
3017			3014	2	3052	11	4a1 C2H	(100+)	[8]
				3	3048	44	22b2 C2H	(100+)	[37]
2981	20	2990 ^{c)}		Methyl asym. str. (aMe)					
2967	14	2963 ^{c)}							
2936	12	2936 ^{c)}	2916	Methyl sym. str. (sMe)					
2871	6	2879 ^{c)}	2871	Methyl out-of-plane str. (Me o)					
1610	2			4	1633	1	21b2 C3C4	(45-)	[2]
1601	3	1608 ^{c)}	1598				19b2 CN	(14+)	[2]
1589	2		1588				26b2 C4Hb	(13+)	[-1]
1579	5	1582B	1579	5	1604	14	2a1 C2C3	(50+)	[4]
							7a1 C2Hb	(16+)	[-5]
							1a1 NC	(11-)	[6]
1461	17		1568	6	1472	6	3a1 C3C4	(43-)	[0]
							7a1 C2Hb	(27-)	[3]
							8a1 C3Me	(11-)	[2]
							5a1 C3Me	(10+)	[1]
1483	7		1482	Methyl asym. def. (Me sc)					
1472	7		1475	(overlap with mode Q6)					
1465			1472						
1449	7		1450						
1434	1		1436	7	1447	34	20b2 C2C3	(33-)	[13]
1423	11	1425A	1425				19b2 CN	(28-)	[10]
1420			1420				24b2 C2Hb	(17-)	[3]
1384				Methyl sym. def. (Me um)					
1381	2	1384A	1379	8	1319	1	24b2 C2Hb	(68-)	[-1]
1320	2	1322A	1334				26b2 C4Hb	(24-)	[1]
1272	0		1271	9	1299	0	5a1 C3Me	(38+)	[0]
							7a1 C2Hb	(32+)	[0]
							10a1 R1	(14+)	[0]
1232	3	1230A	1242	10	1269	0	19b2 CN	(49+)	[0]
							20b2 C2C3	(30-)	[0]
							21b2 C3C4	(18+)	[0]
1168	6	1170B	1172	12	1159	9	1a1 NC	(69-)	[7]
							7a1 C2Hb	(22-)	[2]
1140	2	1139	1148	Methyl rock (Me ro)					
1042	8		1054	13	1018	6	10a1 R1	(61+)	[4]
1034	6	1034B	1028				3a1 C3C4	(18+)	[0]
							2a1 C2C3	(16+)	[1]

Table 4-12 -- continued

Ar Matrix		Gas	Cryst.	Imported force field calculation					
v	A	v	v	Q	v	A	S _j	(PED)	[ID]
1008	2	1003	1010						
924	0			16	935	1	16b1 C4Hw 14b1 C2Hw	(71-) (37+)	[3] [-3]
862	0								
855	9	857C	865	17	884	12	14b1 C2Hw 16b1 C4Hw 15b1 C3Mew 17b1 R1o	(70+) (35+) (12-) (-18-)	[15] [8] [-4] [-10]
837	0								
714	6		721	18	710	5	9a1 R2 2a1 C2C3 5a1 C3Me 10a1 R1	(31-) (23+) (22+) (14-)	[4] [-1] [0] [1]
709	12	710C		19	705	18	17b1 R1o	(118-)	[17]
539	0	537	536	20	544	1	25b2 C3Meb 27b2 R3	(72+) (20-)	[0] [0]
529	0			23	506	2	9a1 R2 5a1 C3Me 3a1 C3C4	(58+) (23+) (10+)	[2] [0] [0]

- a) Computed with force constants imported from pyridine and 4-methylpyridine and by treating the methyl groups as point masses of 15 a.m.u. (see text). Calculated modes that are not observed in experiment are not reported in this table.
- b) Absolute intensities arbitrarily obtained by matching the intensity of the experimental methyl umbrella mode of 3,5-dimethylpyridine at 1381 cm⁻¹ with that of 4-methylpyridine at 1380 cm⁻¹.
- c) Gas phase band center uncertain due to multiple band overlaps.

bendings and waggings of C₃-Me (and C₅-Me) are different than for C₃-H (and C₅-H), the values for these constants were imported from the MP2/6-31+G(d,p) force field of 4-MP. The three diagonal constants for the C₄Me, C₄Meb and C₄Mew coordinates in 4-MP (see Appendix C, Table C-2) were used to replace the six diagonal symmetry force constants: a1 C₃H, b2 C₃H, a1 C₃Hb, b2 C₃Hb, a2 C₃Hw and b1 C₃Hw (Appendix C, Table C-1). Since there is little difference between the force constants associated with the symmetric and asymmetric stretchings (a1 C₃H and b2 C₃H), the same values were set for both constants. The same applies for the symmetric and asymmetric bendings and waggings. Table 4-13 presents the changes made to the force field of pyridine in order to obtain that of “pseudo” 3,5-DMP.

Table 4-13: Diagonal force constants (mdyn Å) involving the C₃-H bond (and C₅-H) of pyridine and values used in the “pseudo” 3,5-DMP force field.

Coordinate S	F _{ss} pyridine DFT	F _{ss} “pseudo” 3,5-DMP
5a1 C ₃ H/C ₃ Me (sym. s)	5.618E+00	5.022E+00
8a1 C ₃ Hb/C ₃ Meb (sym. b)	5.341E-01	8.108E-01
12a2 C ₃ Hw/C ₃ Mew (asym. w)	4.611E-01	4.587E-01
15b1 C ₃ Hw/C ₃ Mew (sym. w)	4.764E-01	4.587E-01
23b2 C ₃ H/C ₃ Me (asym. s)	5.617E+00	5.022E+00
25b2 C ₃ Hb/C ₃ Meb (asym. b)	5.095E-01	8.108E-01

Two remarks must be made concerning the results of the computational treatment, partially presented in Table 4-12. Since the “pseudo” force field for 3,5-DMP is based on the force field of pyridine with the changes shown in Table 4-13, the solutions of the secular equation will yield $(3 \times 11 - 6) = 27$ modes of vibration instead of the $(3 \times 17 - 6) = 45$ expected for 3,5-DMP. More specifically, all 18 of the methyl group characteristic vibrations are missing.

The second important remark is that the polar tensor used to calculate the intensities is the unchanged polar tensor of pyridine. Therefore, one should not rely too much on the calculated intensities presented in Table 4-12. For this reason, the experimental intensities were arbitrarily converted to absolute values by matching the intensity of the methyl umbrella mode around 1380 cm^{-1} in both 3,5-DMP and 4-MP.

There appear to be only two previous studies published on 3,5-DMP. Comparison with the most recent, a Raman gas phase study from Draeger,¹²⁵ is not straightforward because some of the strongest modes in infrared are weak or inactive in Raman. For instance, the strong absorption observed at 855 cm^{-1} in Figure 4-26b is not observed in the Raman spectrum¹²⁵ and several others are also missing. A more complete and helpful study was made by Green *et al.*¹²⁶ with Raman and infrared results in the liquid phase. The assignment proposed in Table 4-12 is in good agreement with their results and the Raman information helped confirm some of the vibrational symmetry assignments.

By observation of the gas phase band contours in Figure 4-26c (also reported in Table 4-12), it appears that the correlation between the symmetries and the band contours is similar to that of 3,5-DCP, i.e., bands with contour A, B and C have b_2 , a_1 , and b_1 symmetry respectively. In fact, the correlation was used to assign some of the uncertain fundamentals. For instance, the vibration observed at 1170 cm^{-1} in Figure 4-26c was assigned to the a_1 mode Q_{12} based on its well-defined contour B. In references (125, 126), this band was attributed to an asymmetrical b_2 vibration.

The methyl scissors region, between 1400 and 1500 cm^{-1} , shows many overlapping bands, visible in the three experimental spectra. Two in-plane symmetric and asymmetric ring deformations (mode Q_6 and Q_7) are also found in this region.

Except for the symmetric methyl deformation (umbrella mode), the methyl group characteristic vibrations are significantly affected by the intermolecular interactions of the solid, as reflected by the changes in the methyl rock ($\sim 1000\text{ cm}^{-1}$) and scissors ($\sim 1400\text{ cm}^{-1}$) regions, between the solid and the matrix isolated spectra. These two spectra were recorded at 10 K. The solid was warmed to 210 K and cooled back down to 10 K to sharpen the extremely broad absorptions typical of the amorphous phase. While the gas phase and the matrix spectra have similar intensity patterns, the solid spectrum exhibits a quite different one, particularly noticeable in the region between 1000 and 1400 cm^{-1} .

2. Infrared Spectra of the HBr:3,5-DMP Complex

The 3,5-dimethylpyridinium bromide was prepared by mixing at $5\text{ }^{\circ}\text{C}$ equimolar quantities of 3,5-DMP (Aldrich, 98% purity) with concentrated hydrobromic acid. After evaporation to dryness in vacuum, the resulting residue was dried over P_2O_5 and sublimed under vacuum to give colorless crystals. No CAS registry number was found for this salt. Sublimation at room temperature of 3,5-dimethylpyridinium bromide was insufficient to deposit HBr and 3,5-DMP in the matrix at an acceptable rate. Thus, the salt was heated to about $50\text{ }^{\circ}\text{C}$.

The spectra of the 3,5-DMP isolated in argon and of the mixture Ar/HBr/3,5-DMP before and after annealing (30 K) is shown in Figure 4-27. It was not possible to estimate the concentration of the complex because no ab initio computation was performed. The molar absorption coefficients required to evaluate its concentration were not available. The HBr absorption region around 2550 cm^{-1} (not shown) revealed virtually no trace of HBr dimer before annealing. It is therefore likely that the concentrations of the different species were comparable to those obtained for the other complexes studied in this work.

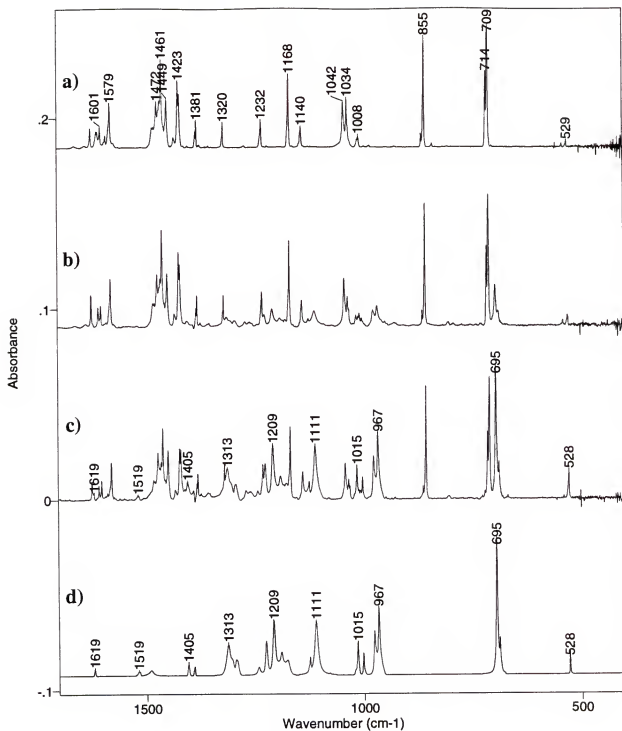


Figure 4-27. Experimental infrared matrix spectra, after baseline correction, in the region from 1700 to 400 cm^{-1} for: (a) 3,5-DMP + Ar; (b) HBr + 3,5-DMP + Ar before annealing; (c) HBr + 3,5-DMP + Ar after annealing; (d) the HBr:3,5-DMP complex extracted from (c). For greater clarity, frequency labels are not shown in (b) and only bands of the complex are labelled in (c).

Table 4-14. Observed vibrational frequencies (cm^{-1}) and relative intensities I_R for the HBr:3,5-DMP complex isolated in an Ar matrix at 10 K after annealing to 30 K. Bands are grouped by absorption regions, and the relative intensity is reported for each region. Asterisks identify the most intense band of each region.

Ar Matrix		Equivalent mode number from the HBr:4-MP complex ^a
ν	I_R	
1619*	0.009	
1519*	0.014	
1491*	0.039	
1405*	0.037	
1391		
1313*	0.295	
1295		
1243	0.695	Q18
1226		
1209*		
1191		
1177		
1125	0.360	Q20
1111*		
1015*	0.110	
1002		
977	0.158	Q26
967*		
695*	0.395	Q31
688		
527*	0.021	Q34

a) Possible mode equivalences from the adjusted force field re-computed results for the HBr:4-MP complex (right column of Table 4-11).

There was no new band attributed to the HBr:3,5-DMP complex after annealing in the higher spectral region. Figure 4-27d represents the extracted spectrum of the one-to-one complex whose absorptions are growing approximately by a factor of three after annealing. Notice that most of the complex bands are clearly visible before annealing (Figure 4-27b). The strong absorptions arising from the complex are spread over a wide spectral region, and the presence of two methyl groups is certainly related to the high number of components. Nearby components are regrouped into absorption regions and are listed, with the relative intensity of each region, in Table 4-14. No accurate assignment was possible for this complex, but it is safe to assume that the intensity of the bands of the complex originates primarily from the hydrogen-bonded proton stretch, coupled with different vibrations of 3,5-DMP. By comparing the spectrum of the HBr:3,5-DMP complex (Figure 4-27d) with that of the HBr:4-MP complex (Figure 4-25d), it is possible to find resemblances for some absorption regions. For possible equivalent regions, the mode numbers from the adjusted force field computation for the HBr:4-MP complex are reported in Table 4-14.

CHAPTER V COMPARISONS AND TRENDS

A. Matrix Effect on the Complex

The ideal study of an individual complex should be conducted in the gas phase in order to avoid any environmental disturbance. Since, at the present time, this is not practically feasible, it is important to know whether the matrix perturbation significantly affects the vibrational levels of the complex and, thus, significantly shifts the vibrational frequencies from their gas phase values. As mentioned in Chapter 4, this could be particularly critical for hydrogen-bonded complexes suspected to be on the verge of proton transfer, like the HBr:3,5-DCP complex for instance.

Several inert gases (argon, krypton and nitrogen) were used as matrix material to assess their effect on the frequency and intensity of bands arising from the one-to-one complex. It has been shown²⁰ that the smallest matrix shifts occur for neon matrices, with increasing matrix shifts for the heavier rare gases and even larger shifts for nitrogen. Due to the temperature limitation of our helium closed-cycle refrigeration system (~ 10 K), it was not possible to condense neon matrices.

Figure 5-1 presents, in the region from 1300 to 500 cm^{-1} , the spectra after annealing of three different mixtures: HBr/pyridine/Ar, HBr/pyridine/Kr and HBr/pyridine/N₂ respectively. Only the absorptions attributed to the one-to-one HBr:pyridine complex are labeled with their frequencies. These often include nearby components belonging to the complex that are not labeled, for greater clarity. When

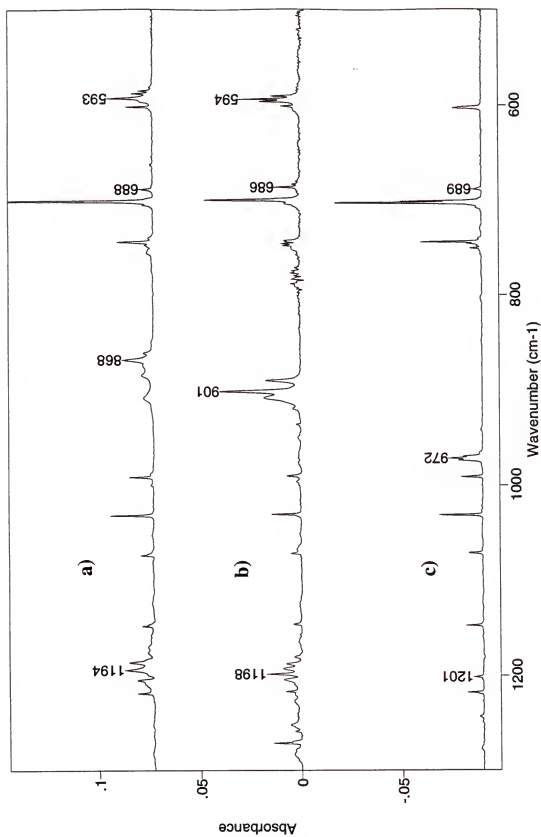


Figure 5-1. Infrared spectra of the HBr:pyridine complex isolated in different matrices in the region from 1300 to 500 cm⁻¹. a) Argon matrix. b) Nitrogen matrix. c) Krypton matrix.

comparing the three spectra visually, bands arising from the pyridine monomer (not labeled) do not appear to be affected by the type of matrix material employed.

Observation of the complex bands in the argon and krypton matrices (Figure 5-1a and 5-1b) reveals that the three regions of strong absorption, at 1194, 868 and 593 cm^{-1} in argon matrix, are virtually unchanged in the more interacting krypton matrix (1198, 901 and 594 cm^{-1}). Note that the absorption region reported at 868 cm^{-1} in argon extends upward to 908 cm^{-1} , while that reported at 901 cm^{-1} in krypton extends downward to 889 cm^{-1} . Hence, the HBr:pyridine complex does not appear to be very sensitive to the small perturbation of the environment from an Ar to a Kr matrix. It seems possible that the frequencies of the strong absorptions in these two matrices could be close to the unknown gas phase values.

The results for the nitrogen matrix (Figure 5-1c) are quite different. The absorption region around 593 cm^{-1} in the argon matrix is completely missing in the nitrogen matrix. The band at 1200 cm^{-1} has a very low intensity relative to the strong band at 972 cm^{-1} which appears to be related to the band at 868 cm^{-1} from the argon matrix results. Nitrogen often interacts strongly with solutes in low-temperature matrices. Barnes *et al.*³¹ have shown that samples studied in argon matrices doped with 1% nitrogen can display shifts similar to those observed in pure nitrogen matrix, proving that there is a specific interaction with nitrogen. Our results for the HBr: NH_3 complex¹²⁷ indicated that the strongest band, arising from the proton stretch coordinate and observed at 729 cm^{-1} in an argon matrix, was shifted to 1390 cm^{-1} in a nitrogen matrix.

Figure 5-2 presents similar results for the HBr:4-CP complex. The three regions of strong absorption at 1180, 913 and 685 cm^{-1} in argon matrix (Figure 5-2a) appear at

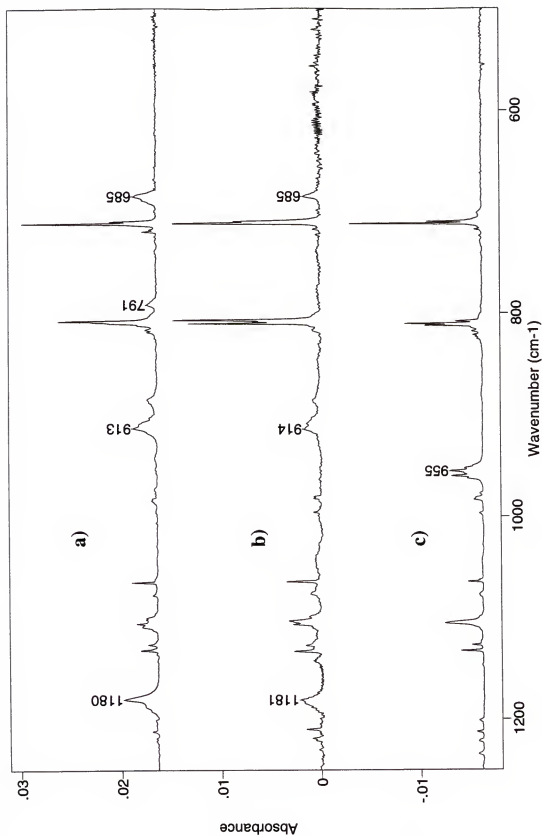


Figure 5-2. Infrared spectra of the HBr:4-CP complex isolated in different matrices in the region from 1250 to 500 cm⁻¹. a) Argon matrix. b) Krypton matrix. c) Nitrogen matrix.

1181, 914 and 685 cm^{-1} , respectively, in krypton matrix (Figure 5-2b). Again, the matrix effect due to the small perturbation from Ar to Kr appears to be very small for the HBr:4-CP complex, suggesting that the matrix perturbation from the gas phase may also be small. One small difference exists, however, for the weaker band at 791 cm^{-1} which is present in argon but not in krypton. The re-computed frequencies and intensities given in Table 4-9 do not predict a strong fundamental vibration of the complex in this region, and its assignment is tentative. The strong absorptions at 1180 and 685 cm^{-1} in the argon matrix are absent in the nitrogen matrix (Figure 5-2c). Only one strong absorption region appears in that matrix at 955 cm^{-1} , probably related to the absorption at 913 cm^{-1} in the Ar matrix.

According to MP2/6-31+G(d,p) calculations, both HBr:pyridine and HBr:4-CP have their hydrogen-bonded proton already transferred towards the pyridine nitrogen (see Chapter 4, Sections A and C). However, the proton in HBr:3,5-DCP is on the brink of transfer but with the proton still close to the bromine atom (Chapter 4, Section B). Thus, it may be possible that a small perturbation could significantly affect the vibrational levels of this complex. Figure 5-3 shows the spectra of the HBr:3,5-DCP complex in argon, krypton and nitrogen matrices. The strong absorptions at 784 and 741 cm^{-1} in the argon matrix are shifted to 729 and 650 cm^{-1} in the krypton matrix, the latter being the most intense. Since the Br-H distance is expected to increase if the more interacting krypton matrix stabilizes the proton transferred form, the observed shift of the strongest bands of the complex to lower frequency proves experimentally that the hydrogen-bonded proton is closer to the bromine atom, confirming the *ab initio* geometry.¹⁰⁵ The HBr:3,5-DCP complex is the only complex of the HBr series studied in this work for

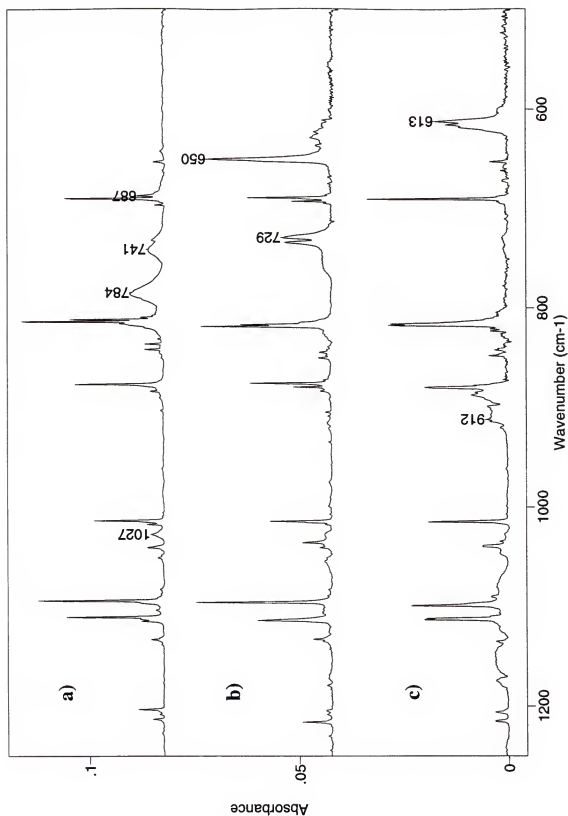


Figure 5-3. Infrared spectra of the HBr:3,5-DCP complex isolated in different matrices in the region from 1250 to 500 cm⁻¹. a) Argon matrix. b) Krypton matrix. c) Nitrogen matrix.

which the proton is not transferred towards the nitrogen. More electronegative substituents on the pyridine, for example 2,6-difluoropyridine (2,6-DFP), are expected to produce complexes with traditional hydrogen bonds, but their weak binding energies with HBr did not allow the synthesis of ionic salts. These bases are too weak and study of their complexes would require the use of a dual jet deposition method.

Because all three matrices perturb differently the potential surface of the HBr:3,5-DCP complex (as shown by the different frequencies of the strong absorptions in all three spectra, Figure 5-3), it is reasonable to expect a neon matrix to produce a different spectrum with the strong bands of the complex shifted to higher frequencies. The gas phase results for this complex would also be expected to be different than that obtained in an argon matrix.

The transfer of the hydrogen-bonded proton in the HBr:4-MP, HBr:3,5-DMP and HBr:2,4,6-trimethylpyridine (HBr:2,4,6-TMP, not presented in Chapter 4) complexes is expected to be more towards the N atom than in the HBr:pyridine complex. Thus, the perturbation of the argon matrix is not expected to be significant for these complexes.

B. The Proton Stretch Local Oscillator

It is apparent, from the PED and ID contributions (Chapter 4), that the strongest transitions of the complex owe their intensity to the proton stretch local oscillator. The intensity is distributed over several modes of the complex that would be too weak to be observed if they did not couple with this local oscillator. In order to obtain the approximate frequency of this local oscillator, an averaging procedure was carried out over all the observed absorption bands for the complex. Using the experimental frequencies and intensities, this intensity weighted average frequency is expressed as:

$$\bar{\nu}_{\text{osc}} = \frac{\sum_{\text{all bands}} \left(\nu_s \int_s \ln \left(\frac{I_0}{I} \right) dv \right)}{\sum_{\text{all bands}} \int_s \ln \left(\frac{I_0}{I} \right) dv}, \quad (5-1)$$

where ν_s is the frequency of the s^{th} band and the integral is the corresponding measured integrated intensity defined in Chapter 2. Figure 5-4 presents the extracted experimental spectra of the 1:1 complexes, trapped in Ar matrices, of HBr with substituted pyridines of increasing basicity, and for each, the frequency of the proton stretch local oscillator $\bar{\nu}_{\text{osc}}$. The figure clearly shows the increase in frequency of $\bar{\nu}_{\text{osc}}$ as the basicity increases, reflecting a deepening of the potential well on the side of the nitrogen. This trend can also be visualized by correlating the frequency of the local oscillator with the proton affinity of each substituted pyridine (see Figure 5-5).

Because the proton affinities of 3,5-DCP and 2,4,6-TMP were not available from published data, their values were estimated as follows. The proton affinity is the negative of the enthalpy change of the reaction at 298 K: base + proton \rightarrow ion, defined as:

$$\Delta H = \Delta E(\text{electronic}) + \Delta E(\text{zero - point vibrational}) + \Delta E(\text{thermal vibrational}) + \Delta E(\text{rotational}) + \Delta E(\text{translational}) + \Delta nRT \quad (5-2)$$

where the rotational, translational and work terms are evaluated classically. The other terms can be obtained from ab initio calculations. The logfiles of 3,5-DCP and of 3,5-dichloropyridinium provide $\Delta E(\text{elect.}) = -218.4$ kcal/mol, $\Delta E(\text{z-p vib.}) = 8.6$ kcal/mol and $\Delta E(\text{therm. vib.}) = 0.1$ kcal/mol. With $\Delta E(\text{rot.}) = 0$, $\Delta E(\text{trans.}) = -0.89$ kcal/mol and $\Delta nRT = -0.59$ kcal/mol, one finds $\text{PA}(3,5\text{-DCP}) = 211.2$ kcal/mol.

In the case of 2,4,6-TMP, no experimental or calculated values were available. Instead, the change in proton affinity from methylamine ($\text{NH}_2(\text{CH}_3)$) to trimethylamine

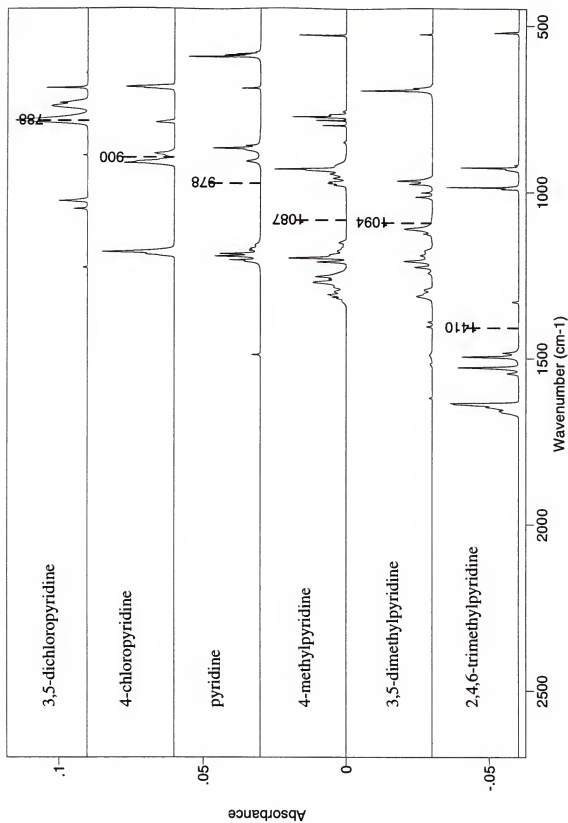


Figure 5-4. Extracted infrared spectra (from Ar matrices) for the HBr series of complexes with substituted pyridines. Each dashed line represent the frequency of the proton stretch local oscillator $\bar{\nu}_{sec}$. The proton affinity of the base increases from top to bottom.

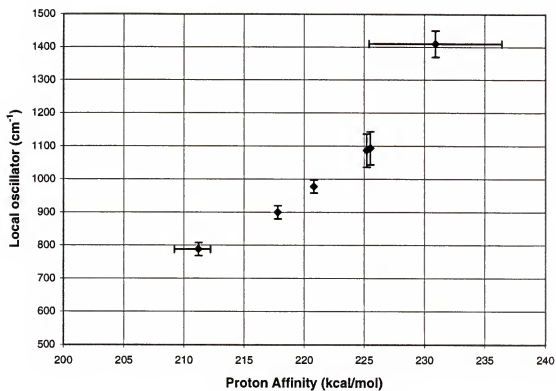


Figure 5-5. Frequencies of the proton stretch local oscillator $\bar{\nu}_{\text{osc}}$ for the HBr series of complexes versus the proton affinity of substituted pyridines.

(N(CH₃)₃) was used as an upper limit for the change in proton affinity from methylpyridine (4-MP) to trimethylpyridine (2,4,6-TMP). This difference (11.0 kcal/mol) provides an upper limit of 225.2 + 11.0 = 236.2 kcal/mol. The proton affinity of 2,4,6-TMP lies between that of 3,5-DMP (225.5 kcal/mol) and 236.2 kcal/mol, the mid-point being at 230.9 kcal/mol. Error bars are represented accordingly in Figure 5-5. Notice in this figure that since the hydrogen-bonded proton of HBr:3,5-DCP is not yet transferred, there should be a minimum frequency for $\bar{\nu}_{\text{osc}}$ between 3,5-DCP and 4-CP.

Additional results for substituted pyridine complexes with HCl¹²⁸ allow us to further extend the trend of proton transfer towards the traditional hydrogen bonds. The frequencies of the local oscillators $\bar{\nu}_{\text{osc}}$ are represented for the HBr and HCl series in Figure 5-6. Some properties for these complexes are reported in Table 5-1. Note that although the hydrogen-bonded proton of HCl:4-MP is less transferred than that of HBr:3,5-DCP, $\bar{\nu}_{\text{osc}}(\text{HCl:4-MP})$ is slightly lower than $\bar{\nu}_{\text{osc}}(\text{HBr:3,5-DCP})$. The vibrational correlation diagram, introduced by Ault *et al.*,¹²⁹ correlates the relative frequency shift of the hydrogen halide with the normalized proton affinity (PA) difference:

$$\Delta = \frac{\text{PA}(\text{A}^-) - \text{PA}(\text{B})}{\text{PA}(\text{A}^-) + \text{PA}(\text{B})}, \quad (5-3)$$

where A⁻ is the halide ion (here, Cl⁻ or Br⁻) and B is the base. The relative frequency shift $\Delta\nu/\nu_0$ is defined by $(\bar{\nu}_{\text{osc}} - \nu_0) / \nu_0$, where ν_0 is vibrational frequency of the free hydrogen halide ($\nu_0(\text{HCl}) = 2885 \text{ cm}^{-1}$ and $\nu_0(\text{HBr}) = 2559 \text{ cm}^{-1}$). Figure 5-7 shows the correlation diagram for the complexes presented in Table 5-1. This correlation does not resemble very closely Ault-Pimentel plots in the literature.^{31,129} The scale of variables is much expanded and the complexes studied here are all close to the region of proton transfer, as

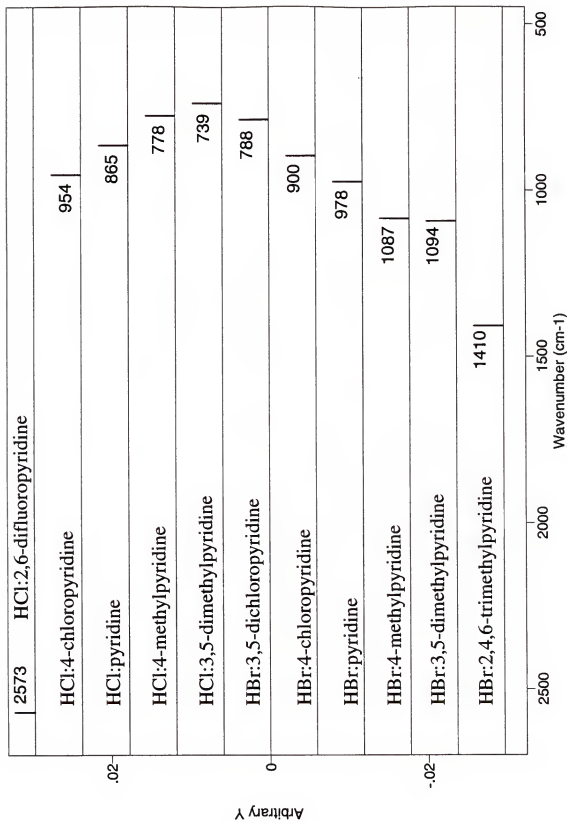


Figure 5-6. Spectral position of the proton stretch local oscillator $\bar{\nu}_{\text{osc}}$ for the HCl and HBr series of complexes with substituted pyridines.

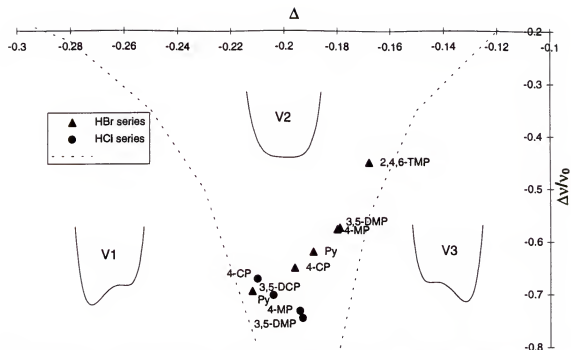


Figure 5-7. Vibrational correlation diagram for the HCl and HBr series of complexes with substituted pyridines, and the three potential curves (along the proton stretching coordinate) corresponding to the three types of hydrogen bond: V1 = traditional, V2 = proton shared, V3 = ionic.

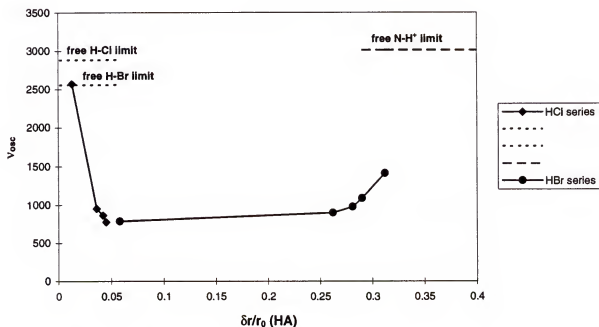


Figure 5-8. Experimental frequencies of the proton stretch local oscillator $\bar{\nu}_{osc}$ versus normalized A-H distances $\delta r/r_0$ for the HCl and HBr series of complexes with substituted pyridines (where A = Cl or Br).

opposed to the plots for traditional complexes. The correlation is much more subtle than suggested and needs further study.

Table 5-1: Selected properties of complexes of HCl and HBr with substituted pyridines.

Complex ^a	PA(B) ^b	PA(A) ^c	Δ^d	r_{A-H} (Å)	r_{N-H} (Å)	$\delta r/r_0^e$	$\bar{\nu}_{osc}^f$
HCl:2,6-DFP		333.7		1.286	2.020	0.013	2573
HCl:4-CP	217.8	333.7	-0.210	1.316	1.758	0.036	954
HCl:pyridine	220.8	333.7	-0.204	1.323	1.721	0.042	865
HCl:4-MP	225.2	333.7	-0.194	1.327	1.703	0.045	778
HCl:3,5-DMP	225.5	333.7	-0.193				739
HBr:3,5-DCP	211.2 ^g	323.9	-0.214	1.489	1.605	0.058	788
HBr:4-CP	217.8	323.9	-0.196	1.775	1.173	0.262	900
HBr:pyridine	220.8	323.9	-0.189	1.802	1.156	0.281	978
HBr:4-MP	225.2	323.9	-0.180	1.815	1.144	0.290	1087
HBr:3,5-DMP	225.5	323.9	-0.179				1094
HBr:2,4,6-TMP	230.9 ^g	323.9	-0.168	1.85 ^h	1.13 ^h	0.31 ^h	1410

^a DFP = difluoropyridine, CP = chloropyridine, DCP = dichloropyridine, MP = methylpyridine, DMP = dimethylpyridine, TMP = trimethylpyridine.

^b Proton affinity of the substituted pyridines in kcal/mol. Unless otherwise noted, all values are from reference (130).

^c Proton affinity (kcal/mol) of the halide anions (A = Cl or Br) are from reference (131).

^d Normalized proton affinity difference (see text).

^e Normalized H-A distance change (see text).

^f Frequency of the proton stretch local oscillator in cm^{-1} .

^g No published data available for this estimated value (see text).

^h Because the estimated proton affinity of HBr:2,4,6-TMP lies approximately between that of HBr:pyridine (220.0 kcal/mol) and HBr:4-Lithiumpyridine (computed at 246.6 kcal/mol), the Br-H distance was estimated by taking the mid-point between the Br-H distance of HBr:pyridine and that of HBr:4-Lithiumpyridine.¹⁰³ Same for the N-H distance.

While ab initio frequencies of proton shared complexes are not predicted very accurately (mostly due to the harmonic approximation), computed distances are expected to be much closer to actual distances for isolated complexes, as revealed by the comparison of the calculated Br-N interatomic distances with some gas phase data for several complexes with amines obtained by microwave spectroscopy.¹³²⁻¹³⁶ Thus, the

normalized distance change $\delta r/r_0$ can be used to correlate with the experimental local oscillator $\bar{\nu}_{\text{osc}}$ (Figure 5-8). Here, r_0 is the interatomic distance for the free hydrogen halide ($r_0(\text{HCl}) = 1.270 \text{ \AA}$, $r_0(\text{HBr}) = 1.407 \text{ \AA}$) and δr is the A-H distance in the complex minus r_0 . The frequency limit marked "free N-H⁺" in Figure 5-8 is that estimated for the totally transferred proton. Its value (around 3000 cm^{-1}) was taken from the experimental absorption of the N-H⁺ stretching vibration of the solid pyridinium bromide. Of course, there should normally be a different value of this limit for each substituted pyridine.

Examination of Figure 5-8 shows that the frequency $\bar{\nu}_{\text{osc}}$ of the HCl series of complexes decreases steadily as the proton approaches the proton-shared region. The HBr series of complexes shows a decrease in frequency as the normalized distance $\delta r/r_0$ decreases, from the proton-transferred to the proton-shared region. This series is not represented correctly in Figure 5-8 because the first two points (HBr:3,5-DCP and HBr:4-CP) should not be connected by a straight line. Indeed, there exists a minimum for $\bar{\nu}_{\text{osc}}$ between these two points.

C. Force Constants

1. Effect of the Scale Factors on the Spectrum

The purpose of scaling the force constants involving the Br-H and N-H stretching coordinates (and all the corresponding coupling constants) is not only to bring the frequency of the computed proton stretch local oscillator (LOp) closer to the experimental one, but also to allow the coupling of this oscillator with lower frequency local modes of the substituted pyridine. Thus, it is interesting to vary systematically the values of the

scale factors (α_{HBr} and α_{NH}) to sweep through a wide range of possible couplings and to observe the changes in frequency and intensity of different modes of the complex.

The effect of the scale factors on the spectrum of the HBr:4-MP complex is visualized, using a 3D perspective, in Figure 5-9 from 0 to 1700 cm^{-1} . Each spectrum was obtained by solving the secular determinant after scaling the Br-H and N-H symmetry force constants by the same factor, i.e., $\alpha_{\text{HBr}} = \alpha_{\text{NH}}$, and using the Pulay's scaling method introduced in Chapter 4, Section B-6. The rearmost spectrum in Figure 5-9, with scale factors $\alpha_{\text{HBr}} = \alpha_{\text{NH}} = 1$, corresponds to the ab initio spectrum (no change of the force field) of the HBr:4-MP complex as shown already in Figure 4-24a. By reducing the scale factors α_{HBr} and α_{NH} , the "BrHs" and "NHs" force constants and, therefore the frequency of the LOp, are reduced. As the frequency of the LOp decreases, different couplings with other local oscillators of the same symmetry (e.g., CH bending modes or ring vibrations of 4-MP) are revealed in Figure 5-9. Observation of the fundamental vibration Q_8 around 1700 cm^{-1} (far left of Figure 5-9) shows that its intensity decreases dramatically as the LOp moves to lower frequencies. While this intensity change is greater than 95% over the range of scale factors presented, the change in frequency (of mode Q_8) is less than 5%. It is also apparent from this figure that some of the modes of the complex exhibit significant coupling with the LOp even when the two oscillators are relatively far apart, while others couple only when the LOp comes very close in frequency.

The apparent "exchange" of intensity between the LOp and a mode of the HBr:4-MP complex is shown with an expanded scale for the region around 1200 cm^{-1} (Figure 5-10). As the LOp (band A) "moves" closer to the mode around 1260 cm^{-1} (Band

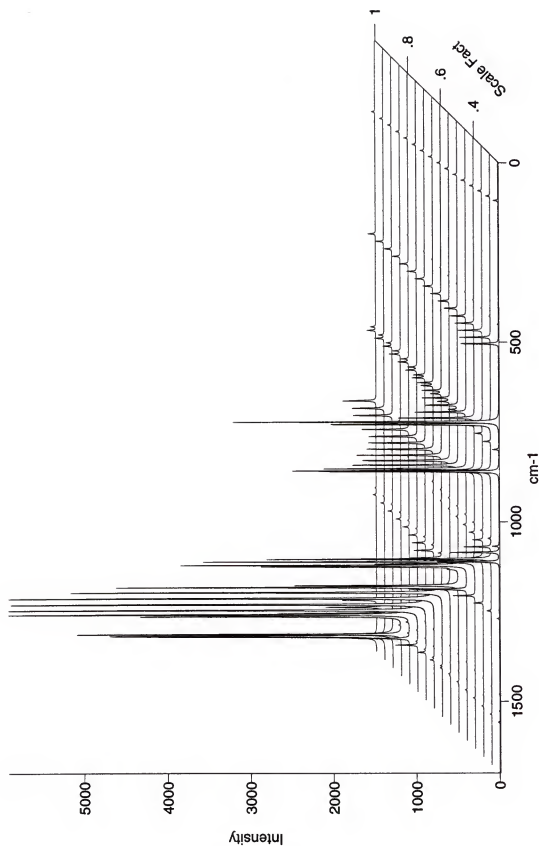


Figure 5-9. 3-D representation of the effect of the scale factors α_{HBr} and α_{NH_3} on the computed spectrum of the HBr:4-MP complex (from 1700 to 0 cm^{-1}). A scaling was applied to the force field with $1 > \alpha > 0.25$ and $\alpha_{\text{HBr}} = \alpha_{\text{NH}_3} = \alpha$.

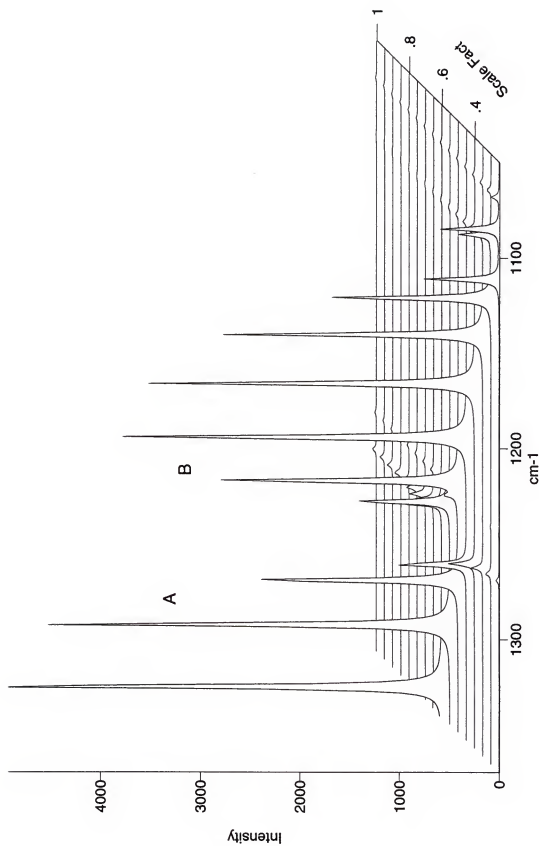


Figure 5-10. Details of Figure 5-9 in the region from 1370 to 1050 cm^{-1} . The change in coupling between band A and band B reveal the apparent "exchange" of intensity.

B = mode Q_{19} of Table 4-11), the potential energy of the LOP is altered by the increasing contribution from the symmetry coordinates involved in the mode Q_{19} . This contribution exchange can be seen in Figure 5-10 with the rapid change of “frequency direction” of band A, which stabilizes around 1260 cm^{-1} for scale factors below 0.4. At that point, band A is not the LOP anymore but almost the pure mode Q_{19} . Figure 5-11 plots the PED contribution from three symmetry coordinates (“HBrs”, “NHs” and “C4Me”) versus the scale factor α (Pulay’s scaling with $\alpha_{\text{HBrs}} = \alpha_{\text{NHs}}$) for bands A and B to better illustrate the PED contribution exchange. Because the intensity of bands A and B arises mostly from the coordinates “HBrs” and “NHs”, the intensity will appear to “exchange”.

In the trend discussed above, α_{HBrs} was assumed to be equal to α_{NHs} . Figure 5-12 presents two trends in the $1050 - 1370\text{ cm}^{-1}$ region where the scale factors are adjusted independently. The first trend (Figure 5-12a) shows the effect on the spectrum of the HBr:4-MP complex of varying the α_{NHs} scale factor from 0.41 to 0.49 and fixing α_{HBrs} to 0.50. In the second trend (Figure 5-12b), the scale factor α_{HBrs} is adjusted from 0.46 to 0.54 and α_{NHs} is fixed at 0.45. Clearly, the two scale factors do not have the same influence on the spectrum. The fact that the hydrogen-bonded proton of the HBr:4-MP complex is significantly transferred towards the nitrogen explains why scaling the N-H stretching force constant has much more influence on the frequency of the LOP (and on the intensity of other modes that couple with the LOP) than scaling the H-Br stretching force constant.

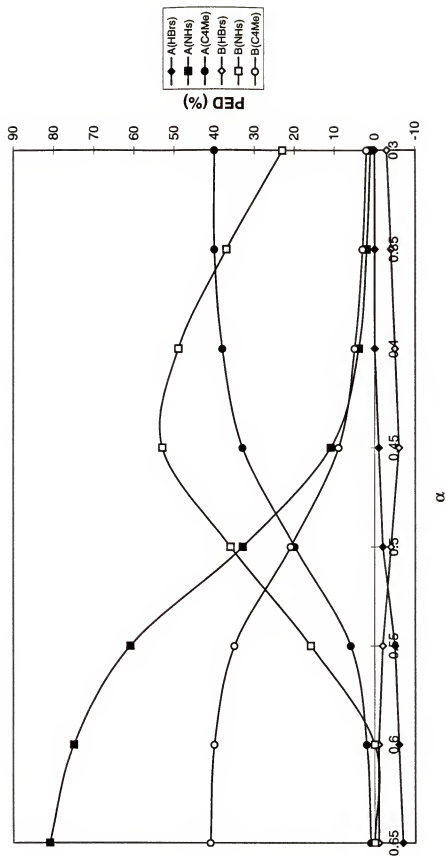


Figure 5-11. PED (%) contributions to modes A and B (presented in Figure 5-9) from the symmetry coordinates "HBr", "NH", and "C4Me" versus the scale factor α .

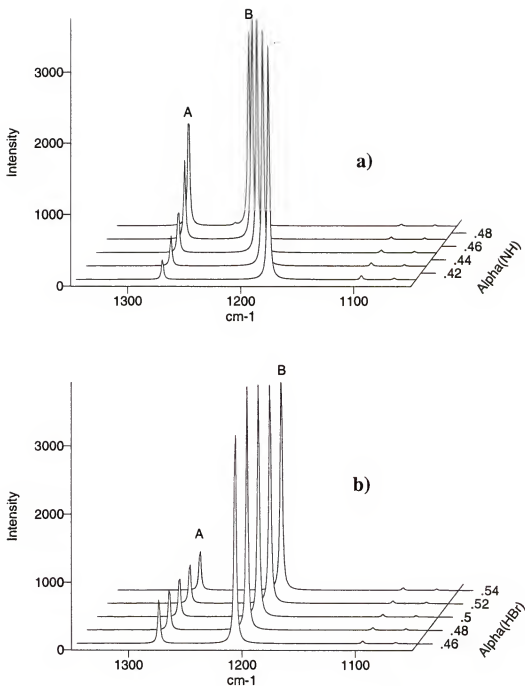


Figure 5-12. Effect of independently varying the scale factors α_{HBr} and α_{NHs} on the spectrum of the HBr:4-MP complex (from 1370 to 1050 cm^{-1}). a) $\alpha_{\text{HBr}} = 0.50$ and $0.49 > \alpha_{\text{NHs}} > 0.41$. b) $0.54 > \alpha_{\text{HBr}} > 0.46$ and $\alpha_{\text{NHs}} = 0.45$.

2. Force Constants of the Proton Stretch Local Oscillator

There are only a limited number of complexes of HBr with substituted pyridines for which both ab initio and experimental data are available. The empirical force constants of four of these complexes, obtained using the Xtrapack program, are presented in this section. Reported in Table 5-2 are the proton affinities of the substituted pyridines, the electronic binding energies of the hydrogen bonded complexes, the harmonic symmetry force constants for the H-Br and the N-H stretching coordinates, their off diagonal coupling constants, the scale factors α_{HBr} and α_{NH} , and the corresponding scaled or “anharmonic” symmetry force constants.

Table 5-2: Force constants of the proton stretch local oscillator for the complexes of HBr with substituted pyridines.

	HBr:3,5-DCP	HBr:4-CP	HBr:Pyridine	HBr:4-MP
PA (kcal/mol)	209.6	217.8	220.8	225.2
ΔE_e^a (kcal/mol)	11.7	14.1	15.7	17.7
$k(\text{HBr}, \text{HBr})$ ($\text{aJ}/\text{\AA}^2$)	2.851	1.250	1.182	1.148
$k(\text{NH}, \text{NH})$ ($\text{aJ}/\text{\AA}^2$)	0.329	2.204	2.480	2.700
$k(\text{HBr}, \text{NH})$ ($\text{aJ}/\text{\AA}^2$)	0.803	1.269	1.227	1.21
α_{HBr}	0.30	0.35	0.45	0.50
α_{NH}	0.67	0.55	0.47	0.45
$k_s(\text{HBr}, \text{HBr})$ ($\text{aJ}/\text{\AA}^2$)	0.855	0.437	0.532	0.574
$k_s(\text{NH}, \text{NH})$ ($\text{aJ}/\text{\AA}^2$)	0.221	1.212	1.166	1.215
$k_s(\text{HBr}, \text{NH})$ ($\text{aJ}/\text{\AA}^2$)	0.360	0.557	0.564	0.574

^a Electronic binding energy of the complex relative to HBr and the substituted pyridine.

The “anharmonic” force constants are simply the ab initio force constants multiplied by the appropriate scale factor. They are estimates of effective force constants that would fit the experimental spectra, although large errors are possible due to significant uncertainties in evaluating the scale factors. The data in Table 5-2 show that for all the complexes the harmonic force constant $k(\text{HBr}, \text{HBr})$ decreases and the force

constant $k(\text{NHs}, \text{NHs})$ increases as the proton affinity of the substituted pyridine increases. This is not true for the “anharmonic” force constants. Figure 5-13 illustrates graphically the variation in diagonal force constants of the LOP as a function of the normalized distance change $\delta r/r_0$ (given in Table 5-1) for the complexes presented in Table 5-2. The non-normalized Y-axis gives a better view of the difference between the harmonic and “anharmonic” force constants. The range of values for both harmonic force constants is much greater than that for the “anharmonic” force constants. It is also possible to plot the scale factors against the normalized distance change $\delta r/r_0$ (Figure 5-14). This figure shows that in the harmonic approximation the force constants are indiscriminately overestimated and that different scale factors should be used to reduce the force constants involving the H-Br and N-H stretching coordinates.

Figure 5-15 plots the change in normalized force constants $-\delta k/k_0$ for the H-Br and N-H stretching force constants versus the proton affinity of the substituted pyridine. For the H-Br stretch, the quantity δk is the difference between the force constant for the H-Br stretch in the complex and the force constant (k_0) for the isolated HBr molecule. The same definition applies for the force constant for the N-H stretch. The two curves corresponding to the harmonic force constants cross at $-\delta k/k_0$ around 0.7 while their “anharmonic” homologues cross substantially higher at $-\delta k_s/k_{s0}$ around 0.85. Note that the force constant k_{s0} for HBr was obtained by scaling the ab initio force constant k_0 so that the computed frequency matched the experimental one ($k_{0(\text{HBr})} = 4.375 \text{ aJ/\AA}^2$ and $k_{s0(\text{HBr})} = 3.850 \text{ aJ/\AA}^2$). The approximation made for the force constant k_{s0} for the N-H stretch was greater for two reasons. First, the scaling of the ab initio force constant k_0 was carried out so that the computed N-H stretch vibrational frequency for the pyridinium

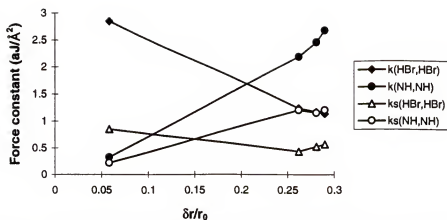


Figure 5-13. Diagonal symmetry force constants of the LOP for the HBr series of complexes with substituted pyridines versus the normalized distance change $\delta r/r_0$. Both ab initio (k) and scaled (ks) force constants are plotted.

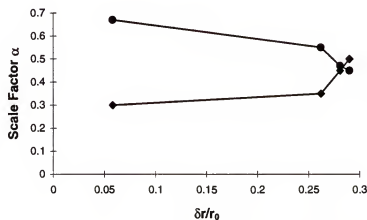


Figure 5-14. Scale factors for the HBr series of complexes with substituted pyridines versus the normalized distance change $\delta r/r_0$.

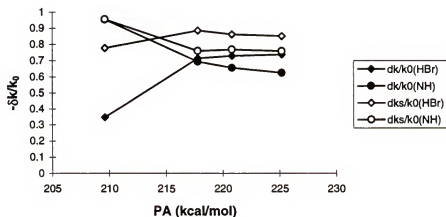


Figure 5-15. Normalized H-Br force constant changes $-\delta k/k_0$ versus the proton affinity of the substituted pyridines.

ion matched that of the experimental pyridinium bromide for which the hydrogen bonded-proton is fully transferred ($k_{0(\text{NH})} = 7.194 \text{ aJ/\AA}^2$ and $k_{s0(\text{NH})} = 5.040 \text{ aJ/\AA}^2$). Second, the computed and experimental N-H stretch characteristic vibration depends on the proton affinity of the nitrogen base. Hence, different values of k_0 and k_{s0} should have been used for each substituted pyridine.

3. Harmonic Coincidental Match

It has been shown thus far that the harmonic force constants associated with the proton stretching motion needed some adjustment in order to account for the anharmonicity. In rare cases, however, the experimental frequency $\bar{\nu}_{\text{osc}}$ matches the calculated harmonic frequency. This implies that the energy difference between the first two vibrational levels, fitted to the “anharmonic” potential, is the same as for the harmonic potential at the point of minimum energy. An indication of how such a coincidental match may occur is shown in model calculations for a series of complexes of HCl with substituted amines.¹³⁷ Figure 5-16 presents energy cross-section curves of the HCl:ammonia, HCl:methylamine, HCl:dimethylamine and HCl:trimethylamine complexes calculated at fixed N-X distances with varying H-X distance, together with the corresponding computed harmonic frequencies and the experimental frequencies. Each “anharmonic” energy cross-section curve was obtained from a series of single point calculations (at the University of Florida) at the MP2/6-31+G(d,p) level of theory by plotting the MP2 energies. All atoms of the complex were fixed in position, except the hydrogen-bonded proton which was incrementally displaced along the N-Cl axis. The curve thus obtained is not a potential energy curve for proton motion, but it still indicates

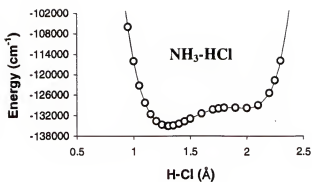
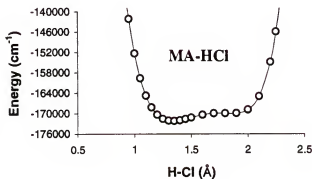
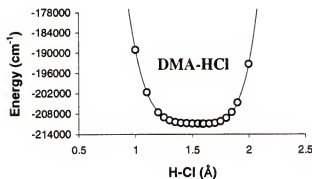
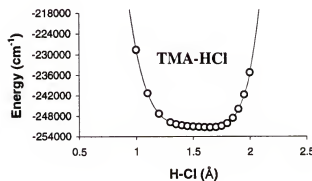
Exp. 1194 cm⁻¹Harm. 2541 cm⁻¹Exp. 765 cm⁻¹Harm. 2157 cm⁻¹Exp. 842 cm⁻¹Harm. 753 cm⁻¹Exp. 1019 cm⁻¹Harm. 1366 cm⁻¹

Figure 5-16. Approximate potential curves for the HCl series of complexes with ammonia, methylamine, dimethylamine, and trimethylamine. The computed harmonic frequency and the experimental frequency of the LOP are given for each complex.

the approximate change in shape of the anharmonic potential along the proton stretching motion.

Figure 5-16 shows that these energy cross-section curves (and presumably also the potential energies for the proton stretching motion) change systematically as the strength of interaction with HCl increases from NH_3 to $\text{N}(\text{CH}_3)_3$. It suggests that there may be complexes in which the energy at the “shoulder” becomes the same as the energy at the equilibrium, and a smooth, broad potential, with a minimum at the equilibrium geometry, occurs. For such a curve the Gaussian program may well fit a harmonic potential that is very similar to the true potential energy curve, so that the calculated harmonic frequency from Gaussian would be the same as the calculated anharmonic frequency, and both would agree with the experiment.

CHAPTER VI CONCLUSION

The results presented in this work reveal that the vibrational frequencies of monomeric molecules of pyridine, 3,5-DCP, 4-CP, 4-MP and 3,5-DMP trapped in argon matrices are not significantly perturbed by the environment, compared with the vapor phase results. For instance, the vibrational frequencies of matrix isolated pyridine are well within 1% of those for gaseous pyridine (300 K) but with a vibrational spectrum much less complicated by rotational transitions. In the solid phase, where the environment is more interacting, the intensity pattern may be affected but the vibrational frequencies of these species remain within 3% of the gas phase values.

The low temperature (10 K) spectra of hydrogen-bonded complexes of HBr with substituted pyridines acquired in the crystal phase and isolated in matrix strongly suggest that different types of hydrogen bonds exist in these two phases. For most of the complexes presented in this work, infrared absorptions associated with the hydrogen-bonded proton stretch are in the $700 - 1200\text{ cm}^{-1}$ region for complexes isolated in Ar matrix and around 3000 cm^{-1} when self-associated in the solid phase. These results seriously contradict the belief of some crystallographers that for strong hydrogen bonds, "...crystal field forces are relatively weak and of almost no influence."^(8,p17) The dramatic frequency shift of about 2000 cm^{-1} between the isolated complex and the crystalline salt reflects important structural changes. In the solid phase, the hydrogen bonds for these

complexes are good examples of the ion pair $\text{Br} \cdots \text{H-N}$. Thus, because low temperature gas phase studies of strongly hydrogen bonded complexes are not practical, the matrix isolation technique is the best approach one can use to simulate a perturbation free environment.

The normalized frequency shift, from the free HBr monomer vibration to the antisymmetric $\text{Br} \cdots \text{H} \cdots \text{N}$ stretching vibration of the matrix isolated complex, is greater than 55% for the entire HBr series of complexes presented in this work, with the exception of the HBr:2,4,6-TMP complex, for which the normalized shift is only 45%. However, the hydrogen-bonded proton of these complexes is transferred towards the nitrogen. Thus, one should consider the normalized frequency shift from the free N-H stretch of pyridinium ion ($\sim 3100 \text{ cm}^{-1}$) which is greater than 50% for all complexes studied here. These facts are an experimental proof that the complexes of HBr with substituted pyridines are all proton shared hydrogen bonds $\text{Br} \cdots \text{H} \cdots \text{N}$. The frequency increase of the hydrogen-bonded proton stretch local oscillator (LOp) as a function of the increasing proton affinity of the substituted pyridine indicates that all but the HBr:3,5-DCP complex are proton shared with the hydrogen-bonded proton already transferred towards the nitrogen. The calculation predicts, and the experiment confirms, that the hydrogen bond in HBr:3,5-DCP is a proton shared with the proton closer to the Br atom than to the N atom. These experimental results are consistent with the *ab initio* MP2/6.31+G(d,p) predictions for the geometry of the HBr:3,5-DCP, HBr:4-CP, HBr:pyridine and HBr:4-MP complexes. However, the computed simulated spectra present severe differences with the experimental spectra, both in the frequency position and in the intensity pattern of the infrared bands of the complexes (an observation that is

valid for virtually all proton shared hydrogen-bonded complexes). The most significant factor which may be responsible for the discrepancy is the fact that the calculations by the Gaussian program of the vibrational spectrum are made under the assumption that all vibrations are harmonic. The force constants for these harmonic modes are obtained in Gaussian from the second derivatives of the potential energy at the point of minimum energy. The resulting calculated harmonic frequencies are usually much too large (with rare exceptions when the curvature of the potential energy at the minimum is very small).

The force field treatments applied in Chapter 4 reveal that scaling only the ab initio symmetry force constants of the LOp (i.e., the N-H and the H-Br stretching constants and their couplings) it is possible not only to lower the frequency of the LOp but also to achieve correct mixing with other modes of the substituted pyridine. Indeed, when the frequency of the LOp falls in the same spectral region as do the local normal vibrations of the substituted pyridine, the motion of the LOp involves the coordinated motion of the Br, H and N atoms, mixed with the motions of atoms of the substituted pyridine. These mixings account for the presence of several strong bands in the spectrum associated with the proton stretching motion. The relatively good agreement between the experimental and re-computed spectra suggests that, except for the N-H and the H-Br stretching constants, the ab initio force constants of the complex are calculated reasonably well.

The analysis of the computed spectra in Xtrapack by decomposing each mode of vibration into internal motion clearly shows that the major contributions to the intensity of the strongest bands are from the N-H and the H-Br stretching symmetry coordinates. The intensity of these strong bands can be up to 6000 km/mol for the series of complexes

studied here. The weaker modes are usually not detectable in the matrix because the concentration of the complex is very low. Small variations in scaling of the N-H and the H-Br stretching force constants strongly suggest that small changes due to a slight distortion of the potential surface can have a dramatic impact on the intensities, with only negligible changes in the frequencies.

Comparison of the *ab initio* and scaled force constants for the proton stretching motions emphasizes that the former are too high and that the difference between the N-H and H-Br stretching force constants is also too high. This is probably a direct consequence of the harmonic approximation used to calculate the vibrational frequencies. The *ab initio* calculation appears to exaggerate the degree of proton transfer (either towards Br or N) not in terms of interatomic distances but in terms of force constants and frequencies. The HBr:3,5-DCP and HBr:4-CP complexes are good examples of this problem. It is clear that in order to better simulate and predict the different spectral properties of proton shared hydrogen bonded complexes, a better knowledge of their potential energy surface is required.

APPENDIX A FORTRAN FLOW-CHART DIAGRAM

Xtrapack is a multi-language program with a user interface written in Visual Basic (MS VB5.0) and a computation intensive routine written in Fortran (MS Fortran90). The Fortran code is compiled as a dynamic link library (DLL) and the two languages communicate through a set external variables (arguments, EV).

The user interface is an event-driven application where the code is executed in response to an event, such as a click from the mouse, instead of following lines of codes in a specific order. An event driven selector (EDS) waits for an action from the user in order to execute the code in the associated event procedure. Because most of the scientifically relevant procedures of Xtrapack are written in Fortran, the flow-chart of the Visual Basic part is not presented here. The symbols used in the flow-chart diagram, Figure A-1, are reported in Table A-1. The arguments used in the calling convention between the Visual Basic and the Fortran are given in Table A-2.

Table A-1. Symbols and dimensions for the vectors and matrices used in Figure A-1. The question mark “?” refers to the dimension of the internal coordinates vector, a user-defined parameter.

Symbols	Description
A	$(3N) \times (3N - 6)$ “Inverse” of B
B	$(3N - 6) \times (3N)$ Transformation $S = B X = U B_R X$
B_R	$(?) \times (3N)$ Transformation $R = B_R X$
C	Eigenvectors of H
D	Eigenvectors of G
EDS	Event driven selector
EV	External Variable (argument)
F	Force constants matrix
F_R	$(?) \times (?)$ Force constants in internal coordinates
F_S	$(3N - 6) \times (3N - 6)$ Force constants in symmetry coordinates
F_X	$(3N \times 3N)$ Force constants in cartesian coordinates
G	$(3N - 6) \times (3N - 6)$ Kinetic energy
H	$(3N - 6) \times (3N - 6)$ Hamiltonian
ID	Intensity distribution
L	Eigenvectors of $(G F_S)$, transformation $S = L Q$
M	$(3N) \times (3N)$ Masses
N	$(3N - 6)$ Vector of the normalization factors of the cartesian displacements
P_O	Polar tensor (dipole derivatives) in normal coordinates
P_S	Polar tensor (dipole derivatives) in symmetry coordinates
P_X	Polar tensor (dipole derivatives) in cartesian coordinates
PED	Potential energy distribution
Q	$(3N - 6)$ Normal coordinates vectors
R	$(?)$ Internal coordinates vectors
RID	RAMAN intensity distribution
S	$(3N - 6)$ Symmetry coordinates vectors
Sc	$(3N - 6) \times (3N - 6)$ Scaling factors matrix (for direct product)
T	Eigenvalues of G
U	$(3N - 6) \times ?$ Transformation $S = U R$
W	Notation simplification of $(D T^{1/2})$
X	$(3N)$ Cartesian coordinates vectors (Gaussian's Z-matrix orientation)
ΔX	Atomic displacements in cartesian coordinates
Λ	Eigenvalues of H and $(G F_S)$

Table A-2. Calling convention between Visual Basic and Fortran with the names of the external variables, their Fortran type, and their description.

VB 5.0	Fortran	Type	Description
PckPath	PCKFN	(string*120)	file name and path
CfcPath	CFCFN	(string*120)	file name and path
PxzPath	PXZFN	(string*120)	file name and path
SymPath	SYMFN	(string*120)	file name and path
IntPath	INTFN	(string*120)	file name and path
OutPath	OUTPUTFN	(string*120)	output file name and path
OutputTitle	TITLE	(string*65)	output file title
FCChoice	FCCHOICE	(integer*4)	1 = save F_S to file 2 = save F_R to file 3 = save both 0 = save none
FSymExist	FSEXIST	(integer*4)	1 = F_S exists as file 2 = F_S exists as double array 0 = F_S doesn't exist
ForcePass	FPASS	(integer*4)	2 = Pass to export F_S in VB 1 = Regular run
NSymmetry	NSYM	(integer*4)	number of symmetry (3N - 6)
RamanInt	IRAMAN	(integer*4)	2 = save Raman intensities 1 = don't save
MinPED	IMIN	(integer*4)	PED threshold (0 - 100)
MaxSym	JMAX	(integer*4)	Maximum number of symmetry printed out (0 - NSYM)
FConstSgl2DArr	FSYMSGL	(real*4)	F_S
FScalSgl2DArr	FSCAL	(real*4)	Sc
DispChoice	CDCHOICE	(integer*4)	1 = save cartesian displacements 0 = don't save

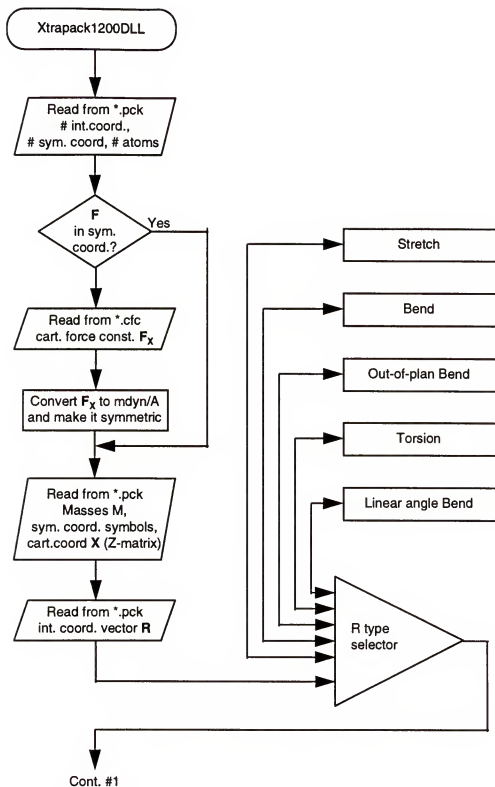


Figure A-1. Flow chart diagram of the dynamic link library Xtrapack1200DLL written in Fortran.

Figure A-1 -- continued

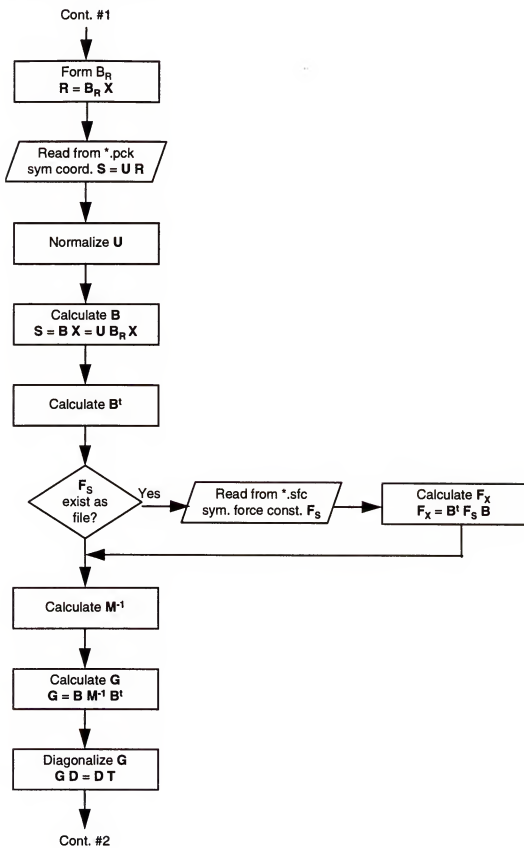


Figure A-1 -- continued

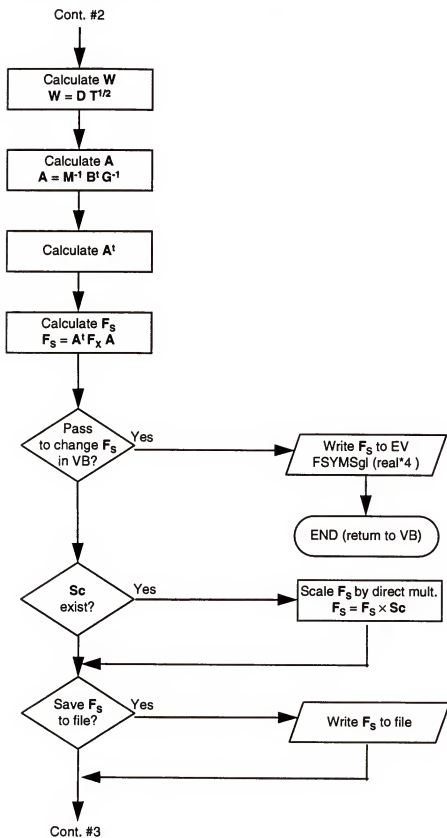


Figure A-1 -- continued

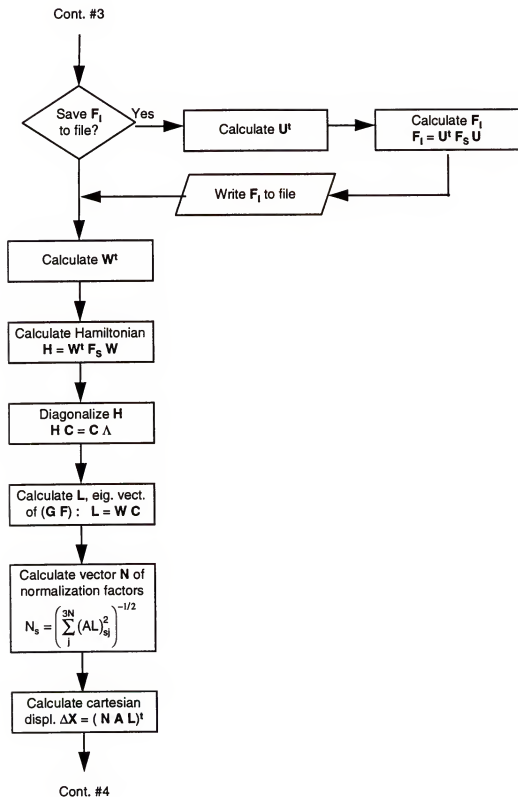


Figure A-1 -- continued

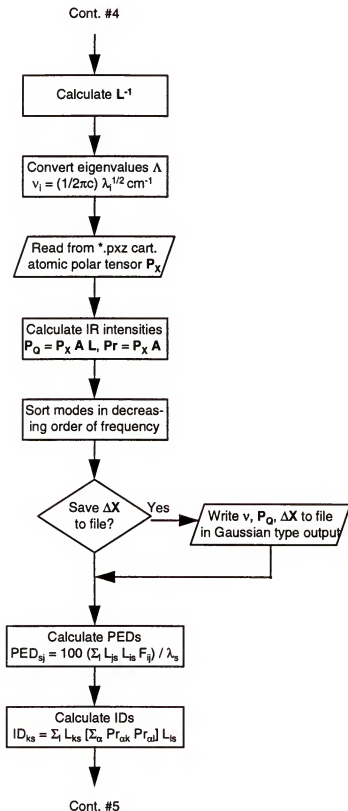
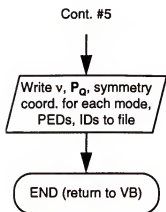


Figure A-1 -- continued



APPENDIX B CONSTRUCTING THE INPUT FILES FOR XTRAPACK

Input Files Generated by Xtrapack

The Xtrapack program requires at least three input files in order to compute the solutions of the secular equation and to present the “dissection” of the fundamental vibrations into meaningful molecular coordinates. The first file contains the Cartesian force constants matrix \mathbf{F}_X in the Z-matrix orientation, exactly as it appear in the Gaussian logfile. This file can be extracted automatically by Xtrapack and saved under a *.cfc file.

The second file contains the dipole derivative tensor necessary to calculate the infrared intensities. For some Gaussian calculations made at the Hartree-Fock (HF) level, it may also contain the polarizability derivative tensor required to calculate the Raman intensities. The dipole derivative elements are read from the archive of the Gaussian logfile, rearranged into a tensor form and saved as a *.pxz file automatically.

Coordinate Input File

The third and most important file is the *.pck file. It contains the definitions of the internal coordinates (often a redundant set of coordinates) and the symmetry coordinates (a non-redundant set of coordinates). Internal coordinates can be defined in many ways and different users may define them differently.

Symmetry coordinates, which are linear combinations of internal coordinates, need to be constructed by the user. In the following, the construction of a *.pck file will be presented for the $\text{HBr}:\text{NH}_3$ complex (C_{3v} point group). The structure and numbering are shown in Figure B-1.

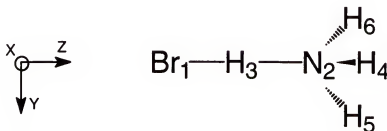


Figure B-1. Schematic geometry and atom numbering for the $\text{BrH}:\text{NH}_3$ complex.

The *.pck file corresponding to this complex is presented in Figure B-2. The first line (heading) always contains five numbers separated by spaces.

#1- Number of internal coordinates defined by the user.

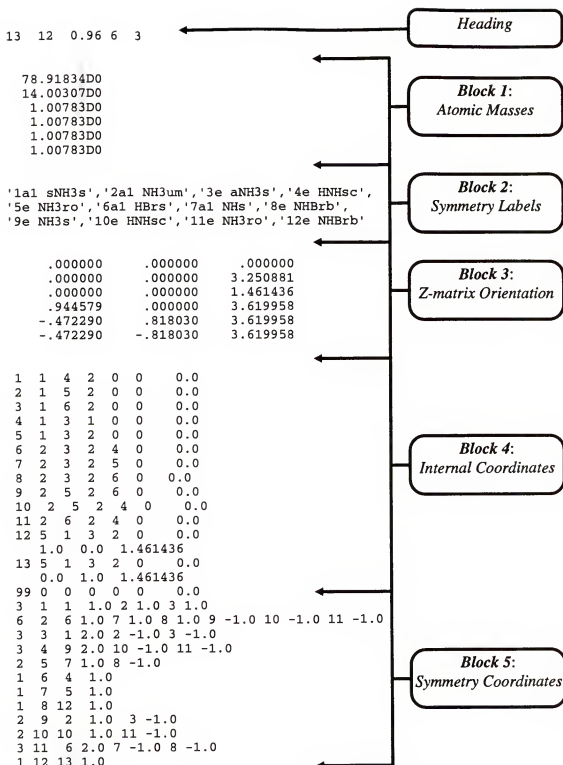
#2- Number of symmetry or normal coordinates.

#3- Scaling factor by which the output frequencies are to be scaled. Note that both scaled and unscaled frequencies are always saved in the output file.

#4- Number of atoms N.

#5- Always "3" (to insure backward compatibility with older *.pck files).

The first block contains the atomic masses in one column (one mass per line as shown in Figure B-2). The order of the masses is very important and must follow the numbering of the standard orientation Table. The second block contains the labels of the symmetry coordinates which must be in single quotation marks and separated by a

Figure B-2. Input *.pck file for the BrH:NH₃ complex.

commas. The third block corresponds to the Z-matrix orientation without the dummy atoms (if any) that are automatically removed by Xtrapack. This orientation is used for all calculations performed by Xtrapack, including the Cartesian atomic displacements. No user input is necessary for this block which is automatically generated by the extraction routine.

Internal Coordinates

The fourth block contains the definitions of the internal coordinates. There should be one coordinate per line. Each line consists of seven numbers defined as follows.

#1- Internal coordinate number. The number "99" indicates the end of the definition of the internal coordinates and the beginning of the definition of the symmetry coordinates.

#2- Type of internal coordinate:

- 1 = stretching,
- 2 = bending,
- 3 = out-of-plane bending,
- 4 = torsion,
- 5 = linear bending.

#3-, #4-, #5-, #6- Atom numbers used in the definition of the coordinate.

#7- Always "0.0" (to insure backward compatibility with older PCK files).

In the example Figure B-2, the first line of block four (1 1 4 2 0 0 0.0) means that the first internal coordinate is a stretching of H(4) against N(2) $\Leftrightarrow \Delta r_{42}$. Line six (6 2 3 2

4 0 0.0) corresponds to a bending of the angle defined by H(3), N(2) and H(4) \Rightarrow $\Delta\alpha_{324}$. The sign “ Δ ” will be omitted in the remainder of this Appendix.

Linear bendings are always defined in pairs because one must consider two orthogonal bending coordinates. Therefore, two perpendicular vectors also need to be defined. In the example Figure B-2, line 12 of block four (12 5 1 3 2 0 0.0) defines a linear bending between atoms Br(1), H(3) and N(2). The following line (1.0 0.0 1.461436) defines the first vector in Cartesian coordinates, perpendicular to the axis defined by these three atoms (here the z-axis) and originating from H(3). Line 13 (13 5 1 3 2 0 0.0) is identical to line 12 and is followed by the second vector (0.0 1.0 1.461436), perpendicular to the first vector and to the z-axis.

Symmetry Coordinates

The symmetry coordinates immediately follow the internal coordinates after the code “99”. There should be one coordinate per line, each a linear combination of internal coordinates defined above. Unlike the internal coordinates, the number of entries per line is variable:

#1- Number of internal coordinates involved in the symmetry coordinate.

#2- Symmetry coordinate number.

#3- Internal coordinate number

#4- Coefficient of the coordinate defined in #3.

#5- and #6- correspond to the next internal coordinate, #7- and #8- to the next, and so on. In the example (Figure B-2), the first line of the symmetry coordinate definition (3 1 1 1.0 2 1.0 3 1.0) indicates that the first symmetry coordinate is the

linear combination of the internal coordinate (1) with a coefficient of 1.0, the internal coordinate (2) with a coefficient of 1.0, and the internal coordinate (3) with a coefficient of 1.0 $\Leftrightarrow 1.0 \times r_{42} + 1.0 \times r_{52} + 1.0 \times r_{62}$.

The following discussion shows how the symmetry coordinate definitions may be found. One can define thirteen internal coordinates for the BrH:NH_3 complex: five stretchings (r_{31} , r_{32} , r_{42} , r_{52} , r_{62}), six bendings (α_{324} , α_{325} , α_{326} , α_{526} , α_{524} , α_{624}), and two linear bends (β_{132x} , β_{132y}). The x, y, z coordinates of the six nuclei span an 18-dimensional reducible representation Γ_{tot} . By inspection of Figure B-1 the characters of Γ_{tot} can be calculated (see Table B-1):

$$\text{Tr}(\Gamma_{\text{tot}}^E) \times n = \text{Tr} \begin{pmatrix} 1 & & \\ & 1 & \\ & & 1 \end{pmatrix} \times 6 = 18, \quad \text{Tr}(\Gamma_{\text{tot}}^{C_3}) \times n = \text{Tr} \begin{pmatrix} \frac{-1}{2} & & \\ & \frac{-1}{2} & \\ & & 1 \end{pmatrix} \times 3 = 0, \text{ etc. (B-1)}$$

where n is the number of atoms unaffected by the given operation.

Table B-1: C_{3v} character table with the total representation Γ_{tot} of HBr:NH_3 .

C_{3v}	E	$2C_3$	$3\sigma_v$	
A_1	1	1	1	z
A_2	1	1	-1	R_z
E	2	-1	0	(x, y)(R_x, R_y)
Γ_{tot}	18	0	4	

To determine which irreducible representations (irreps) are contained in the reducible representation Γ_{tot} , the following equation is applied to each irrep k:

$$a_k = \frac{1}{h} \sum_{q=1}^K \alpha_q \chi_{\text{tot}}(q) \chi_k(q), \quad (\text{B-2})$$

where h is the order of the group, q is any one of the operators of the q^{th} class, κ is the number of classes, α_q is the number of operators in the q^{th} class and χ is the character of the given representation. Γ_{tot} contains

$$a_{A_1} = \frac{1}{6}(1 \times 18 \times 1 + 2 \times 0 \times 1 + 3 \times 4 \times 1) = \frac{30}{6} = 5,$$

$$a_{A_2} = \frac{1}{6}(1 \times 18 \times 1 + 2 \times 0 \times 1 + 3 \times 4 \times -1) = \frac{6}{6} = 1,$$

$$a_E = \frac{1}{6}(1 \times 18 \times 2 + 2 \times 0 \times -1 + 3 \times 4 \times 0) = \frac{36}{6} = 6.$$

The vibrational reducible representation can then be obtained by subtracting the translational and rotational reducible representations obtained from the C_{3v} character table (Table B-1):

$$\begin{array}{rcl} \Gamma_{\text{tot}} = & 5A_1 + & A_2 + & 6E \\ - \Gamma_{\text{tr}} = & A_1 + & & E \\ - \Gamma_{\text{rot}} = & & A_2 + & E \\ \hline \Gamma_{\text{vib}} = & 4A_1 + & & 4E \end{array}$$

Thus, one expects four vibrations with A_1 symmetry and eight vibrations with E symmetry (since E is a two-dimensional representation). The symmetry coordinates are found by applying the trace-projection operator to each internal coordinate according to:¹³⁸⁻¹⁴⁰

$$P_k R = \frac{l_k}{h} \sum_p \chi_k(p) O_p R, \quad (\text{B-3})$$

where P_k is the trace-projection operator for the k^{th} irrep, R is an internal coordinate, l_k is the dimension of the k^{th} irrep and O_p is p^{th} operator of the group. Here, $O_p R$ is the

coordinate into which R is transformed by the symmetry operation O_p . Applied to the BrH:NH_3 complex:

$$P_{A_1} r_{42} = \frac{1}{6} [1 \times r_{42} + 1 \times (r_{62} + r_{52}) + 1 \times (r_{42} + r_{62} + r_{52})] = \frac{2}{6} [r_{42} + r_{52} + r_{62}]$$

Note that since the coordinates r_{52} and r_{62} are also related to the N-H bonds of the ammonia group the above trace-projection operator will produce the same results. The normalization factor will then become $3 \times (2/6) = 1$. The symmetry coordinate obtained above appears in the first line of the fifth block of the *.pck file (symmetry coordinate definitions, Figure B-2). Similarly,

$$P_{A_1} r_{31} = \frac{1}{6} [1 \times r_{31} + 1 \times (r_{31} + r_{31}) + 1 \times (r_{31} + r_{31} + r_{31})] = \frac{6}{6} r_{31} \text{ (line 6),}$$

$$P_{A_1} r_{32} = \frac{6}{6} r_{32} \text{ (line 7).}$$

Note that the last two symmetry coordinates are strictly equal to the internal coordinates.

$$P_{A_1} \alpha_{324} = \frac{1}{6} [(\alpha_{324} + \alpha_{325} + \alpha_{326}) + (\alpha_{324} + \alpha_{325} + \alpha_{326})],$$

$$P_{A_1} \alpha_{524} = \frac{1}{6} [(\alpha_{524} + \alpha_{624} + \alpha_{526}) + (\alpha_{524} + \alpha_{624} + \alpha_{526})].$$

These two symmetry coordinates are not acceptable. Because the BrH:NH_3 complex has a branch (ammonia group), there is a branching redundancy condition¹⁴¹ between the angles α_{324} , α_{325} , α_{326} and α_{524} , α_{526} , α_{624} :

$$\sum_{i < j} \alpha_{i,2,j} = 0 \text{ or here, } \alpha_{324} + \alpha_{325} + \alpha_{326} = -\alpha_{524} - \alpha_{526} - \alpha_{624}, \quad (\text{B-4})$$

so that,

$$P_{A_1} \alpha_{324} = \frac{1}{6} [(\alpha_{324} + \alpha_{325} + \alpha_{326}) - (\alpha_{524} + \alpha_{526} + \alpha_{624})] \text{ (line 2).}$$

Identical results are obtained for all six angles so that the normalization factor equals one.

$$P_{A_1}\beta_x = \frac{1}{6} \left[\beta_x + \left(-\frac{1}{2}\beta_x + \frac{\sqrt{3}}{2}\beta_y - \frac{1}{2}\beta_x - \frac{\sqrt{3}}{2}\beta_y \right) + \left(\beta_x \frac{1}{2}\beta_x - \frac{\sqrt{3}}{2}\beta_y - \frac{1}{2}\beta_x + \frac{\sqrt{3}}{2}\beta_y \right) \right] = 0$$

$$P_{A_1}\beta_y = 0.$$

There is no linear bend with A_1 symmetry. Thus, the four coordinates with A_1 symmetry have been found. The eight coordinates with E symmetry remain to be found.

$$P_E r_{42} = \frac{2}{6} [2 \times r_{42} - 1 \times (r_{62} + r_{52}) + 0 \times (\dots)] = \frac{2}{6} [2r_{42} - r_{62} - r_{52}],$$

$$P_E r_{52} = \frac{2}{6} [2 \times r_{52} - 1 \times (r_{62} + r_{42}) + 0 \times (\dots)] = \frac{2}{6} [2r_{52} - r_{42} - r_{62}],$$

$$\text{Sum} = \frac{2}{6} [r_{42} + r_{52} - 2r_{62}] \text{ (line 3),}$$

$$\text{Diff.} = \frac{6}{6} [r_{42} - r_{52}] \text{ (line 9).}$$

In order to insure orthogonality between symmetry coordinates, the sum and the difference are normally taken.

$$P_E r_{32} = \frac{2}{6} [2 \times r_{32} - 1 \times (r_{32} + r_{32}) + 0 \times (\dots)] = 0,$$

$$P_E r_{31} = 0.$$

$$P_E \alpha_{324} = \frac{2}{6} [2\alpha_{324} - \alpha_{325} - \alpha_{326}] \left\{ \begin{array}{l} \text{Sum} = \frac{2}{6} [\alpha_{324} + \alpha_{325} - 2\alpha_{326}] \text{ (line 11),} \\ \text{Diff.} = \frac{6}{6} [\alpha_{324} - \alpha_{325}] \text{ (line 5).} \end{array} \right.$$

$$P_E \alpha_{325} = \frac{2}{6} [2\alpha_{325} - \alpha_{324} - \alpha_{326}] \left\{ \begin{array}{l} \text{Sum} = \frac{2}{6} [\alpha_{324} + \alpha_{325} - 2\alpha_{326}] \text{ (line 4),} \\ \text{Diff.} = \frac{6}{6} [\alpha_{324} - \alpha_{325}] \text{ (line 10).} \end{array} \right.$$

$$P_E \alpha_{524} = \frac{2}{6} [2\alpha_{524} - \alpha_{625} - \alpha_{624}] \left\{ \begin{array}{l} \text{Sum} = \frac{2}{6} [\alpha_{524} + \alpha_{625} - 2\alpha_{624}] \text{ (line 4),} \\ \text{Diff.} = \frac{6}{6} [\alpha_{524} - \alpha_{625}] \text{ (line 10).} \end{array} \right.$$

$$P_E \alpha_{625} = \frac{2}{6} [2\alpha_{625} - \alpha_{624} - \alpha_{524}] \left\{ \begin{array}{l} \text{Sum} = \frac{2}{6} [\alpha_{524} + \alpha_{625} - 2\alpha_{624}] \text{ (line 4),} \\ \text{Diff.} = \frac{6}{6} [\alpha_{524} - \alpha_{625}] \text{ (line 10).} \end{array} \right.$$

$$P_E \beta_x = \frac{2}{6} \left[2\beta_x - \left(-\frac{1}{2}\beta_x + \frac{\sqrt{3}}{2}\beta_y - \frac{1}{2}\beta_x - \frac{\sqrt{3}}{2}\beta_y \right) \right] = \frac{6}{6}\beta_x \text{ (line 8),}$$

$$P_E \beta_y = \frac{6}{6}\beta_y \text{ (line 12).}$$

Since the linear bends transform into themselves, it is not necessary to take the sum and the difference because these coordinates are already orthogonal to each other. All twelve $(3N - 6)$ coordinates have now been derived.

An important remark must be made at this point. The redundancy condition given in Equation (B-4) is expressed only in the first order. Therefore, the symmetry coordinates obtained using this condition are not exactly orthogonal to each other and the symmetry force constant matrix F_S is not perfectly block diagonal. A higher order condition is necessary to reduce the off-diagonal (and off-block) elements of F_S .

First order redundancy conditions for cyclic molecules¹⁴² like pyridine are more complex but the treatment given above may be employed to find the symmetry coordinates. The definitions for pyridine (C_{2v}) and 4-methylpyridine (C_s) are given (but not derived) in Appendix C.

APPENDIX C SYMMETRY COORDINATE DEFINITIONS

The definitions of the symmetry coordinates in terms of internal displacement coordinates for pyridine and the HBr:pyridine complex are presented in Table C-1. The definitions for 4-chloropyridine (4-CP) and HBr:4-CP are identical to those given in Table C-1, except for the coordinates involving the bond C₄-H which becomes C₄-Cl: $r_{C4H} \rightarrow r_{C4Cl}$; $\beta_{HC4C3} \rightarrow \beta_{ClC4C3}$; $\beta_{HC4C5} \rightarrow \beta_{ClC4C5}$. The same remark can be made for 3,5-dichloropyridine (3,5-DCP) and HBr:3,5-DCP with the bonds C₃-Cl and C₅-Cl. The symmetry definitions for 4-methylpyridine (4-MP) and HBr:4-MP with C_s symmetry are given in Table C-2. Atom labeling for the C_{2v} and C_s groups is shown in Figure C-1.

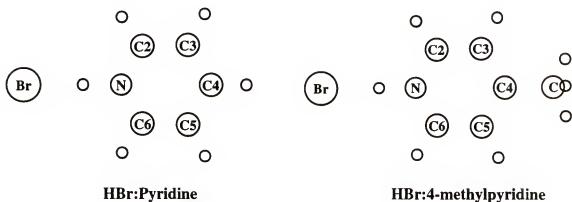


Figure C-1. Ring numbering for the complexes presented in this work with C_{2v} and C_s symmetry. Note that the numbering from the Gaussian output logfile is different than that presented here and depends on the Gaussian input file (user defined).

Table C-1. Symmetry coordinates for pyridine and the HBr:pyridine complex.

Sym. (C_{2v})	Label of coordinate ^a (pyridine)	Label of coordinate ^a (HBr:py)	Definition ^b
a₁	1a ₁ NC	1a ₁ NC	$\Gamma_{C2N} + \Gamma_{C6N}$
	2a ₁ C2C3	2a ₁ C2C3	$\Gamma_{C2C3} + \Gamma_{C5C6}$
	3a ₁ C3C4	3a ₁ C3C4	$\Gamma_{C3C4} + \Gamma_{C4C5}$
	4a ₁ C2H	4a ₁ C2H	$\Gamma_{C2H} + \Gamma_{C6H}$
	5a ₁ C3H	5a ₁ C3H	$\Gamma_{C3H} + \Gamma_{C5H}$
	6a ₁ C4H	6a ₁ C4H	Γ_{C4H}
	7a ₁ C2Hb	7a ₁ C2Hb	$\beta_{HC2N} - \beta_{HC2C3} + \beta_{HC6N} - \beta_{HC6C5}$
	8a ₁ C3Hb	8a ₁ C3Hb	$\beta_{HC3C2} - \beta_{HC3C4} + \beta_{HC5C6} - \beta_{HC5C4}$
	9a ₁ R2	9a ₁ R2	$2\alpha_{C6NC2} - \alpha_{NC2C3} - \alpha_{C2C3C4} + 2\alpha_{C3C4C5} - \alpha_{C4C5C6} - \alpha_{C5C6N}$
	10a ₁ R1	10a ₁ R1	$\alpha_{C6NC2} - \alpha_{NC2C3} + \alpha_{C2C3C4} - \alpha_{C3C4C5} + \alpha_{C4C5C6} - \alpha_{C5C6N}$
		11a ₁ HBr ^c	Γ_{HBr}
		12a ₁ NH ^s	Γ_{NH}
a₂	11a ₂ C2Hw	13a ₂ C2Hw	$\gamma_{C2H} - \gamma_{C6H}$
	12a ₂ C3Hw	14a ₂ C3Hw	$\gamma_{C3H} - \gamma_{C5H}$
	13a ₂ R3o	15a ₂ R3o	$\tau_{6N23} + \tau_{2345} + \tau_{3456} + \tau_{56N2}$
b₁	14b ₁ C2Hw	16b ₁ C2Hw	$\gamma_{C2H} + \gamma_{C6H}$
	15b ₁ C3Hw	17b ₁ C3Hw	$\gamma_{C3H} + \gamma_{C5H}$
	16b ₁ C4Hw	18b ₁ C4Hw	γ_{C4H}
	17b ₁ R1o	19b ₁ R1o	$\tau_{N234} - \tau_{456N}$
	18b ₁ R2o	20b ₁ R2o	$-\tau_{6N23} + \tau_{2345} - \tau_{3456} + \tau_{56N2}$
		21b ₁ NBrw	γ_{NBr}
		22b ₁ NHBrb	β_{NHBr} linear bend out-of-plane
b₂	19b ₂ CN	23b ₂ CN	$\Gamma_{C2N} - \Gamma_{C6N}$
	20b ₂ C2C3	24b ₂ C2C3	$\Gamma_{C2C3} - \Gamma_{C5C6}$
	21b ₂ C3C4	25b ₂ C3C4	$\Gamma_{C3C4} - \Gamma_{C4C5}$
	22b ₂ C2H	26b ₂ C2H	$\Gamma_{C2H} - \Gamma_{C6H}$
	23b ₂ C3H	27b ₂ C3H	$\Gamma_{C3H} - \Gamma_{C5H}$
	24b ₂ C2Hb	28b ₂ C2Hb	$\beta_{HC2N} - \beta_{HC2C3} - \beta_{HC6N} + \beta_{HC6C5}$
	25b ₂ C3Hb	29b ₂ C3Hb	$\beta_{HC3C2} - \beta_{HC3C4} - \beta_{HC5C6} + \beta_{HC5C4}$
	26b ₂ C4Hb	30b ₂ C4Hb	$\beta_{HC4C5} - \beta_{HC4C3}$
	27b ₂ R3	31b ₂ R3	$-\alpha_{NC2C3} + \alpha_{C2C3C4} - \alpha_{C4C5C6} + \alpha_{C5C6N}$
		32b ₂ NHBrb	β_{NHBr} linear bend in-plane
		33b ₂ BrHb	$\beta_{BrNC2} - \beta_{BrNC6}$

Table C-1 -- continued

a) Labels are given as: number of coordinate, symmetry class, brief description. The brief description is meant to be a mnemonic for the coordinates in the detailed definition. Thus, C2C3 is the coordinate concerned with stretching the C2C3 bond and by symmetry the equivalent C5C6 bond, either in phase (a_1) or out of phase (b_2); C2Hb is the in plane bending motion for the C2H and C6H bonds; C2Hw is the out of plane bending motion for the same two bonds. The in plane ring bending motions (R1, etc.) are more complicated as are the out of plane ring puckering motions (R1o, etc.).

b) The definition of the motion in terms of displacement coordinates according to the definition of such coordinates given by Wilson *et al.*,⁶¹ for example. Thus, r_{AB} is the change in the length of the AB bond, α_{ABC} (or β_{ABC}) is the change in the angle between the AB bond and the BC bond (B is the central atom), γ_{C2H} is the out of plane bending mode for a terminal H atom, and τ_{ABCD} coordinates are torsional coordinates involving atoms ABCD (torsion of the AB bond about the BC bond, measured relative to the CD bond). All coordinates are normalized, but the normalization factor is not shown here.

c) The hydrogen bonded proton stretch is given, for $D_{\infty h}$ symmetry, by $r_{HBr} - r_{NH}$; the heavy atom stretch is $r_{HBr} + r_{NH}$. In this less symmetrical C_{2v} complex the mixing of these internal coordinates occurs with coefficients determined by the normal coordinate analysis. Since these coordinates do not exist in pyridine, the numbering of the coordinates following this one are different in the complex.

Table C-2: Symmetry coordinates for 4-MP and the HBr:4-MP complex.

Sym. (C _s)	Label of coordinate (4-MP)	Label of coordinate (HBr:4-MP)	Definition
a'	1a' NC	1a' NC	$\Gamma_{C2N} + \Gamma_{C6N}$
	2a' C2C3	2a' C2C3	$\Gamma_{C2C3} + \Gamma_{C5C6}$
	3a' C3C4	3a' C3C4	$\Gamma_{C3C4} + \Gamma_{C4C5}$
	4a' C2H	4a' C2H	$\Gamma_{C2H} + \Gamma_{C6H}$
	5a' C3H	5a' C3H	$\Gamma_{C3H} + \Gamma_{C5H}$
	6a' C4Me	6a' C4Me	Γ_{C4C}
	7a' C2Hb	7a' C2Hb	$\beta_{HC2N} - \beta_{HC2C3} + \beta_{HC6N} - \beta_{HC6C5}$
	8a' C3Hb	8a' C3Hb	$\beta_{HC3C2} - \beta_{HC3C4} + \beta_{HC5C6} - \beta_{HC5C4}$
	9a' R2	9a' R2	$2\alpha_{C6NC2} - \alpha_{NC2C3} - \alpha_{C2C3C4} + 2\alpha_{C3C4C5} - \alpha_{C4C5C6} - \alpha_{C5C6N}$
	10a' R1	10a' R1	$\alpha_{C6NC2} - \alpha_{NC2C3} + \alpha_{C2C3C4} - \alpha_{C3C4C5} + \alpha_{C4C5C6} - \alpha_{C5C6N}$
	11a' sMe	11a' sMe	$\Gamma_{CH12} + \Gamma_{CH13} + \Gamma_{CH14}$ (methyl symmetric stretch)
	12a' Me um	12a' Me um	$\beta_{H12CC4} + \beta_{H13CC4} + \beta_{H14CC4} - \beta_{H13CH12} - \beta_{H13CH14} - \beta_{H14CH12}$ (methyl umbrella)
	13a' C2Hw	13a' C2Hw	$\gamma_{C2H} + \gamma_{C6H}$
	14a' C3Hw	14a' C3Hw	$\gamma_{C3H} + \gamma_{C5H}$
	15a' C4Mew	15a' C4Mew	γ_{C4C}
	16a' R1o	16a' R1o	$\tau_{N234} - \tau_{456N}$
	17a' R2o	17a' R2o	$-\tau_{6N23} + \tau_{2345} - \tau_{3456} + \tau_{56N2}$
	18a' Me ro	18a' Me ro	$2\beta_{H12CC4} - \beta_{H13CC4} - \beta_{H14CC4}$ (methyl out-of-plane rock)
		19a' HBrs	Γ_{HBr}
		20a' NHs	Γ_{NH}
		21a' NHBrb	β_{NHBrs} (linear bend out-of-plane)
		22a' BrHw	γ_{NBr}
	19a' Me o	23a' Me o	$2\Gamma_{CH12} - \Gamma_{CH13} - \Gamma_{CH14}$ (methyl out-of-plane stretch)
	20a' Me sc	24a' Me sc	$2\beta_{H13CH14} - \beta_{H13CH12} - \beta_{H14CH12}$ (methyl out-of-plane scissors)
a''	21a'' C2Hw	25a'' C2Hw	$\gamma_{C2H} - \gamma_{C6H}$
	22a'' C3Hw	26a'' C3Hw	$\gamma_{C3H} - \gamma_{C5H}$
	23a'' R3o	27a'' R3o	$\tau_{6N23} + \tau_{2345} + \tau_{3456} + \tau_{56N2}$
	24a'' Me tor	28a'' Me tor	$\tau_{H12CC4C3} + \tau_{H13CC4C3} + \tau_{H12CC4C5} + \tau_{H13CC4C5} + \tau_{H14CC4C3} + \tau_{H14CC4C5}$ (methyl torsion)
	25a'' CN	29a'' CN	$\Gamma_{C2N} - \Gamma_{C6N}$
	26a'' C2C3	30a'' C2C3	$\Gamma_{C2C3} - \Gamma_{C5C6}$

Table C-2 -- continued

Sym. (C _s)	Label of coordinate (4-MP)	Label of coordinate (HBr:4-MP)	Definition
	27a" C3C4	31a" C3C4	$r_{C3C4} - r_{C4C5}$
	28a" C2H	32a" C2H	$r_{C2H} - r_{C6H}$
	29a" C3H	33a" C3H	$r_{C3H} - r_{C5H}$
	30a" C2Hb	34a" C2Hb	$\beta_{HC2N} - \beta_{HC2C3} - \beta_{HC6N} + \beta_{HC6C5}$
	31a" C3Hb	35a" C3Hb	$\beta_{HC3C2} - \beta_{HC3C4} - \beta_{HC5C6} + \beta_{HC5C4}$
	32a" C4Meb	36a" C4Meb	$\beta_{CC4C5} - \beta_{CC4C3}$
	33a" R3	37a" R3	$-\alpha_{NC2C3} + \alpha_{C2C3C4} - \alpha_{C4C5C6} + \alpha_{C5C6N}$
	34a" aMe	38a" aMe	$-r_{CH13} + r_{CH14}$ (methyl asymmetric stretch)
	35a" Me ro	39a" Me ro	$\beta_{H14CC4} - \beta_{H13CC4}$ (methyl in-plane rock)
		40a" NHBrb	β_{NHBr} (linear bend in-plane)
		41a" BrHb	$\beta_{BrNC2} - \beta_{BrNC6}$
	36a" aMe sc	42a" aMe sc	$\beta_{H13CH12} - \beta_{H14CH12}$ (methyl asymmetric scissors)

REFERENCES

1. Pauling, L.; Corey, R.B.; Branson, H.R.; *Proc. Nat. Sci. USA* **1951**, 37, 205.
2. Watson, J.D.; Crick F.H.C.; *Nature (Lond.)* **1953**, 171, 737.
3. Almond, M.J.; Downs, A.J.; *Spectroscopy of Matrix Isolated Species*, Vol. 17 of the series "Advance in Spectroscopy", John Wiley & Son, New York, **1989**.
4. Latimer, W.M.; Rodebush, W.H.; *J. Am. Chem. Soc.* **1920**, 42, 1419.
5. Pimentel, G.C.; McClellan, A.L.; *The Hydrogen Bond*. Freeman, San Francisco, **1960**.
6. Pauling, L.; *The Nature of the Chemical bond and the Structure of Molecules and Crystals*; 2nd ed., Cornell Univ. press, Ithaca, New York, **1940**.
7. Atkins, P.; *Physical chemistry*, 5th ed., Freeman, New York, **1994**.
8. Jeffrey, G.A.; Saenger, W.; *Hydrogen Bonding in Biological Structures*, Springer-Verlag, New York, **1991**.
9. Cooley, J.W.; Tukey, J.W.; *Math. Comp.* **1965**, 19, 297.
10. Forman, M.L.; *J. Opt. Soc. Am.* **1966**, 56, 978.
11. Bell R. J.; *Introduction to Fourier Transform Spectroscopy*, Academic Press, New York, **1972**.
12. Griffiths P. R.; *Chemical Infrared Fourier Transform Spectroscopy*, Wiley-interscience, New York, 1975.
13. Ferraro, J. R.; Basile, L. J.; *Fourier Transform Infrared Spectroscopy*, Academic press, New York, Vol. 1 **1978**, Vol. 2 **1979**.
14. Colthup, N. B.; Daly, L. H.; Wiberley, S. E.; *Introduction to Infrared and Raman Spectroscopy*, Academic Press, Boston, **1990**.

15. Van Thiel, M.; Becker, E. D.; Pimentel, G.C.; *J. Chem. Phys.*, **1957**, 27, 486.
16. Van Thiel, M.; Becker, E. D.; Pimentel, G.C.; *J. Chem. Phys.*, **1957**, 27, 95.
17. Whittle, E.; Dows D. A.; Pimentel, G. C.; *J. Chem. Phys.*, **1954**, 22, 1943.
18. Norman, I.; Porter, G.; *Nature*, Lond., **1954**, 174, 508
19. Barnes, A. J.; *Matrix Isolation Spectroscopy*; Reidel, Dordrecht, Boston, London, **1981**.
20. Jacox, M.E.; *J. Mol. Spectrosc.* **1985**, 113, 286.
21. Jacox, M.E.; *J. Mol. Struct.* **1987**, 157, 43.
22. Jacox, M.E.; *Vibrational and Electronic Energy Levels of Polyatomic Transient Molecules*; J. of Phys. and Chem. Ref data, Monograph No. 3; J. Gallagher ed.; Am. Chem. Soc. and Am. Inst. Phys. Pub.; Woodbury, **1994**.
23. Barnes, A. J.; *Rev. Anal. Chem.*, **1972**, 1, 193.
24. Howard, N. H.; Legon, N. W.; *J. Chem. Phys.*, **1988**, 88 , 4694.
25. Barnes, A. J.; Beech, T. R.; Mielke, Z.; *J. Chem. Soc., Faraday Trans. 2*, **1984**, 80, 455.
26. Cradock, S.; Hinchcliffe, A. J. *Matrix Isolation*; Cambridge University Press, Cambridge, **1975**.
27. Orville-Thomas, W. J.; Suzuki, S.; Riley, G.; "Infrared Band Intensities and the Polar Properties of Molecules"; *Vibrational Spectroscopy - Modern Trends*; Barnes Orv-Thomas ed., Elsevier, New York, **1977**.
28. Meyer, B.; *Low Temperature Spectroscopy*, American Elsevier, New York, **1971**.
29. Barnes, A. J.; *J. Mol. Struct.*, **1984**, 113, 161.
30. Barnes, A. J.; *Matrix isolation spectroscopy*, D. Reidel Publishing Company, Dordrecht, Boston, **1981**.
31. Barnes, A. J.; LeGall, L.; Madec, C., Lauransan, J.; *J. Mol. Struct.*, **1977**, 38, 109.
32. Walsh, B.; Barnes, A. J.; Suzuki, S.; Orville-Thomas, W. J. *J. Mol. Spectr.*, **1978**, 60, 343.
33. Barnes, A. J.; *J. Mol. Struct.*, **1980**, 60, 343.

34. Ault, B. S.; Pimentel, G. C.; *J. Phys. Chem.*, **1973**, 77, 1649.
35. Schriver, L.; Schriver, A.; Perchard, J.P.; *J. Am. Chem. Soc.*, **1983**, 105, 3843.
36. Barnes, A. J.; Szczepaniak, K.; Orville-Thomas, W. J.; *J. Mol. Struct.*, **1980**, 59, 39.
37. Barnes, A. J.; Orville-Thomas, W. J.; Szczepaniak, K.; *J. Mol. Struct.*, **1978**, 45, 75.
38. Avakyan, V.G.; Golitsyna, T.L.; Kimel'fel'd, Y. M.; translated from *Zhurnal Strukturnoi Khimii*, **1978**, Vol. 19, 6, 1027.
39. Johnson, G.L.; Andrews, L.; *J. Am. Chem. Soc.*, **1981**, 104, 3043.
40. Barnes, A. J.; Kuzniarski, N. S.; Mielke, Z.; *J. Chem. Soc., Faraday Trans. 2*, **1984**, 80, 465.
41. Bohn, R. B.; Andrews, L.; *J. Phys. Chem.*, **1988**, 93, 3974.
42. Bohn, R. B.; Andrews, L.; *J. Phys. Chem.*, **1989**, 93, 5684.
43. Barnes, A. J.; Wright, M. P.; *J. Chem. Soc., Faraday Trans. 2*, **1986**, 82, 153.
44. Schriver, L.; Schriver, A.; Perchard, J.P.; *J. Chem. Soc., Faraday Trans. 2*, **1985**, 81, 1407.
45. Huggins, C. M.; Pimentel, G. C.; *J. Chem. Phys.*, **1955**, 23, 896.
46. Ratajczak H.; Orville-Thomas, W. J.; *Trans. Faraday Soc.*, **1965**, 61, 2603.
47. Johnson, G. L.; Andrews, L.; *J. Am. Chem. Soc.*, **1982**, 104, 3043
48. Ratajczak H.; Orville-Thomas, W. J.; *J. Mol. Struct.*, **1972**, 14, 155.
49. Ratajczak H.; Orville-Thomas, W. J.; Rao C. N.; *Chem. Phys.*, **1976**, 17, 197.
50. Person, W. B.; in *Matrix Isolation Spectroscopy*, Barnes *et al.* (eds.), D. Reidel Publishing Company, **1981**, p 415-445.
51. Person, W. B.; Steele, D.; *Molecular spectroscopy*, **1974**, 2, 357.

52. Mills, I.; Cvitas, T.; Homann, K.; Kallay, N.; Kuchitsu, k.; *Quantities, Units and Symbols in Physical Chemistry*, 2nd ed., International Union of Pure and Applied Chemistry, Blackwell Science, London, **1993**.
53. Jiang, G. J.; Person, W. B.; Brown, K. G.; *J. Chem. Phys.*, **1975**, 62, 1201.
54. Grams/32, v. 4.0, Galactic Industries Corp., **1996**.
55. M.J. Frisch, G.W. Trucks, H.B. Schlegel, P.M.W. Gill, B.G. Johnson, M.A. Robb, J.R. Cheeseman, T.A. Keith, G.A. Petersson, J.A. Montgomery, K. Raghavachari, M.A. Al-Laham, V.G. Zakrzewski, J.V. Ortiz, J.B. Foresman, J. Cioslowski, B.B. Stefanov, A. Nanayakkara, M. Challacombe, C.Y. Peng, P.Y. Ayala, W. Chen, M.W. Wong, J.L. Andres, E.S. Replogle, R. Gomperts, R.L. Martin, D.J. Fox, J.S. Binkley, D.J. DeFrees, J. Baker, J.P. Stewart, M. Head-Gordon, C. Gonzalez, and J.A. Pople, Gaussian 94; Gaussian, Inc., Pittsburgh, PA (**1995**).
56. Del Bene, J. E.; *Intern J. Quantum Chem. Symp.*, **1992**, 26, 527.
57. Del Bene, J. E.; Mettee, H. D.; *J. Chem. Phys.*, **1993**, 97, 9650.
58. K. KuBulat, Ph.D. Dissertation, University of Florida, 1989.
59. Califano, S.; *Vibrational States*, John Wiley & Sons, New York, **1976**.
60. AniMol 3.2, Infrared & Raman Spectroscopy Teaching and Research Tool for Windows. Innovative Software, 1996.
61. Wilson, E. B.; Decius, J. C.; Cross, P. C.; *Molecular Vibrations: The Theory of Infrared and Raman Vibrational Spectra*; McGraw-Hill, New York, **1955**.
62. Eliashevich, M.; *Compt. Rend. Acad. Sci. U.R.S.S.*, **1940**, 28, 605.
63. Wilson, E. B.; *J. Chem. Phys.*, **1941**, 9, 76.
64. Miyazawa, T.; *J. Chem. Phys.*, **1958**, 29, 246.
65. Wilkinson, H. C.; *The Algebraic Eigenvalue Problem*, Oxford University Press, **1965**.
66. Press, W. H.; Flannery, B. P.; Teukolsky, S. A.; Vetterling, W. T.; *Numerical Recipes: The Art of Scientific Computing*; Cambridge University Press, Cambridge, **1986**.
67. Morino, Y.; Kuchitsu, K.; *J. Chem. Phys.*, **1952**, 20, 1809.
68. Keresztury, B.; Jalsovszky, G.; *J. Mol. Struct.*, **1973**, 10, 304

69. Person, W. B.; Newton, J. H.; *J. Chem. Phys.*, **1974**, 61, 1040.
70. Person, W. B.; Newton, J. H.; *J. Chem. Phys.*, **1976**, 64, 3036.
71. Biarge, J. F.; Herranz, J.; Morcillo, J.; *An. R. Soc. Esp. Fis. Quim.*, **1961**, A57, 81.
72. Person, W. B.; Kubulat, K.; *J. Mol. Struct.*, **1988**, 173, 357.
73. Person, W. B.; Szczepaniak, K.; Del Bene J. E.; *Properties of Substituted pyridines and pyridinium ions. Concepts, Method, and results for pyridine.* To be published.
74. Wong K. N.; Colson, S. D.; *J. Mol. Spec.*, **1984**, 104, 129.
75. Turkevich, J.; Stevenson, P. C.; *J. Chem. Phys.*, **1943**, 11, 328.
76. Kline, J.; Turkevich, J.; *J. Chem. Phys.*, **1944**, 12, 300.
77. Corrsin, L.; Fax, B. J.; Lord, D. R.; *J. Chem. Phys.*, **1953**, 21, 1170.
78. McCullough, J. P.; Doulsin, D. R.; Messerly, J. F.; Hossenlopp, I. A.; Kincheloe, T. C.; Waddington, G.; *J. Am. Chem. Soc.*, **1957**, 79, 4289.
79. Wilmschurst, J. K.; Bernstein, H. J.; *Canad. J. Chem.*, **1957**, 35, 1183.
80. Kovner, M. A.; Korostelev, Y. S.; Berezin, V. I.; *Opt. Spectrosc.*, **1961**, 10, 233.
81. Berezin, V. I.; *Opt. Spectrosc.*, **1963**, 15, 167.
82. Long, D. A.; Murfin, F. S.; Thomas, E. L.; *Trans. Faraday Soc.*, **1963**, 59, 12.
83. Zerbi, G.; Crawford, B.; Overend, J.; *J. Chem. Phys.*, **1963**, 38, 127.
84. Loisel, J.; Lorenzelli, V.; *J. Mol. Struct.*, **1967**, 37, 321.
85. Castellucci, E.; Sbrana, G.; Verderam, F. D.; *J. Chem. Phys.*, **1969**, 51, 3762.
86. Suzuki, S.; Orville-Thomas, W. J.; *J. Mol. Struct.*, **1977**, 37, 321.
87. Kakiuti, Y.; Akiyama, M.; Saito, N.; Saito, H.; *J. Mol. Spec.*, **1976**, 61, 164.
88. Mochizuki, Y.; Kaya, K.; Ito, M.; *J. Chem. Phys.*, **1978**, 69, 935.
89. Harsanyi, L.; Kilar, F.; *J. Mol. Struct.*, **1980**, 65, 141.

90. Stidham, H. D.; Dilella, D. P.; *J. Raman Spectrosc.*, **1979**, 8, 247.
91. Dilella, D. P.; Stidham, H. D.; *J. Raman Spectrosc.*, **1980**, 9, 90.
92. Dilella, D. P.; *J. Raman Spectrosc.*, **1980**, 9, 239.
93. Stidham, H. D.; Dilella, D. P.; *J. Raman Spectrosc.*, **1980**, 9, 247.
94. Jones, W. J.; "The Infra-red Spectra of Simple Molecules." *Infra-Red Spectroscopy and molecular structure*; Ed. Mansel Davies, Elsevier, Amsterdam, **1963**.
95. Welti, D.; *Infrared Vapor Spectra*; Heyden & Son Ltd, London, **1970**.
96. Fletcher, W.H.; "Band Contour Analysis"; *Vibrational Spectroscopy - Modern Trends*; Barnes Orv-Thomas ed., Elsevier, New York, **1977**.
97. Wong K. N.; Colson, S. D.; *J. Phys. Chem.*, **1983**, 87, 2102.
98. Barnes, A. J.; Hallam, H.E.; Scrimshaw, G. F.; *Trans. Faraday Soc.*, **1969**, 65, 3172.
99. Shriver A.; Silvi, B.; Maillard, D.; Perchard, J. P.; *J. Phys. Chem.*, **1977**, 81, 2095.
100. Glazunov, V. P.; Odínokov, S. E.; *Spectrochim Acta, Part A*, **1982**, 38, 399.
101. Glazunov, V. P.; Odínokov, S. E.; *Spectrochim Acta, Part A*, **1982**, 38, 409.
102. Foglizzo, R.; Novak, A.; *J. Chem. Phys.*, **1969**, 66, 1539.
103. Del Bene, J. E.; Person, W. B.; Szczepaniak, K.; *Molecular Physics*, **1996**, 89, 47.
104. Del Bene, J. E.; Person, W. B.; Szczepaniak, K.; *Chem. Phys. Lett.*, **1995**, 247, 89.
105. Del Bene, J. E.; Szczepaniak, K.; Chabrier, P.; Person, W. B.; *Chem. Phys. Lett.*, **1997**, 264, 109.
106. Somorjai, R. L.; Hornig, D. F.; *J. Chem. Phys.*, **1962**, 36, 1980.
107. Tanaka, K.; Kasasaku, K.; Shimada, H.; Shimada, R.; *Bull. Chem. Soc. Jpn.*, **1988**, 61, 1917.
108. Green, J. H.; Harrison, D. J.; Kipps, M. R.; *Spectrochim Acta*, **1973**, Vol. 29A, 1177.
109. Tripathi, R. S.; *Indian J. of pure & Applied Phys.*, **1973**, 11, 277.

110. Szczepaniak, K.; Chabrier, P.; Person, W. B.; Del Bene, J. E.; *J. Mol. Struct.*, **1997**, 436 - 437, 367.
111. Del Bene, J. E.; Jordan, M. J.; Gill, P. M.; Buckingham, A. D.; *Molecular Physics*, **1997**, 92, 429.
112. Pulay, P.; Fogarasi, G.; Pongor, G.; Boggs, J. E.; Vargha, A.; *J. Am. Chem. Soc.*, **1983**, 105, 7037.
113. Szczepaniak, K.; Chabrier, P.; Person, W. B.; "*NH₃:HCl complex: unsolved mysteries*", to be published.
114. Cook, G. L.; Church, F. M.; *J. Phys. Chem.*, **1957**, 61, 458.
115. Green, J. H.; Harrison, D. J.; Paisley, H. M.; *Spectrochim Acta*, **1963**, 19, 549.
116. Katritzky, A. R.; Gardner, J. N.; *J. Chem. Soc.*, **1958**, 2198.
117. Draeger, J. A.; *Spectrochim Acta, Part A*, **1983**, 39, 809.
118. Yoshikai, K.; Hieida, T.; Nibu, Y.; Shimada, H.; Shimada, R.; *Bull. Chem. Soc. Jpn.*, **1990**, 63, 1529.
119. Inoue, K.; Kuze, N.; Tanabe, M.; Takeuchi, H.; Egawa, T.; *J. Mol. Struct.*, **1997**, 413-414, 81.
120. Green, J. H.; Kynaston, W.; Paisley, H.M.; *Spectrochim Acta, Part A*, **1963**, 19, 549.
121. Berezin, V. I.; El'kin, M. D.; Translated from *Khimiya Geterotsiklicheskikh Soedinenii*, **1978**, 4, 501.
122. Lamba O. P.; Parihar, J. S.; Bist, H. D.; Jain, Y. S.; *Indian J. of pure & Applied Phys.*, **1983**, 21, 231.
123. Akyuz, J. E.; Davies, J. E.; Holmes, K. T.; *J. Mol. Struct.*, **1977**, 42, 59.
124. Andras, M. T.; Hepp, A. F.; Fanwick, P. E.; Martuch, R. A.; Duraj, S. A.; *Acta Cryst., C (Cr. Str. Comm.)*, **1993**, 49, 548.
125. Dreager, J. A.; *Spectrochim Acta, Part A*, **1983**, 39, 809.
126. Green, J. H.; Harrison, D. J.; Kynaston, K.; Paisley, H. M.; *Spectrochim Acta, Part A*, **1970**, 26, 2139.

127. Szczepaniak, K.; Chabrier, P. H.; Person, W. B.; *The HBr:NH₃ complex*, to be published.
128. Szczepaniak, K.; Chabrier, P. H.; Person, W. B.; *The HCl Series of Complexes with Substituted Pyridines*, to be published.
129. Ault, B. S.; Steinback, E.; Pimentel, G. C.; *J. Phys. Chem.*, **1975**, 79, 615.
130. Lias, S.G.; Liebman, J. F.; Levin, R. D.; *J. Phys. Chem. Ref. Data*, **1984**, 13, 695.
131. Lias, S.G.; Bartmess, J. E.; Liebman, J. F.; Holmes, J. L.; *J. Phys. Chem. Ref. Data*, **1988**, 17, 1.
132. Howard, N. W.; Legon, A. C.; *J. Chem. Phys.*, **1987**, 86, 6722.
133. Howard, N. W.; Legon, A. C.; *J. Chem. Phys.*, **1988**, 88, 4694.
134. Legon, A. C.; Rego, C. A.; *J. Chem. Phys.*, **1989**, 90, 6867.
135. Legon, A. C.; Wallwork, A. L.; *J. Chem. Phys.*, **1990**, 92, 6397.
136. Legon, A. C.; *Chem. Soc. Rev.*, **1993**, 22, 143.
137. Chabrier, P. H.; *Approximate Energy Cross Sections for the HCl Series of Complexes with four Substituted Amines*, unpublished.
138. Douglas, B. E.; Hollingsworth, C. A.; *Symmetry in Bonding and Spectra*, Academic Press, Inc., London, **1985**.
139. Sverdlov, L. M.; Kovner, M. A.; Krainov, E. P.; *Vibrational Spectra of Polyatomic Molecules*, Halsted Press, New York, **1974**.
140. Lowe, J. P.; *Quantum Chemistry*, 2nd edition, Academic Press, Inc, San Diego, 1993.
141. Shimanouchi, T.; *J. Chem. Phys.*, **1949**, 17, 245.
142. Califano S.; Crawford, B.; *Z. Electrochem.*, **1960**, 64, 571.

BIOGRAPHICAL SKETCH

Pierre Henri Chabrier was born on March 12, 1967, in Gennevilliers, France. He attended the University of Orsay (France) for five years where he received successively an associate degree in laser and fiber optics, a B.S. and M.S. in applied physics and finally, a “diplôme d'études approfondies” (no US equivalent) in physical chemistry in 1991. Following an (involuntary) break to complete his service in the armed forces, he found his way to the University of Florida in 1993 to pursue a Ph.D. in physical chemistry. There, he learned a lot about the American culture and met his wife Christina. Aside from science, Pierre enjoys many things in life. For instance, he can watch flowers like many watch fireworks. His passions do not stop at the surface of the earth, as he was conferred a license of private pilot by the French DGAC in 1992 and by the American FAA in 1998. Against winds and tides, he strives to stand for his belief that it is better to know nothing about everything than everything about nothing, an homage to the philosopher and scientist François Rabelais who wrote “science sans conscience n'est que ruine de l'âme.”

I certify that I have read this study and that in my opinion it conforms to acceptable standards of scholarly presentation and is fully adequate, in scope and quality, as a dissertation for the degree of Doctor of Philosophy.



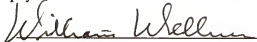
Willis B. Person, Chairman
Professor of Chemistry

I certify that I have read this study and that in my opinion it conforms to acceptable standards of scholarly presentation and is fully adequate, in scope and quality, as a dissertation for the degree of Doctor of Philosophy.



Martin T. Vala
Professor of Chemistry

I certify that I have read this study and that in my opinion it conforms to acceptable standards of scholarly presentation and is fully adequate, in scope and quality, as a dissertation for the degree of Doctor of Philosophy.



William Weltner
Professor of Chemistry

I certify that I have read this study and that in my opinion it conforms to acceptable standards of scholarly presentation and is fully adequate, in scope and quality, as a dissertation for the degree of Doctor of Philosophy.



Lisa A. McElwee-White
Professor of Chemistry

I certify that I have read this study and that in my opinion it conforms to acceptable standards of scholarly presentation and is fully adequate, in scope and quality, as a dissertation for the degree of Doctor of Philosophy.



Neil S. Sullivan
Professor of Physics

This dissertation was submitted to the Graduate Faculty of the Department of Chemistry in the College of Liberal Arts and Sciences and to the Graduate School and was accepted as partial fulfillment of the requirements for the degree of Doctor of Philosophy.

August 1998

Dean, Graduate School